UNIVERSITÄTSKLINIKUM HAMBURG-EPPENDORF

Institut für Osteologie und Biomechanik

Prof. Dr. med. Michael Amling

# *Yersinia enterocolitica* infection: the role of the lysosome-autophagy pathway in intestinal epithelial cells and organoids

**Dissertation**

zur Erlangung des Doktorgrades PhD
an der Medizinischen Fakultät der Universität Hamburg

vorgelegt von:

Gianmarco Del Gallo
aus Spoleto (Pg), Italy

Hamburg 2025

***To my family***

**(wird von der Medizinischen Fakultät ausgefüllt)**

**Angenommen von der**
**Medizinischen Fakultät der Universität Hamburg am:** 31.03.2025

**Veröffentlicht mit Genehmigung der**
**Medizinischen Fakultät der Universität Hamburg.**

**Prüfungsausschuss, der/die Vorsitzende:** Prof. Dr. Thomas Braulke

**Prüfungsausschuss, zweite/r Gutachter/in:** Prof. Dr. Tim Wolf Gilberger

# Table of Contents

# 1. Introduction

Lysosomes are dynamic membrane-bound and acidic organelles of eukaryotic cells that function in the degradation, processing and recycling of a variety of cargos and biological macromolecules (such as proteins, lipids, polysaccharides and nucleic acids) delivered to lysosomes via endocytic, phagocytic and autophagic pathways. Lysosomes participate also in other cellular processes including wound healing, nutrient- and energy sensing, antigen processing, and the final clearance of intracellular phagocytosed pathogens by fusing with phagosomes or autophagosomes. Therefore, they play a primary role in the defence, maintenance and restoration of cellular homeostasis. In addition, dysfunctions of lysosomal activities cause rare inherited neurodegenerative and skeletal diseases, and they are involved in more common metabolic disorders and cancer (Eriksson and Öllinger, 2024).

## 1.1 Lysosomes

About 50 to 1000 lysosomes are detectable in the cytosol of single animal cells constituting up to 5% of the intracellular volume. These organelles are delimited by a single-layer lipid membrane and vary in diameters between 50 nm and 500 nm in relation to cellular needs, environmental cues or physical interactions with other subcompartments (Ballabio and Bonifacino, 2020). Lysosomes are characterized by an acidic internal pH (4.6-5.0) that is maintained by a proton-pumping vacuolar ATPase, (v-ATPase; Luzio et al., 2007). They contain ~70 soluble acid hydrolases (such as proteases, lipases, glycosidases, sulfatases, phosphatases, and nucleases) and accessory proteins, in addition to more than 250 integral membrane proteins. Moreover, 150 associated proteins are known to be localized on the cytosolic surface of lysosomes involved in organelle fusion, contact sites with other subcellular compartments, mobility and positioning of lysosomes, and metabolic signaling (Ballabio and Bonifacino, 2020). Biosynthesis of lysosomes comprises the **i)** coordinated transcription of genes encoding lysosomal proteins, **ii)** the synthesis of lysosomal proteins **iii)** post-translational modifications (e.g. glycosylation, acylation, proteolytic processing), and **iv)** the sorting and targeting of newly synthesized lysosomal proteins. Several lysosomal genes comprise a palindromic 10-bp GTCACGTGAC motif in their promoter region that can bind to members of the MiTF transcription factor family (e.g. the transcription factor EB (TFEB), the transcription factor EC (TFEC), the transcription factor E3 (TFE3), and the Microphthalmia-associated transcription factor MITF) resulting in their transcriptional activation (Ballabio and Bonifacino, 2020).

Details about the protein synthesis, post-translational modifications and targeting of lysosomal enzymes are described in the next chapters.

## 1.2 Synthesis and transport of soluble lysosomal enzymes

### 1.2.1 Biosynthesis of soluble lysosomal proteins

Soluble lysosomal enzymes as well as accessory proteins are synthesized as preproproteins in the endoplasmic reticulum (ER) and translocated into the ER lumen due to a mostly hydrophobic *N*-terminal signal peptide of 20-25 amino acids (aa) (Walter et al., 1984). Preproproteins contain a signal peptide, directing them into the ER lumen, where it is cleaved by a signal peptidase. Select Asn residues located in a consensus sequence Asn-X-Ser/Thr (X can be any amino acid except Pro and Asp) can be co-translationally *N*-glycosylated by the oligosaccharyltransferase (Ruddock and Molinari, 2006) by a transfer of pre-assembled oligosaccharides $Glc_3Man_9GlcNAc_2$. These *N*-linked oligosaccharides are trimmed sequentially by various glycosidases generating the $Glc_1$-$Man_9$-$GlcNAc_2$ intermediate, required for binding of chaperones, and proper folding which is prerequisite for the transport to the Golgi apparatus (Helenius and Aebi, 2001). The newly synthesized and glycosylated lysosomal enzymes are transported to the *cis*-Golgi in 60-70 nm membrane-bound coat protein complex II (COPII) vesicles transiting through the ER-Golgi intermediate compartment (ERGIC) (Fromme and Schekman, 2005; Zanetti et al., 2012). Here, lysosomal enzymes are modified with mannose 6-phosphate (M6P) residues on high-mannose type carbohydrates, a prerequisite for their sorting to lysosomes (Braulke et al., 2024). Upon arrival in lysosomes the propeptide is cleaved by various peptidases at the acidic pH and results in a catalytically active and mature functional enzyme (Braulke and Bonifacino, 2009).

### 1.2.2 Generation of M6P targeting signals

Mannose 6-phosphate moieties on lysosomal proteins are generated by a sequential action of two enzymes: in the first step, the UDP-*N*-acetylglucosamine (UDP-GlcNAc):lysosomal enzyme *N*-acetylglucosamine 1-phosphotransferase (GlcNAc-1-phosphotransferase; GNPT) transfers an *N*-acetyl-glucosamine 1-phosphate (GlcNAc-1-P) from the UDP-GlcNAc to the hydroxyl group at position C6 of specific terminal mannose residues of high-mannose type oligosaccharides in the α1,6- rather than in α1,3-branch. Phosphorylation can occur at one or two of the five outer mannose residues and the total number of phosphorylated *N*-linked oligosaccharides varies depending on the lysosomal enzyme (Kornfeld and Sly, 2001). In a second step, the phosphodiester intermediate is hydrolyzed by a GlcNAc-1-phosphodiester α *N*-acetylglucosaminidase (or ‘uncovering enzyme’, UCE), localized in the *trans*-Golgi network (TGN) exposing the M6P residues for the recognition by M6P receptors (MPR) (Braulke and Bonifacino, 2009) which is described in detail in the next chapters.

### 1.2.3 Structural properties and functions of the GlcNAc-1-phosphotransferase complex

The GlcNAc-1-phosphotransferase complex was isolated and purified from lactating bovine mammary glands and leading to a model of 540 kDa heterohexameric complex, composed of a disulfide-linked α-subunit homodimer, a non-covalently linked β-subunit dimer, and two disulfide-linked γ-subunits (Bao et al., 1996). An enzymatically inactive α/β- subunit precursor is encoded by the *GNPTAB* gene (Kudo et al., 2005; Tiede et al., 2005), whereas the *GNPTG* gene encodes for the γ-subunit (Raas-Rothschild et al., 2000). The α/β- subunit precursor is an *N*-glycosylated type III membrane protein composed of 1256 aa, with both the N-terminal (19 aa) and C-terminal tail (21 aa) facing the cytosol. It is highly conserved in human, mouse, rat, chicken and zebrafish. Furthermore, the GNPT-precursor contains 20 potential *N*-glycosylation sites, 17 on the α-subunit and 3 on the β-subunit (Tiede et al., 2005; Kollmann et al., 2010). A combinatorial sorting motif has been identified consisting of a dominant dileucine (LL) and a dibasic RIR motif in the N- and C-terminal cytosolic domains, respectively, required to exit the ER and to be transported to the Golgi apparatus in COPII-coated vesicles (Franke et al., 2013). The soluble γ-subunit contains 305 aa, equipped with a predicted signal sequence of 24 aa and 2 *N*-glycosylation sites (Raas-Rothschild et al., 2000). The γ-subunits are proposed to increase the activity of the GNPT toward select lysosomal enzymes and facilitate the addition of a second GlcNAc-1-P group to high mannose oligosaccharides on newly synthesized lysosomal enzymes (Qian et al., 2010). The luminal domain of the α/β-subunit precursor consists of a modular structure containing four conserved regions (CR1-CR4) assembling into a stealth domain which constitutes the catalytic center and harbor the UDP-GlcNAc binding site (Li et al., 2024; Braulke et al., 2024). Additionally, two Notch repeats (N1 and N2) and a DMAP (DNA-methyltransferase-associated protein) domain mediating the interactions with protein determinants on lysosomal enzymes (Braulke et al., 2024). Among the four spacer regions (S1-S4), the S2 region has been identified as the interaction site between α- and γ-subunits (De Pace et al.,2015; Gorelik et al., 2022). Between the CR3 and CR4 domain (aa 955 – 1194) in the β-subunit, a small EF-hand motif is located which contains a $Ca^{2+}$-

binding domain and coordinates $Ca^{2+}$ ions (Fig. 1.1 A) (Gorelik et al., 2022; Braulke et al., 2024). Recently a novel factor, transmembrane protein 251 (TMEM251), has been identified that is responsible for the proper localization, stability and retention of the GNPT complex in the *cis*- Golgi (Fig. 1.1 B). The deletion of TMEM251 results in a rapid degradation of GNPT in lysosomes and to a secondary failure to modify lysosomal enzymes with M6P tags unable to be transported to lysosomes. Therefore, TMEM251 was renamed LYSET (Lysosomal Enzyme Trafficking factor). It is a small non-glycosylated protein passing twice the membrane and interacts with GNPT in the *cis*-Golgi (Richards et al., 2022). The α- and β-subunits of the GNPT present hydrophilic transmembrane helices and their membrane integration is facilitated by the hydrophobic transmembrane helices of LYSET, providing free energy to favor the integration process into the membrane (Pechincha et al., 2022). The molecular mechanism of how the GNPT-LYSET complex is retained in the *cis*-Golgi still needs to be elucidated.

A

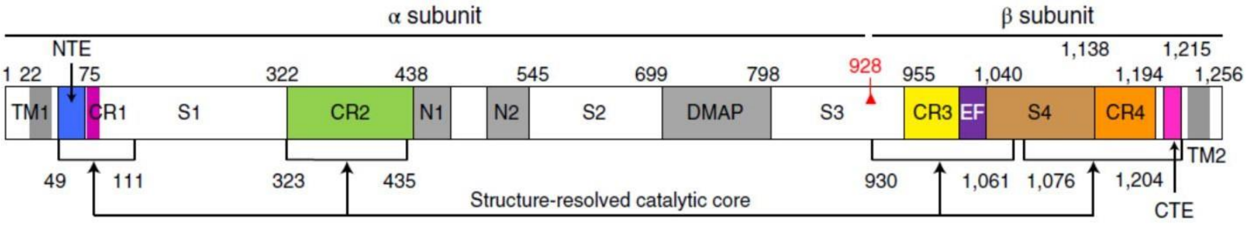

B

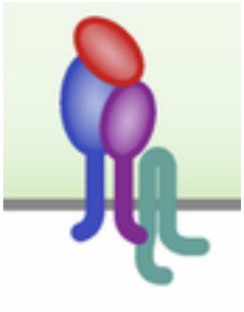

**Figure 1.1**. (**A**) **Structural domains of human GNPT** (Li et al., 2022). (**B**) **Schematic representation of the structure of the GNPT enzyme**. Here, one alpha- (blue), one beta- (purple) and one gamma-subunit (red) are shown. Recently LYSET (green), a Golgi retention factor for GNPT, has been identified (Brauer et al., 2024).

### 1.2.4 Proteolytic activation and Golgi retention of the GlcNAc-1-phosphotransferase complex

The proteolytic cleavage of the α- and β-subunits precursor protein of the GlcNAc-1-phosphotransferase complex is a prerequisite for the enzymatic activity of the phosphotransferase (Kudo and Canfield, 2006). The cleavage between $Lys^{928}$ and $Asp^{929}$ is catalyzed by the membrane-bound site-1 protease (S1P), a *cis*-Golgi-resident enzyme resulting in the formation of mature 190 kDa glycosylated α- and 45 kDa β-subunits (Fig. 1.1 A) (Marschner et al., 2011). S1P is a type I membrane protein composed of 1052 aa, belonging to the mammalian proprotein convertase subtilisin/kexins (PCSK) family which proteolytically activate several precursor proteins in the secretory pathway such as the sterol regulatory element-binding proteins SREBP1 and 2, the activating transcription factor ATF6, and envelope glycoproteins of various viruses (Ye et al., 2000; Seidah and Prat, 2012). S1P deficiency results in the loss of the GNPT activity, missorting of lysosomal enzymes and accumulation of unesterified cholesterol in lysosomes (Marschner et al., 2011). The S1P knock-out (KO) in mice is embryonically lethal (Yang et al., 2001). Since the first report in 2018, more than 10 patients aged 5 to 24 years were diagnosed with a new autosomal recessive skeletal disorder, spondyloepiphyseal skeletal dysplasia exhibiting mutations in a gene, which encodes S1P (Kondo et al., 2018).

### 1.2.5 Mannose 6-phosphate receptor-dependent transport of lysosomal enzymes

The segregation of newly synthesized M6P-containing lysosomal proteins from the secretory pathway to endosomes is mediated by receptors. In the TGN, M6P moieties can be recognized by two homodimeric M6P-specific receptors (MPRs) characterized by distinct molecular masses, the 46 kDa cation-dependent MPR (CD-MPR or MPR46) and the 300 kDa cation-independent MPR (CI-MPR or MPR300). Both receptors are type I transmembrane glycoproteins sharing sequence similarities in the luminal domain, however the MPR300 contains two high-affinity M6P binding sites while MPR46 have one binding site. They differ in their expression levels, tissue distribution, transport functions and ligand binding properties (Ghosh et al., 2003; Braulke and Bonifacino, 2009). The MPR-ligand complexes are formed in the TGN at a relatively neutral pH of 6.5, budding in clathrin-coated vesicles (CCV) and fuse with the endosomal compartment. Due to the low pH (≤6) the MPR-lysosomal enzyme complexes dissociate in the endosomes (Casey, Grinstein and Orlowski, 2010) followed by MPR recycling to the TGN. Small amounts of both MPRs (3-10%) are localized at the plasma membrane and exchange continuously with MPR in intracellular compartments. However, only MPR300s are able to endocytose M6P-ligands from the extracellular space. In non-tumour cell lines 5-20% of newly synthesized lysosomal enzymes escape binding to MPRs in the TGN and are secreted. They can be partially recaptured by MPR300 localized at the plasma membrane and delivered along the endocytic pathway to lysosomes (Braulke and Bonifacino, 2009). Upon arrival of the M6P-containing precursor enzymes in lysosomes, they are dephosphorylated by the concerted role of the acid phosphatases Acp2 and Acp5 (Makrypidi et al., 2012) and many of them are proteolytically activated (Yadati et al., 2020).

## 1.3 Autophagy

Autophagy is a fundamental process that provides amino acids during starvation, removes and delivers intracellular debris to lysosomes for degradation and recycling of the building blocks. It acts also as a housekeeping system which removes misfolded or aggregated proteins, and damaged organelles serving as organelle quality control and as essential part of the cellular stress response (Zhao et al., 2021). Macroautophagy (here called autophagy) is the major pathway through which cytoplasm, large cytoplasmic cargos (such as damaged organelles or microbes) and specific targets sequestered in double membrane-bound autophagosomes fuse with multiple lysosomes to form autolysosomes (Fig. 1.2; Nanayakkara et al., 2023; Zhen and Stenmark, 2023).

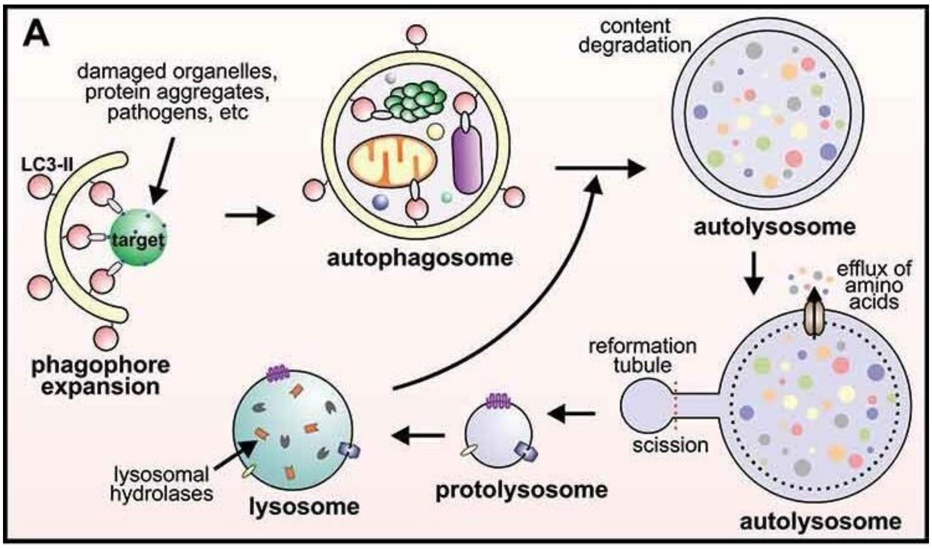

**Figure 1.2. Autophagy overview and autolysosomes biogenesis**. During autophagic lysosome reformation (ALR) the autolysosome membrane generates "reformation tubules", whose scission produces membrane fragments, the proto-lysosomes, which mature into functional lysosomes (Nanayakkara et al., 2023).

Mechanistically, autophagy consists of different phases: initiation, elongation, maturation, fusion and degradation. All the steps are mainly regulated by about 20 Atg proteins acting in concert with other players, up to 200 human proteins involved in autophagy (Nagatokawa, 2020; Oughtred et al., 2021). The initiation core machinery is the ULK complex comprising ULK, Atg13, FIP200 and Atg101 which is responsible for the autophagophore formation, whose membrane sources involve plasma membrane, ER, Golgi apparatus, COPI-coated vesicles, late endosomes, mitochondria and lipid droplets (Zhao et al., 2021; Zhen and Stenmark, 2023). The ULK complex activates the Beclin1-Vps34-Atg14L-p150 complex by Beclin1 phosphorylation, triggering the generation of phosphatidylinositol-3-phosphate ($PI_3P$), which is essential for recruiting autophagic Atg9 vesicles and $PI_3P$-effectors like WIPI2/WIPI4 (nucleation). Membrane elongation involves the microtubule-associated protein 1 light chain 3 (LC3) which is modified by a phosphatidylethanolamine (PE) and forms LC3II, stably inserted into the phagophore membrane that is promoted by Atg12/Atg5/Atg16L. Cargo selection partly occurs by targeted ubiquitination, recognized by receptor proteins such as p62/SQSTM1, TAX1BP1 or NBR1 and it directs the cargo to phagophores followed by ESCRT-II/Vps4-mediated closure of autophagosomes. In the final fusion step of autophagosomes with lysosomes, several proteins are involved, among them UVRAG (autophagosomes maturation and Rab7 recruitment), Rab7 (endosomes maturation and fusion with lysosomes), SNAREs such as Syntaxins (STX) 7 and STX17 (membranes fusion events), LAMPs (lysosomal membrane markers), allowing the degradation of the content in acidic autolysosomes (Zhao et al., 2021). To maintain autophagy a sufficient number of lysosomes is required, which is achieved either by the de novo biogenesis pathway and controlled by the nutrient-sensing mTORC1 kinase or transcriptionally by member of the MiTF transcription factor family (see 1.1). Alternatively, lysosomes are re-generated from autolysosomes, called autophagic lysosome reformation (ALR), that includes budding and extruding of protolysosomal tubules, their scission and maturation into functional lysosomes (de Araujo et al., 2020; Nanayakkara et al., 2023). Defective formation and maturation of degradative autolysosomes or in the ALR process are associated with the pathogenesis of various human diseases, including neurodegenerative and lysosomal storage disorders, cancer and inflammatory and liver diseases (Zhao et al., 2021; Nanayakkara et al., 2023).

## 1.4 Inherited loss of GlcNAc-1-phosphotransferase activity

The total loss of *GNPT* activity leads to a severe inherited autosomal recessive disease, mucolipidosis type II (ML II; Tiede et al., 2005; Braulke et al., 2024). Biochemically the disease is characterized by the loss of intracellular lysosomal enzymes caused by the absence of M6P residues, high amounts of lysosomal enzymes in the serum, and swollen lysosomes filled with heterogeneous originally eponymous as inclusion disease (Leroy and Demars, 1967). Clinically ML II patients present early onset symptoms such as thoracic deformities and dwarfism, neurodegeneration, skeletal abnormalities, facial dysmorphism, organomegalies including cardiomegaly leading to death between 5 and 8 years of age. To date, neither causal treatment exists for ML II nor clinical trials have been initiated.

## 1.5 The *Gnpt*$^{c.3082insC}$ mouse model

The disease model which most closely resembles the human ML II disease phenotype is a *Gnptab* knock-in (ki) mouse generated in the Braulke group by insertion of a single cytosine (c.3082insC) identified in an ML II patient (c.3145insC) that leads to a C-terminal truncation with an almost total loss of the beta-subunit (Kollmann et al., 2012). The growth, brain development, the humoral immunity (in particular B-cells; Otomo et al., 2015) are severely impaired, and numerous skeletal, craniofacial and dental alterations are observed in *Gnpt*$^{c.3082insC}$ mice. The loss of M6P modifications on lysosomal enzymes and the subsequent accumulation of specific non-degraded storage material (fucosylated complex oligosaccharides, non-esterified cholesterol, gangliosides, bis(monoacylglycero)phosphates (BMP) and other lipids) have been reported (Kollmann et al., 2012; Markmann et al., 2015; Koehne et al., 2016; Schweizer et al., 2013).

## 1.6 Lysosome positioning

Lysosomes are broadly distributed within the cell and move along actin filaments and microtubule tracks connected through effector proteins, in response to physiological or external stimuli (Pu et al., 2016; Eriksson and Öllinger, 2024). Short transport ways on actin filaments are slow (~0.1 µm/sec), while long routes of lysosomes on microtubule tracks are faster (~1 µm/sec) (Eriksson and Öllinger, 2024). Lysosomes form a relatively immobile perinuclear pool, that is characterized by a low luminal pH, and/or create a dynamic peripheral pool with a more alkaline pH in the cell periphery (Johnson et al., 2016; Cabukusta and Neefjes, 2018). Peripheral lysosomes are involved in membrane repair, exocytosis and in the control of mTORC1 activation, whereas starvation induces the perinuclear positioning of lysosomes which can fuse with autophagosomes to degrade autophagic cargos and recycle nutrients (Encarnação et al., 2016; Korolchuk et al., 2011). The bidirectional movement of lysosomes requires kinesin or dynein motor proteins (Fig. 1.3; Eriksson and Öllinger, 2024).

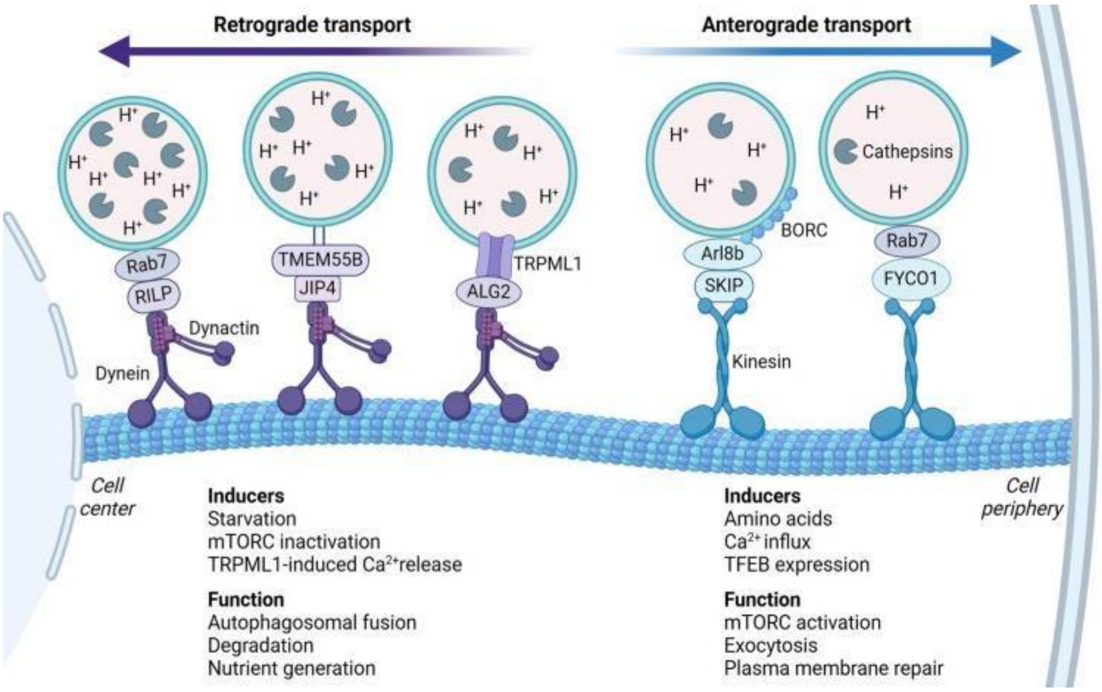

**Figure 1.3. Regulated anterograde and retrograde movement of lysosomes along actin filaments and microtubules and main effector proteins** (Eriksson and Öllinger, 2024).

Kinesins are linked to microtubules and interact with adaptor proteins such as the small GTPases Arl8, Rab7, Rab25, Rab26, Rab27, and Rab38, and the coupling to lysosomes is supported by the octameric BORC complex to the lysosomal surface (Pu et al., 2015; Farías et al., 2017). On the other hand, the retrograde transport of lysosomes is determined by their interaction network with dynein, dynactin, Rab7, lysosomal $Ca^{2+}$ release through the cation-permeable channel TRPML1 (Li et al., 2016), the lysosomal membrane protein TMEM55B, its effector JIP4 (Willett et al., 2017), and the Arl8 effectors, the **RU**N- and **FY**VE-domain-containing RUFY3 and RUFY4 (Keren-Kaplan et al., 2022; Kumar et al., 2022). Finally, the lipid composition of lysosomal membranes, in particular the phosphatidylinositol 3-phosphate (PI3P)-PI4P molecular switch plays an important role in lysosome positioning, and it functions as well as mTORC1 activity (Ebner et al., 2023).

## 1.7 Host-intracellular pathogen interaction

Intracellular pathogens enter host cells via clathrin-mediated endocytosis and phagocytosis by phagocytic cells (e.g. macrophages) or via macropinocytosis (Ribet and Cossart, 2015). Their survival requires an intracellular compartment or the host cytoplasm to replicate and evade the host immune responses. Different strategies have been evolved by pathogens to avoid lysosomal degradation by interfering with the fusion of pathogen-containing vesicles (PCVs) and lysosomes, the formation of autophagolysosomes or phagolysosomes, or inducing the rupture of the phagosomes followed by their release into the cytoplasm (Teixeria et al., 2023). Other pathogens can alter the lysosomal system directly or indirectly either by secretion of effectors or by posttranslational modifications affecting host components of i) the intracellular transport vesicle machinery towards lysosomes such as Rab GTPases, the cytoskeleton, or motor proteins involved in lysosome biogenesis, positioning or autophagy, or ii) the composition of lysosomal membranes, the luminal enzyme content, or the lysosomal pH (Sachdeva and Sundaramurthy, 2020). Few examples are given: after phagocytosis *Mycobacterium* can survive in macrophages by blocking the progression of phagosome maturation through inhibition of the associated Rab5-Rab7 conversion (Rink et al., 2005). Mechanistically a mannose-capped lipoarabinomannan plays an essential role by preventing the recruitment of host Rab5 effectors on the pathogen-containing vacuole. This unique lipid inhibits the generation of phosphatidylinositol 3-phosphate (PI3P) by the PI3Kinase hVPS34 and subsequently the formation of PIP-nanodomains for protein recruitment, as well as the targeting of lysosomal enzymes to the phagosome (Fratti et al., 2001; Spanò and Galán, 2017). PIPs play essential roles in a wide range of cellular processes, such as membrane dynamics, actin cytoskeleton arrangements and vesicle trafficking (Lolicato et al., 2024). Upon *Salmonella enterica* infection, its released effector SopE represents a Rab-specific Guanine Nucleotide Exchange Factor recruiting active Rab5-GTPs to the *Salmonella*-containing vacuoles (SCVs). This conversion promotes the fusion of SCV with early endosomes and it prevents its fusion with lysosomes (Bulgin et al., 2010). This is an example of bacterial survival even after fusion of SCV with host lysosomes. Another effector-dependent strategy to manipulate the lysosomal system has been developed by *S. typhimurium* that blocks the retrograde transport of M6P receptors (MPRs) from endosomes to the Golgi by the effector protein SifA. It causes a hypersecretion of acid hydrolases into the extracellular space and it decreases the intracellular lysosomal degradative activity (McGourty et al., 2012) which is thought to promote bacterial survival upon fusion of SCV with host lysosomes.

# Introduction

Very recently novel molecular insights have been gained in how macrophages manage the efficient elimination of microbes and how bacteria exploit host nutrients via transcriptional regulation. It has been shown that TFEB is transported into the nucleus and it activates the transcription of about 70 lysosomal and autophagy in addition to 400 other genes upon bacterial uptake via phago-lysosomal calcium release (Irazoqui, 2020; Takla, Keshri, Rubinsztein, 2023). Thus, heat-killed *Mycobacterium tuberculosis*, living *Salmonella* Typhimurium and mixtures of lipopolysaccharides (LPS) and interferon-γ induce the nuclear translocation of TFEB. Mechanistically, the bacterial stimuli induce the transcription of the mitochondrial aconitate decarboxylase and increase the production of the itaconate metabolite, which is subsequently transferred from mitochondria into the SCV and inhibits the growth of the pathogen (Schuster, Epple et al., 2022). At the same time, Li and colleagues identified the role of itaconate which directly alkylates TFEB at cysteine 212 and prevents the interaction between TFEB and the cytoplasmic retention protein 14-3-3 by inhibiting the mTORC-mediated TFEB phosphorylation at serine 211. Subsequently, the nuclear TFEB activates lysosomal biogenesis to benefit the bacterial elimination (Zhang et al., 2022). Finally, applying CRISPR screens the ATP-binding cassette transporter G2 (ABCG2) has been identified exporting itaconate from the cytosol into the extracellular space. Therefore, ABCG2 functions as key regulator that limits TFEB- dependent lysosomal biogenesis and antibacterial innate immunity (Chen et al., 2024).

The intracellular pathogen *Legionella pneumophila* requires nutrients, preferentially amino acids, from the host cells for its replication. Upon internalization *L. pneumophila* releases about 300 effector proteins to establish a *Legionella*-containing vacuole (LCV) and to manipulate the host defense system (Wang et al., 2024). Thus, *Legionella* effector protein SetA, that exhibits glucosyltransferase activity, is able to glucosylate TFEB at multiple sites among the serine 138 and threonine 208 adjacent to S142 and S211 phosphorylation sites, resulting in the translocation of TFEB into the nucleus and in the activation of genes for autophagy and lysosomal biogenesis. The data suggest that *Legionella* utilizes not only the proteasomal degradation system, but also the mTORC1 regulated pathway to promote the generation of free amino acids for bacterial consumption. Intestinal mucosae are equipped with a 2-layer gel-like mucus barrier, composed of large heavily O-glycosylated homo-oligomers (mucins) in addition to antimicrobial molecules (e.g. lysozymes or α-defensins), and with specialized sentinel cells continuously sensing the presence of pathogens, such as dendritic cells, macrophages and 'microfold cells' (M cells). Upon infection, enteric pathogens are chemoattracted to the mucus layer and propelling with their flagella through it. They can damage the mucus barrier, whose viscosity obstacles bacterial movement, by releasing enzymes exhibiting mucolytic effects, such as glycosidases which degrade mucin oligosaccharides and expose the mucin peptide backbone to proteases (McGuckin et al., 2011). Underneath the mucus barrier, M cells contribute to the tissutal immunity by transporting antigens collected from the intestinal lumen across the epithelial barrier to the lymphoid tissue underlying it (Peyer's patches). Thus, they are exploited by several bacterial pathogens (e.g. *Y.enterocolitica*, enteropathogenic Gram-negative bacteria) which use them as an easily accessible entry route to deeper host tissutal positions (cyan, Fig. 1.4 A) (Ribet and Cossart, 2015).

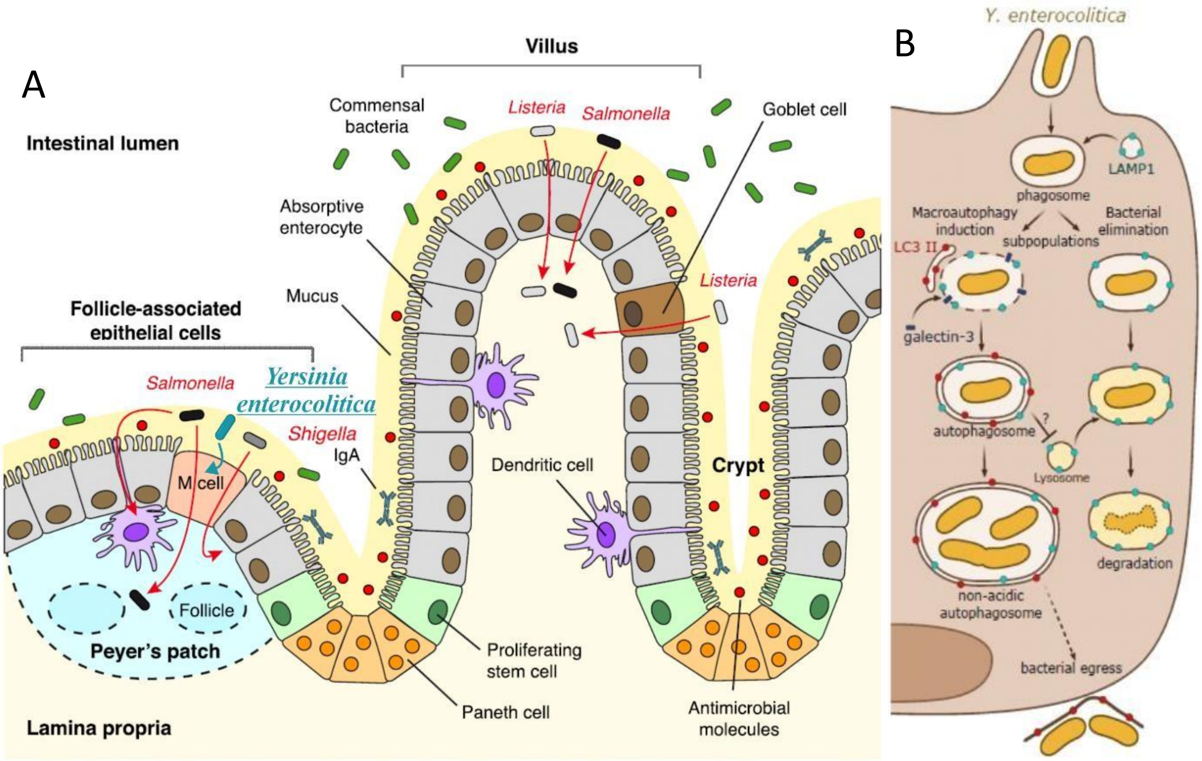

**Figure 1.4.** (**A**) **Intestinal epithelium upon infection with enteropathogenic bacteria (red) entry routes**. *Y.enterocolitica* (cyan) enters through M cells (orange) (adapted from Ribet and Cossart, 2015). (**B**) **Intracellular pathways of *Y.enterocolitica* in epithelial cells**. A half is degraded in lysosomes, the other half survives and replicates in non-acidic compartments (Lemarignier and Pizarro-Cerdá, 2020).

Preferentially entering through M cells, *Yersiniae* replicate intracellularly subverting autophagosome formation to create a niche supporting bacterial replication. It has been reported that *Yersiniae* trigger autophagy in murine macrophages and epithelial cells (Deuretzbacher et al., 2009; Valencia-Lopez et al., 2019). However, while in macrophages autophagy does not support an intracellular replication niche, in epithelial cells the picture is different. Here, *Y.enterocolitica* are taken up from the apical side and undergo two pathways: half of them is described to be internalized and directly degraded in lysosomes, while the other half triggers macroautophagy, survives and replicates in double-membrane non-acidic autophagosomes which cannot fuse with lysosomes, escaping lysosomal degradation. Ultimately, they are released from the non-acidic compartments and egress to continue the infection process (Fig. 3.14 B) (Lemarignier and Pizarro-Cerdá, 2020). The mechanisms for which *Yersinia*-containing compartments fail to fuse with lysosomes are unclear.

## 1.8 Aim of the study

*Yersinia enterocolitica* are pathogenic bacteria that are internalized into epithelial cells of the intestinal tract. The intracellular organelles, the communication between the compartments, the trafficking routes and the transport machinery in phagocytic host cells seem to be important for *Yersinia* replication, survival and elimination, but remained mostly unknown. Over the past 15 years the autophagic pathway, a conserved intracellular catabolic transport and recycling route for macromolecules, defective organelles and pathogens, was shown to be undermined and manipulated by *Yersinia* to bypass lysosomal degradation but create a non-acidic replication niche. The aim of this study was:

- the establishment of more physiological cell models than previously used cell lines e.g. murine intestinal organoids and the murine epithelial intestinal MODE-K cells;
- cell biological and biochemical characterization of intestinal organoids from control and *Gnpt*$^{ki}$ mice with dysfunctional lysosomes and *Gnpt*-edited MODE-K cells;
- proteomic and lipidomic analyses of enriched lysosomal fractions in correlation to functional alterations in control and *Gnpt*-KO MODE-K cells;
- establishment of standard protocols for *Y.enterocolitica* infection protocols on filter-grown MODE-K cells and apical-out converted intestinal organoids.

The deeply characterized intestinal organoids and MODE-K cell models will provide proper tools to study basic molecular mechanisms to maintain lysosomal homeostasis in polarized cells and multi-cellular systems and to discover adaptive mechanisms and altered proteins of the intracellular trafficking machinery upon *Yersinia* infection.

# 2. Materials and Methods

## 2.1 Materials

**Cell culture**: Lipofectamine2000™, Zeocin (Invitrogen); Matrigel® Matrix Basement Membrane Growth Factors Reduced Phenol-Red Free, Cell Strainer 70 µm (Corning); Human recombinant epidermal growth factor (EGF), N-Acetyl-Cysteine, Puromycin dihydrochloride from *Streptomyces alboniger*, Y-27632 dihydrochloride, Poly-L-Lysine, Fibronectin (Sigma); JetPEI DNA Transfection Reagent (Polyplus); 0.2 µm filters FP 30/0.2 CA-S (GE Healthcare Life Sciences Whatman); Ethylenediamine tetraacetic acid disodium salt dehydrate (EDTA), Dimethylsulfoxid (DMSO) (Roth); Dulbecco's Modified Eagle's Medium (DMEM), Advanced DMEM/F12, Fetal Bovine Serum (FBS), GlutaMAX™, Penicillin/Streptomycin (P/S), HEPES Buffer Solution 1M, Dulbecco´s Phosphate Buffered Saline (DPBS), 0.05% Trypsin-EDTA 1X, Hank´s Balanced Salt Solution 10X (HBSS), Opti-MEM I (Gibco).

**Kits:** ROTI Quant universal (Roth); Clarity Western ECL Substrate (Bio-Rad); Cyto-ID Autophagy Detection kit (Enzo Life Sciences); AccuStart II Mouse Genotyping Kit; AccuStart II GelTrack PCR SuperMix (VWR).

**Fluorophore probes:** Bodipy Lactosylceramide complexed to BSA, LysoTracker Deep Red, HCS LipidTOX™ Red Neutral lipid stain, Wheat Germ Agglutinin (WGA) Alexa Fluor555 conjugate (Invitrogen); WGA CF488A conjugate (Biotium); Phalloidin 660 (ThermoFischer Scientific); Filipin complex ready made solution 5 mg/ml, 2-(4-amidinophenyl)-1H-indole-6-carboxamidine (DAPI) (Sigma).

**Microscopy**: Aqua-Poly/Mount (Polysciences Inc); Microscopic Slides Superfrost® Plus Ground Edges 90°, Cover glasses 12 mm (Hecht-Assistant).

**Plastic**: µ-Slide 8 Well Glass Bottom (Ibidi); 24-well plates (ThermoFischer Scientific); Cell scraper, T25 and T75 Tissue Culture Flasks, 60 and 100 mm Tissue Culture Dishes (Sarstedt); Cryo.s™ vials (Greiner); 24-Well Cell Culture Inserts 0.4 µm PET clear (cellQART).

**Other consumables**: Dextran-coated magnetite DexoMAG 40 (Liquid Res. Ltd); Saponin (Fluka); Triton X-100 (Roth); Bovine Serum Albumin, Fraction V (BSA) (Biomol); 4-nitrophenyl-N-acetyl-β-D-glucosaminide (Sigma); DNase/RNase Free Water (ThermoFisher Scientific); Extraction Reagent, Stabilization Reagent (Quantabio).

R-Spondin- and Noggin-overexpressing HEK293 cells, BSA-gold particles, SEP-Lamp1-RFP cDNA were kindly provided by Dr. Calvin Kuo (Stanford University), by Prof. Dr. Judith Klumperman (University Medical Center Utrecht) and by Prof. Juan Bonifacino (NIH, Bethesda, Maryland), respectively. *Y.enterocolitica* infections were performed in the lab of Prof. Ruckdeschel (University Medical Center Hamburg-Eppendorf). *Salmonella serovar thypimurium* STm 4/74 were used in the lab of Prof. Denise Monack (Stanford University) during the internship.

**Antibodies** are listed in **Supplementary Table S5**.

## 2.2 Methods

### 2.2.1 Cell culture and transfection

Murine duodenal epithelial cell clone K (MODE-K) cells (kindly provided by Prof. Philip Rosenstiel (University of Kiel) were maintained in DMEM supplemented with 10% heat-inactivated FBS, 25mM HEPES pH 7.2, GlutaMAX™ and 1% penicillin/streptomycin (complete medium). Heat-inactivated FBS has been generated by incubation of FBS in a water bath at 56 °C for 30 min. Cells were splitted twice a week at a 1:20 ratio until passage 20. For transient transfection, cells were seeded on 12 mm coverslips pre-coated with 0.1 mg/ml Poly-L-Lysine, and transiently transfected next day at confluency ~60-65% with cDNA constructs (0.5 µg) for 24 hrs using Lipofectamine2000™ according to the manufacturers´ instructions. SEP-LAMP1-RFP stable expressing MODE-K cell lines were generated by cloning and transducing the cells with the lentiviral LeGO-expression vector followed by puromycin selection (Weber et al., 2008) by PD Dr. Kristoffer Riecken (University Medical Center Hamburg-Eppendorf).

R-Spondin 1 and Noggin overexpressing HEK293 cells were cultured in DMEM containing 10% FBS and either 0.01 mg/ml puromycin (Noggin) or 0.3 mg/ml zeocin (R-Spondin 1) from passage 1 (P1) to passage 3. From passage 3, R-Spondin 1 and Noggin expressing HEK cells were cultivated in DMEM containing 10% FBS without antibiotics and the conditioned media collected after 4 days in culture. Collected media were centrifuged at 800 xg for 5 min, pooled in a large scale by mixing 4 batches of each around 125 ml as described (Vonk et al., 2020), filtered through 0.45 µm vacuum filtration units (Sarstedt) and frozen at -20 °C aliquoted in 50 ml each.

Cell freezing was performed by rinsing cells grown in T25 flasks with 10 mM Phosphate Buffered Saline (PBS) detaching them with 400 µl Trypsin-EDTA for about 2 min at 37 °C. Trypsin was blocked by resuspension in complete medium, followed by centrifugation at 1200 rpm 5 min (Eppendorf 5804 R). The cell pellet was resuspended in 4 ml freezing medium (90% complete DMEM, 10% DMSO). Aliquots of 1 ml have been filled in cryovials and frozen at -80 °C for 2-4 days and finally stored in liquid nitrogen.

### 2.2.2 Mice

Heterozygous *Gnptab*$^{c.3082insC}$ (*Gnpt*-ki) mice in C57Bl/6 or 129/SvJ genetic background were inbred to yield wild-type (wt) and homozygous *Gnpt*-ki in a mixed background and genotyped for the wt and mutant alleles by PCR (Kollmann et al., 2012). Briefly, each tail biopsy was digested with 50 µl of Extraction Buffer (VWR) and boiled in the Heating Thermo-mixer (HLC) at 95 °C, 200 rpm shaking, 30 min. After cooling it down on ice for 1 min, 50 µl of Stabilization Buffer (VWR) were added, mixed and 1 µl used as template for the genotyping PCR. Forward and reverse primers (FRT-F5 and FRT-R5, 10 µM) were used in a mastermix with AccuStart II GelTrack PCR SuperMix and DNase/RNase Free Water. After the initial denaturation (95 °C 3 min), the PCR programme ran 35 cycles composed of denaturation (95 °C 15 sec), annealing (59 °C 15 sec) and elongation (72 °C 15 sec), followed by the final elongation step (72 °C 5 min). PCR products were loaded (15 µl) on a 3% agarose gel, bands were detected by UV light exposure and mice genotype annotated.

The mice were housed in a pathogen-free animal facility at the University Medical Center Hamburg-Eppendorf, and the removal of the gut was performed according to the institutional and ethical guidelines.

### 2.2.3 Murine intestinal organoid culture

Intestinal crypts were isolated from mouse small intestines and cultivated according to a slightly modified protocol (Mahe et al., 2013). The sedimented crypts (300–400) were resuspended in 50 µl matrigel with epidermal growth factor (EGF) 1:1000 and supplemented with Basal Gut Medium (Advanced DMEM/F12 supplemented with 20 mM HEPES, 1% GlutaMAX™, 1% P/S and 2 mM N-acetyl-cysteine) and conditioned media of R-Spondin 1 and Noggin in a ratio 7:2:1, and placed in a 24-well plate. After incubation of the plates for 20 min at 37 °C to allow matrigel polymerization, 500 µl/well of Basal Gut medium/R-Spondin1/Noggin were added. The medium was replaced every 3 days. The organoids were passaged every 7 days and splitted 1:3 (Mahe et al., 2013).

Organoids freezing was performed by gently resuspending organoids in 500 µl/well of ice-cold DPBS, pooled and collected in a 15 ml Falcon tube and centrifuged at 400 xg for 10 min at 4 °C. The pellet was resuspended in organoid freezing solution (90% FBS and 10% DMSO, supplemented with 10 µM ROCK-inhibitor Y-27362). Organoids from three wells were pooled and transferred into one cryovial. Aliquots of 1 ml have been filled in cryovials and frozen at -80 °C for 2-4 days and finally stored in liquid nitrogen.

### 2.2.4 Immunofluorescence microscopy of organoids

Organoids were seeded in an Ibidi µ-slide 8 Well during the weekly passaging. After 3 days in culture, organoids were fixed with 4% paraformaldehyde (PFA) for 10 min at room temperature and rinsed three times with 10 mM PBS containing 50 mM $NH_4Cl$ for quenching free aldehyde groups after fixation. Organoids were permeabilized using PBS containing 0.2% saponin and 3% BSA (permeabilization buffer) for 1 hr at room temperature and further incubated in permeabilization buffer containing primary antibodies in the given dilution (**Suppl. Table S5**) overnight at 4 °C. After rinsing twice in PBS, the organoids were incubated with respective secondary antibodies (1:1,000) and DAPI (1:1,000) for 2 hrs at room temperature. After three PBS washes, organoids were directly imaged using a confocal Leica TCS SP8 X microscope supported by a Leica LAS X software and images analyzed with ImageJ.

### 2.2.5 Lattice Lightsheet microscopy of organoids

Organoids were prepared and seeded in an Ibidi µ-slide 8 Well during the weekly passaging. According to the manufacturers´ instructions, after 48 hrs in culture the organoids were incubated with 5 µM Bodipy Lactosylceramide complexed to BSA (1:100) in HBSS for 30 min at 4 °C, followed by three washes with ice-cold Basal Gut medium, and 50 nM LysoTracker Deep Red in pre-warmed Basal Gut medium for 30 min at 37 °C. After a quick wash in the same medium, organoids can be imaged using ZEISS Lattice Lightsheet 7 microscope equipped with Zen 3.2 software.

### 2.2.6 Murine and human intestinal organoid polarity reversion, infection and staining (apical-out)

Organoids polarity reversion, infection and stainings were performed at Stanford University School of Medicine (CA) as previously described (Co et al., 2021).

### 2.2.7 Generation of *Gnpt-knockout* MODE-K cells using CRISPR/Cas9

sgRNAs were designed by the SYNTHEGO sgRNA design tool (https://design.synthego.com/#/). DNA oligos containing sgRNA sequences for exon 3 (for CACCGCATGGGCAGACAGAGCCTA; rev AAACTAGGCTCTGTCTGCCCATGC) were annealed and ligated into BbsI-digested pX459 vector (Addgene, #62988). MODE-K cells were transfected with pX459 constructs using JetPEI transfection reagent and selected with puromycin (Sigma). Four days later, single clones were seeded into a 96-well plate, followed by expansion of 40 clones which were tested for missorted β-hexosaminidase by activity measurement in 24-hour conditioned media, and western blotting for the loss of intracellular cathepsin B. Two potential KO clones were genotyped by isolating genomic DNA followed by amplification (Primers: for ACTCTATAGACAAGGCTGTCCTC; rev GTGCATCAGTTGTGGGTTACT), subcloning into pGEM Easy Vector (Promega), and sequencing. Amplicon sequences were aligned to the reference sequence (GRCm39 assembly) using the BLAST analysis tool.

### 2.2.8 Immunofluorescence microscopy of MODE-K cells

MODE-K cells were counted (15.000) with Luna II Automated Cell Counter (Bio-Cat), seeded on 12 mm coverslips pre-coated with 0.1 mg/ml Poly-L-Lysine and cultivated for 48 hrs at 37 °C, 5% $CO_2$. Cells were fixed in 4% PFA for 20 min at room temperature and quenched with 50 mM $NH_4Cl$ for 10 min at room temperature. Cells were permeabilized in permeabilization buffer (PBS containing 0.2% saponin and 3% BSA) for 10 min at room temperature, incubated with the primary antibody in permeabilization buffer at the indicated dilution (**Suppl. Table S5**) overnight at 4 °C and with the appropriate secondary antibody (1:1,000) for 2 hrs at room temperature. DAPI (1:2000) in permeabilization buffer was applied for 10 min at room temperature. Coverslips were mounted on slides using mounting medium.

For Filipin staining, cells were cultivated in complete DMEM for 24 hrs at 37 °C and 5% $CO_2$. Cells were fixed and quenched as above and permeabilized with PBS containing 0.05% Triton X-100 for 10 min at room temperature. The staining was performed using 25 µg/ml of neutral polyene Filipin isolated from *Streptomyces filipinensis* for 45 min at room temperature in the dark, followed by dilutions of primary (overnight 4 °C) and secondary (2 hrs at room temperature) antibodies incubations in PBS (Kwiatkowska et al., 2014). After three washes in PBS, coverslips were mounted on glass slides with Aqua-Poly/Mount and placed overnight under dark condition at room temperature to let the mounting medium tighten. Next day slides were moved to 4 °C. All samples were imaged with the 405 nm laser using a confocal Leica TCS SP8 X microscope supported by a Leica LAS X software and analyzed with ImageJ.

### 2.2.9 Live-cell imaging, tracking, and mean squared displacement (MSD) analysis of MODE-K cells

Control and *Gnpt*-KO MODE-K cells were seeded onto 35 mm glass bottom dishes (Ibidi) a day prior to the experiment. Cells labelling with LysoTracker Deep Red and Bodipy was performed as described above. The cells were imaged using a commercial Zeiss Lattice Lightsheet 7 (Zeiss). The integrated incubation and gas mixer system ensured environmental control (37 °C, 5% $CO_2$, 90%

humidity). The cells were imaged continuously for 120 sec using a 488 nm and 642 nm wavelength laser with a predefined lightsheet of 30 µm x 1000 nm. The LBF 405/488/561/642 filter cube was used. The images were post-processed in Zen Blue's (v.3.8) deskewing function, which utilized the cover glass transformation. The ImageJ Fiji software (Schindelin et al., 2012) with the plugin TrackMate v.7.6.2 (Ershov et al., 2022) was employed for single particle tracking. Short tracks with less than 20 spots were excluded from further analysis. The spot location and radius of each spot were refined using an elliptical orthogonal Gaussian 3D function. Post-processing of the data was carried out with a custom-written code. Radii of spots within a track that could not be redefined were excluded from further analysis, and tracks with more than 50% excluded values. Using a custom-written code, MSD analysis was performed using the MSDanalyzer package (Tarantino et al., 2014) in MATLAB R2021a, v9.10.0.1602886. Statistical analysis and visualization were carried out using GraphPad Prism v.9.5.0.

### 2.2.10 Microtubules posttranslational modifications analysis

For immunofluorescence, 15.000 cells were counted and seeded on 12 mm pre-coated coverslips and cultivated as previously described. Cells were fixed with pre-warmed 4% PFA supplemented with 4% sucrose and 0.25% glutaraldehyde (GA) in PBS for 10 min at 37 °C, washed once with pre-warmed 10 mM PBS for 10 min at 37 °C and quenched with pre-warmed 50 mM $NH_4Cl$ in PBS (pH 8) for 10 min at 37 °C. Cells were washed three times with 10 mM PBS, each for 10 min at room temperature, and stored at 4 °C. Cell extracts for western blot analysis were obtained by seeding cells on 6-well plate (450.000) and cultivating them as previously described. After 48 hrs in culture, cells were washed shortly with ice-cold 10 mM PBS and harvested in 200 µl of ice-cold lysis buffer (20 mM Tris/HCl pH 7.4, 150 mM NaCl, 1% Triton X-100, 1X Protease Inhibitory Cocktail) and incubated in Eppendorf tubes on ice for 1 hr, mixing the tubes gently every 10 min. Samples were centrifuged at 14000 xg for 15 min at 4 °C, supernatants collected and frozen at -20 °C. Both IF and WB analyses were performed by the group of Prof. Marina Mikhaylova (Humboldt University, Berlin).

### 2.2.11 Ultrastructural analysis of murine intestinal organoids and MODE-K cells

After 7 days in culture matrigel containing wild-type and *Gnpt*$^{ki}$ intestinal organoids was resuspended several times by pipetting in ice-cold PBS to break the matrigel droplets followed by centrifugation for 10 min at 400 xg (Mahe et al., 2013). The intestinal organoid pellets were fixed in 4% PFA containing 1% GA overnight at 4 °C.

Confluent MODE-K cells grown on 6 cm dishes for 2 days at 37 °C were fixed by addition of 4% PFA supplemented with 2% GA solution to the culture medium (1:1 v/v) for 15 min at room temperature. The supernatant was discarded and the cells were postfixed with 4% PFA/1% GA overnight at 4 °C. For ultrastructural analysis the organoids and cells were embedded in Epoxy resin as previously described (Richards et al., 2022).

### 2.2.12 Western blotting

Cells were lysed on ice with lysis buffer (150 mM NaCl, 10 mM Tris/HCl pH 7.4, 1% Triton X-100, 1X Protease Inhibitory Cocktail (Sigma)) for 30 min and centrifuged at 16000 xg for 15 min. Supernatant was collected and protein content quantified using BCA protein determination assay (Roth). Aliquots (15-25 µg protein) of the extracts were solubilized in SDS-sample buffer (125 mM Tris/HCl pH 6.8, 1% SDS, 10% glycerol, 10 mM DTT), boiled for 5 minutes at 95 °C, separated by SDS-PAGE and blotted onto nitrocellulose membranes (Amersham Protran) using a self-made Tris-gylcine transfer buffer (25 mM Tris/HCl, 192 mM glycin, 20% v/v methanol, pH 8.7). Samples were analyzed by western blotting with primary antibodies in TBST blocking buffer (25 mM Tris-buffered saline pH 7.4 containing 5% milk powder and 0.05% Tween-20) at the indicated dilution (**Suppl. Table S5**). After incubation with the appropriate HRP-conjugated secondary antibodies, the immunoreactive bands were visualized by enhanced chemiluminescence using the Clarity Western ECL substrate (Bio-Rad). Equal protein loading of the gels was verified by α-tubulin western blotting. Blots were imaged on ChemiDOc Universal Hodd II (Bio-Rad), quantified and analyzed using QuantityOne – 4.6.9 software and ImageLab software 5.1, respectively.

### 2.2.13 *Y.enterocolitica* strain

The strain used was WAc-RFP, originated from a clinical isolate of serotype O:8, WA-314 (Leibiger et al., 2008). Its plasmidless derivative WAc was functionalized with an RFP fluorophore for research purposes.

### 2.2.14 *Y.enterocolitica* infection of MODE-K cells grown on Transwell filters

Transwell filters (6.5 mm diameter, 0.4 µm pore size) were placed in 24-well plate and pre-coated with 200 µl of fibronectin solution (6 µg/ml) overnight at 4 °C. Next day filters were rinsed four times with sterile water and 40.000 cells counted, seeded in each filter and cultivated in complete medium for 48 hrs at 37 °C, 5% $CO_2$. Medium was replaced with fresh medium without P/S before the infection, 2 µl of RFP-labelled bacteria (~$4x10^6$ bacteria, MOI ~3.3) were added to the fresh medium without antibiotics and cells infected 30 min at 37 °C, 5% $CO_2$. Infection medium was removed and cells chased in complete medium (without P/S, but supplemented with 100 µg/ml gentamicin to get rid of extracellular bacteria) for 3.5 hrs at 37 °C, 5% $CO_2$. Chase medium was removed and cells directly fixed with 4% PFA, quenched, permeabilized and stained for Lamp1 at the indicated dilution (**Suppl. Table S5)** as previously described. When CytoID staining was performed, chase medium was replaced for the last 30 min of the chase period with fresh pre-warmed chase medium added with the dye at 1:500 dilution. Fixation, permeabilization and staining followed the procedure described.

### 2.2.15 *Y.enterocolitica* infection in BSA-gold labelled MODE-K cells

Cells were seeded on 6 cm dishes and cultivated in complete DMEM for 2 days at 37 °C, 5% $CO_2$. BSA-gold particles (210 µl used at a starting OD=107) were dialyzed to reach a final OD=5 in dark condition under gentle rotation: firstly, in ice-cold PBS for 6 hrs, then in DMEM supplemented with 1% GlutaMAX™ overnight. Retrieved dialyzed BSA-gold particles were diluted in 2 ml of DMEM supplemented with 1% GlutaMAX™, 1% P/S and 1% FBS-heat inactivated and incubated on cells for 2 hrs at 37 °C, 5% $CO_2$. Cells were chased for 2 hrs in the same media without P/S to prepare them for the following infection with *Y.enterocolitica*.

### 2.2.16 Organoid preparation for proteomic analysis

After 7 days in culture wt and *Gnpt$^{ki}$* organoids were collected in ice-cold DPBS as described above, followed by centrifugation at 400 xg for 10 min at 4 °C (Mahe et al., 2013). The supernatant was removed and the organoid pellets were frozen. In total three replicates of both wt and *Gnpt$^{ki}$* organoids were prepared. Each replicate contained organoids pooled from 7 wells, with an average of 15 organoids per well.

### 2.2.17 Isolation of lysosomal fractions using magnetic beads for proteomic and lipidomic analyses

MODE-K cells ($1.5 \times 10^6$ cells/each plate) were counted and seeded on 10 cm dishes and cultured in complete medium for 48 hrs. At confluency, medium was replaced with fresh complete DMEM supplemented with 10% v/v Dextran-coated magnetite beads DexoMAG40 and further cultivated for 14 hrs. Afterwards the cells were washed three times with 10 mM PBS and chased in complete medium for 4 hrs at 37 °C. The subcellular fractionation and the isolation of magnetite loaded lysosomal fractions were performed using QuadroMACS™ Separator Unit (up to four simultaneous separations) and LS magnetic columns (Markmann et al., 2015; Richards et al., 2022). Five elutions (E1 to E5) were collected in 500 µl each of Elution Buffer (10 mM HEPES pH 7.4, 250 mM sucrose, 1 mM EDTA). Elutions E1 and E2 of each sample were pooled and used for proteomic and lipidomic analyses. Aliquots (15 µl) of the inputs, unbound fractions, each eluted fractions and of the 1 ml fractions of non-eluted material (PBS containing 10% Triton X-100 and 1X Protease Inhibitory Cocktail) were tested by β-hexosaminidase activity. The proteomes were analyzed by Mass Spectrometry in the Winter laboratory (University of Bonn).

### 2.2.18 Measurement of lysosomal pH

Lysosomal pH was measured as previously described (Weinert et al., 2010). MODE-K cells were plated on glass-bottom live-cell dishes (MatTek) 24 hrs before pH measurement. Cells were loaded with 0.5 mg/ml Oregon Green 488-dextran (Life Technologies GmbH) in growth medium overnight, followed by a 2 hrs chase for complete dye delivery to lysosomes. For imaging, the medium was changed to an imaging buffer at pH 7.4. Images were acquired using a Leica Dmi8 Thunder Imager microscope (Leica Microsystems) equipped with a 63x 1.40 NA oil-immersion lens and an Oregon Green filter cube (AHF) with excitation at 440 nm or 480 nm, respectively. In situ pH calibration curves were subsequently obtained for each dish, using isotonic K-based buffers supplemented with 10 µM nigericin and 10 µM monensin after equilibration for at least 2 min for each pH (ranging between pH 3.5 - 6.0) starting with pH 6. Images were analysed using ImageJ, where regions of interest (ROIs) were defined as areas above a defined fluorescence threshold in the acquired images at 440-nm excitation. The mean intensity ratio between 480- (pH-sensitive) and 440-nm excitation (pH-insensitive) was calculated after background subtraction for each ROI. The fluorescence intensity ratios (480/440) as a function of pH were fit to a sigmoid and used to interpolate the pH values from the cells.

### 2.2.19 Enzyme activity measurement

Activities of β-hexosaminidase were measured in cell extracts (5 µg protein),24 hrs conditioned media (15 µl), or from magnetite-loaded cell fractions using 4-nitrophenyl-N-acetyl-β-D-glucosaminide as enzymatic substrate, as described previously (Kollmann et al., 2012).

# 3. Results

## 3.1 Biochemical characterization of *Gnpt*$^{ki}$ murine intestinal organoids

### 3.1.1 Lysosomal size and storage material

Small intestinal organoids from wild-type (wt) and *N*-Acetylglucosamine-1-phosphotransferase *knock-in* (*Gnpt*$^{ki}$) mice were cultured for 3 days, fixed and processed for immunofluorescence microscopic imaging. The co-stainings for the Golgi marker GM130 and the lysosome marker Lamp1 are shown in Fig. 3.1 (A-B).

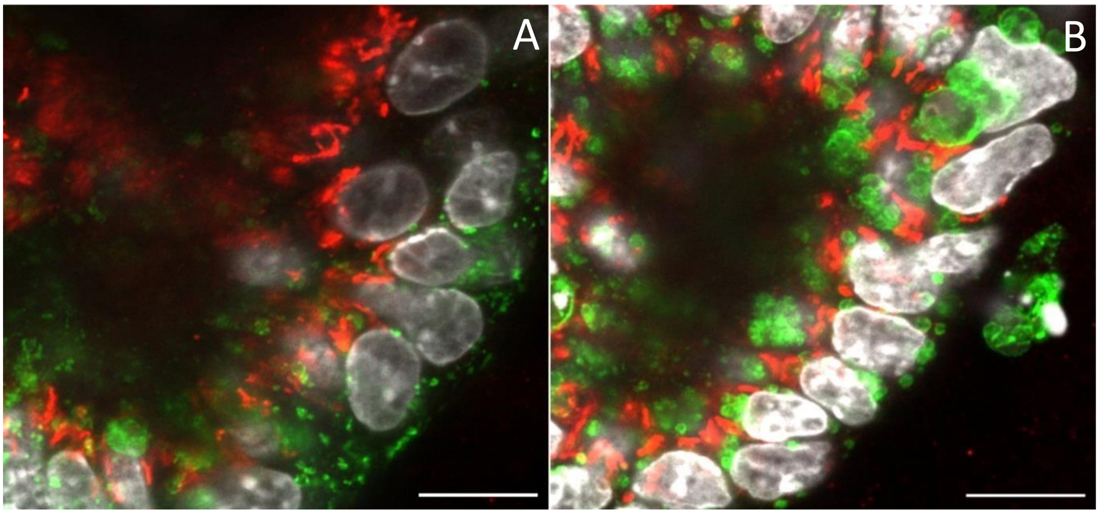

**Figure 3.1. Wt (A) and *Gnpt*$^{ki}$ (B) intestinal organoids co-stained with GM130 (red), Lamp1 (green), DAPI (pseudocolor, white)**. The Golgi apparatus is localized in the perinuclear region of both wt and *Gnpt*$^{ki}$ organoids; lysosomes are significantly enlarged and redistributed beneath the apical surface in *Gnpt*$^{ki}$ organoids. Scale bar 10 µm.

In both genotype organoids the Golgi apparatus was properly localized in the perinuclear region. Lysosomes were visible as small sized punctates distributed throughout wt cells. In *Gnpt*$^{ki}$ organoids lysosomes were enlarged in size and appeared to be organised in clusters which preferentially localised beneath the apical surface, towards the lumens of the organoids. Electron Microscopy (EM) analysis of wt and *Gnpt*$^{ki}$ organoids was performed on 60 nm resin-embedded thin sections (Fig. 3.2 A and B). Significant discrepancies in different cell types could be detected. In wt enterocytes, comprising the majority of intestinal cells, lysosomes were hard to find due to the very thin sectioning. In sections from *Gnpt*$^{ki}$ organoids enlarged lysosomes filled with storage material could be observed. The apical plasma membrane projected short microvilli. Few isolated intestinal secretory Goblet cells were detectable in the epithelial layer which function in the production of the mucus. The secretory granules appeared to be empty primarily because carbohydrate-rich proteins such as mucins rich proteins, such as mucins, were washed out in the preparation of microscopy samples. The electron-density within the granules varied. Secretory granules found in *Gnpt*$^{ki}$ organoids were enlarged in size and more electron-dense. The uniform dark appearance, as mean of electron-density, was mostly due to relatively high content of proteins and other granule-stored products, which normally appear quite homogenously electron-dense.

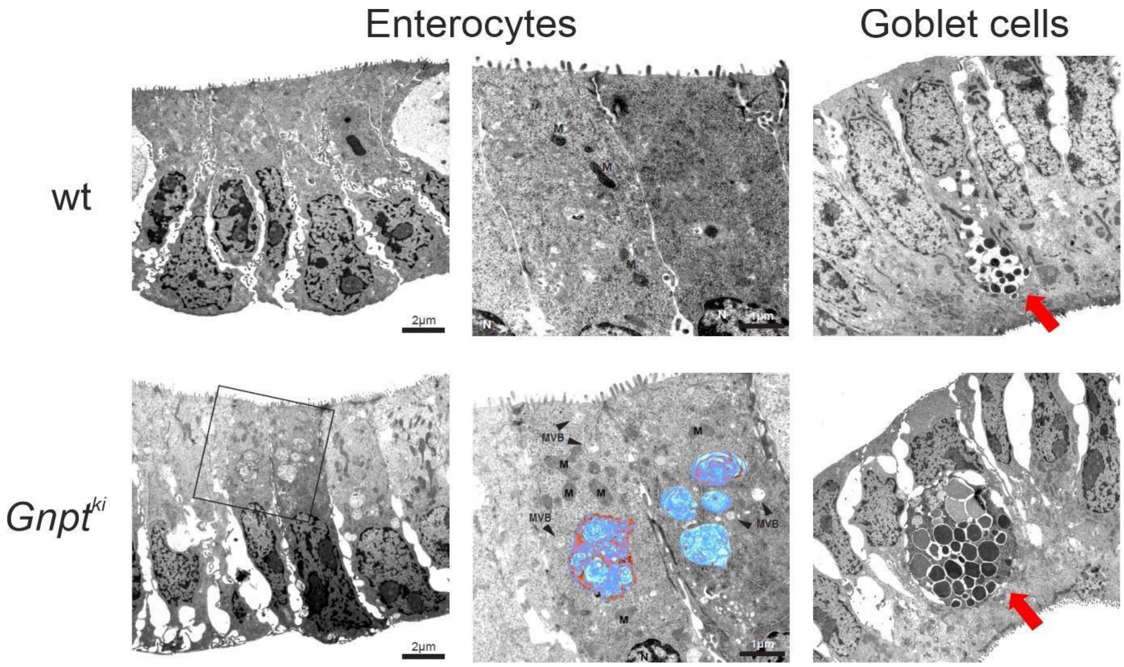

**Figure 3.2. Electron Microscopy images of thin sections of resin-embedded wt and *Gnpt*$^{ki}$ organoids**. In enterocytes of wt organoids (upper images) no lysosomes were detectable (middle magnified image). *Gnpt*$^{ki}$ organoids (lower images) showed several enlarged lysosomes (marked in blue; middle magnified image). In Goblet cells from wt organoids the secretory granule (red arrow) appeared small and mainly filled with carbohydrate-rich proteins, while in *Gnpt*$^{ki}$ organoids the granules were much larger and filled with more electron-dense storage materials. Scale bar 2 µm. M=mitochondria, MVB=multivesicular bodies, N=nuclei.

### 3.1.2 Lysosomal positioning and mobility

To analyze the distribution and mobility of lysosomes in *Gnpt*$^{ki}$ organoids, live-cell confocal imaging was performed using LysoTracker™ Deep Red, a fluorescent dye composed of a fluorescein group and a linked weak base, which can freely cross the cell membrane (maximum emission wavelength of 668 nm) for tracking acidic organelles such as lysosomes. Simultaneously the green fluorescent (Bodipy) labeled sphingolipid lactosylceramide (LacCer) analog was applied to visualize membrane domains in living cells. Live-cell imaging was performed with wt and *Gnpt*$^{ki}$ organoids labelled with LysoTracker Deep Red for 30 min at 37 °C and Bodipy-LacCer for 30 min at 4 °C (the single stacks for both wt and *Gnpt*$^{ki}$ organoids were acquired in continuous mode for 180 sec at 37 °C and 5% $CO_2$, both consist of 113 frames taken at 1.6 frames per second (fps), with an average interval of 0.63 seconds between each frame acquisition). The movies were prepared at 5 fps. The distribution and sizes of LysoTracker-positive lysosomes in wt and *Gnpt*$^{ki}$-organoids were highly similar to those shown in fixed and permeabilized Lamp1-positive lysosomes (compare Fig. 3.1 with Fig. 3.3 A and B). Remarkable differences in the motility of small sized lysosomes in wt cells in comparison to lysosomes of *Gnpt$^{ki}$* cells were observed. Tracking single lysosomes in wt organoids revealed their appearance and disappearance from the focal plane and between the apical and basolateral sides, whereas large-sized and clustered lysosomes of *Gnpt$^{ki}$* cells did not move and were localized beneath the apical plasma membrane (Fig. 3.3 C-D).

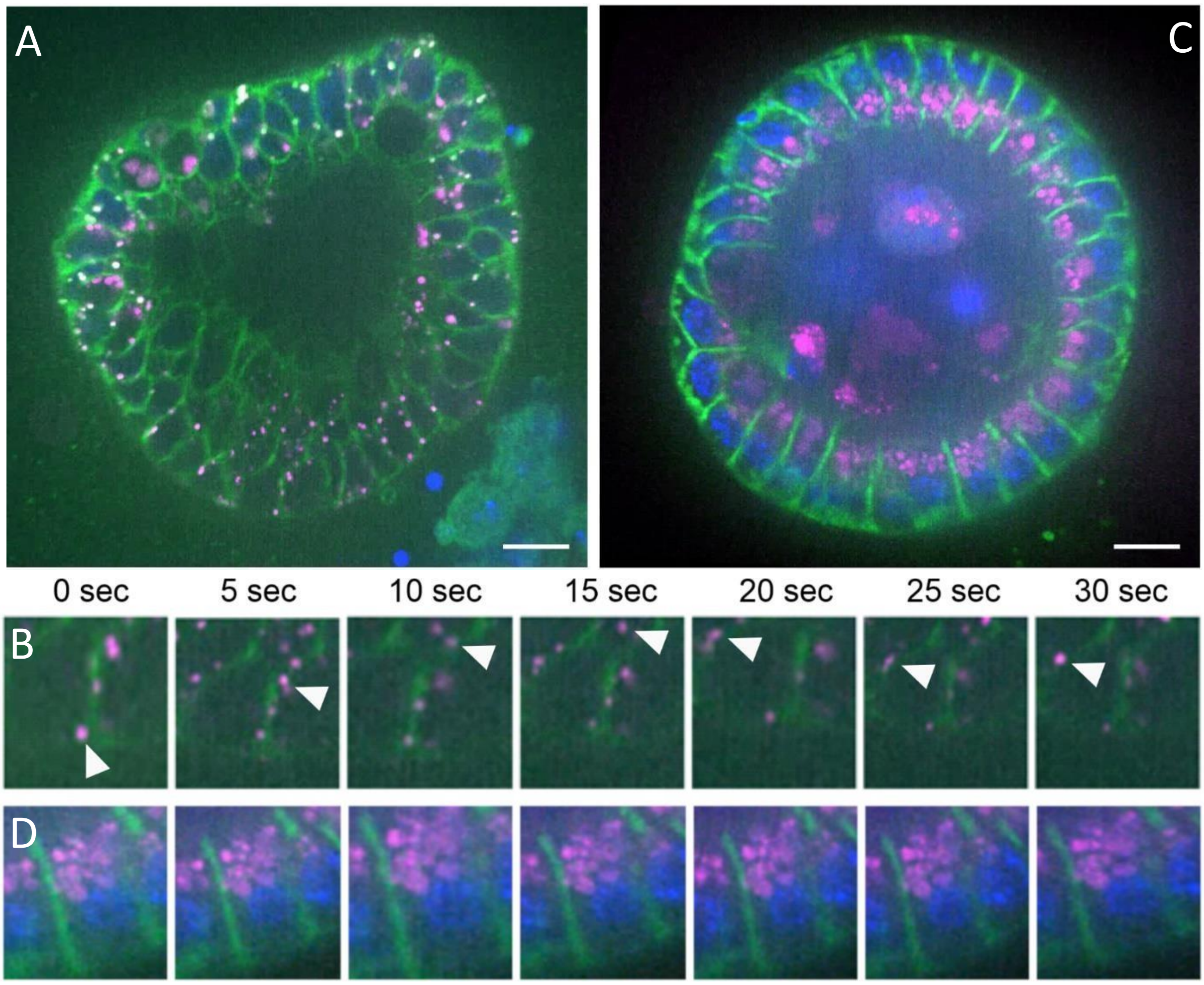

**Figure 3.3. Representative wt (A) and *Gnpt$^{ki}$* (C) organoid images from live-imaging confocal movies (n=3)**. Lysosomes were stained with LysoTracker Deep Red (purple), cell membranes with Bodipy-LacCer (green), and nuclei with Hoechst 33342 (blue). Scale bar 15 µm. Representative snapshots from confocal live-imaging movies showed the mobility of small lysosomes in cells of wt organoids (**B**; white arrowheads) whereas the large-size lysosomes in cells of *Gnpt$^{ki}$* organoids were unable to move (**D**).

The mobility differences were confirmed by live-cell imaging analysis by Lattice Lightsheet (LLS) microscopy, providing a higher resolution and enhancing the quality of the acquisitions resulting in low photo-toxicity to the specimens (Fig. 3.4 A-F). The single planes presented were acquired in continuous mode as part of z-stacks acquisitions, imaged for 15.2 min for wt and 12.5 min for *Gnpt$^{ki}$* organoids at 37 °C and 5% $CO_2$. They consisted of 20 frames for 228 stacks in wt organoids and 58 frames for 65 stacks in *Gnpt*$^{ki}$ organoids, at 1 frame every 0.2 seconds. The movies were prepared at 2 fps.

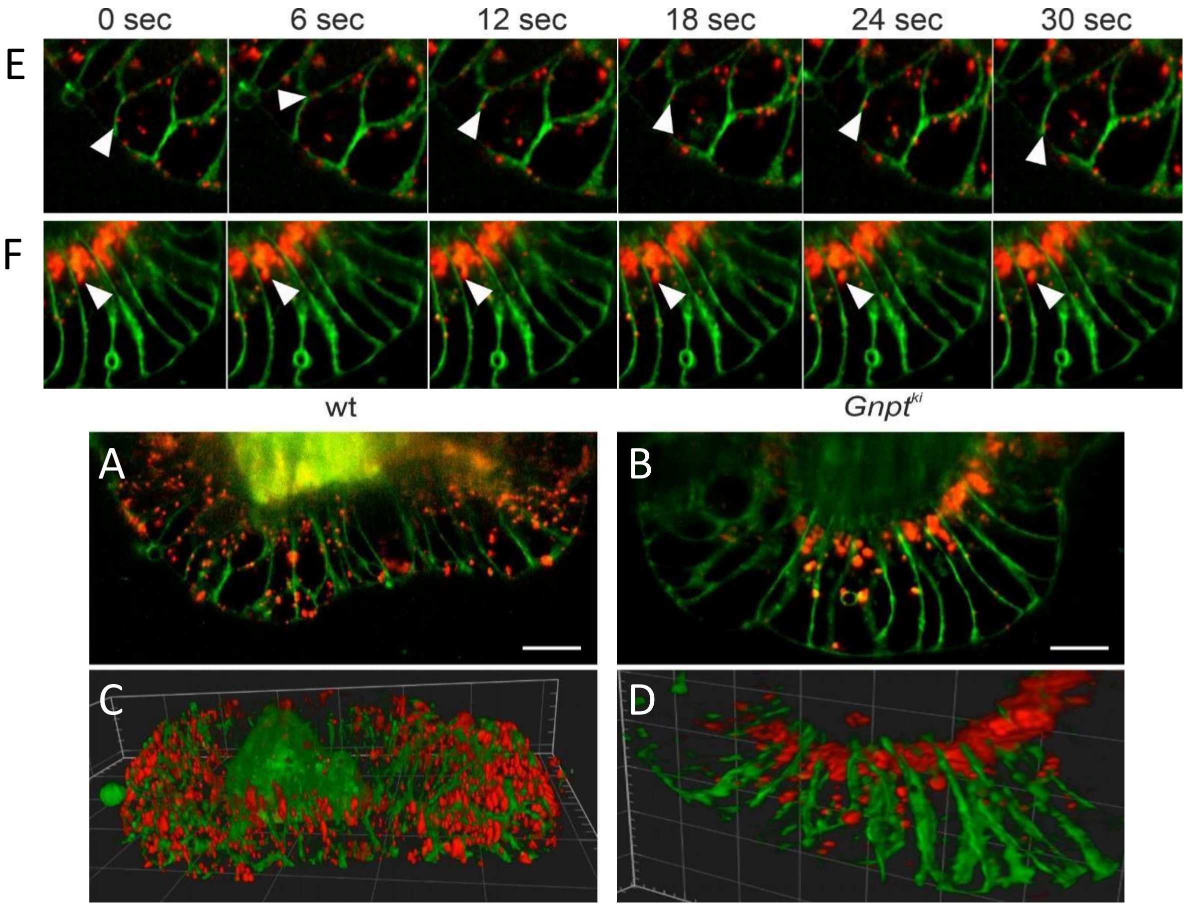

**Figure 3.4. Images from LLS live-cell imaging analysis of wt (A) and *Gnpt*$^{ki}$ (B) organoids**. Lysosomes were stained with LysoTrackerDeep Red (red), cell membranes with BodipyLacCer (green). Lysosomal distribution reconstructions from LLS movies supported the different localization of lysosomes in wt (**C**) and *Gnpt*$^{ki}$ (**D**) organoids. Scale bar 10µm. Representative snapshots from LLS movies showed the mobility of small lysosomes (white arrowheads) in cells of wt organoids tracked over 30 sec (**E**) and the enlarged lysosomes of *Gnpt*$^{ki}$ organoids unable to move (**F**).

The analyses were performed similarly to the confocal life cell imagings (see above) using wt and *Gnpt*$^{ki}$ organoids labelled with LysoTracker Deep Red and BodipyLacCer. Using LLS microscopy differences in mobility of lysosomes between wt and *Gnpt*$^{ki}$ organoids were confirmed. Small sized, evenly scattered lysosomes throughout the cells of wt organoids showed motility in all directions (Fig. 3.4 A-E). The loss of *Gnpt* caused the localization of enlarged and immobile lysosomes and their increased clustering towards the cell periphery beneath the apical side (Fig. 3.4 B-F). Of note, a few numbers of small sized lysosomes in cells of *Gnpt*$^{ki}$ organoids exhibited a slight, short distance mobility. The LLS data allowed also the reconstruction of lysosome distributions, generated by overlapping all the planes of the organoid cells acquired, and clearly demonstrate the differences in the subcellular localization of lysosomes in wt and *Gnpt*$^{ki}$ organoids (Fig. 3.4 C-D).

### 3.1.3 Targeted lysosomal proteome analysis

To biochemically characterize *Gnpt*$^{ki}$ intestinal organoids and investigate contents and properties of enlarged lysosomes, proteome analyses by a Targeted Mass Spectrometry approach were performed. In addition to soluble lysosomal enzymes and accessory proteins, lysosomal membrane proteins and proteins playing a role in lysosomal mobility including their effectors, were separately presented. Volcano plots and western blot analysis are shown in Fig. 3.5, demonstrating the loss of 28 soluble lysosomal enzymes and accessory proteins in *Gnpt*$^{ki}$ organoids, which is most likely caused by the hypersecretion of enzymes lacking M6P tags (Kollmann et al. 2012). Only 5 lysosomal enzymes and co-factors were increased in their abundance in comparison with wt organoids: thiol protease cathepsin B (CtsB), the regulator of lysosomal proteolysis progranulin (Grn), the co-factor for sphingolipid degradation prosaposin (Psap), the exonuclease digesting single-stranded DNA phospholipase D3 (Pld3), and the sphingomyelin phosphodiesterase (Smpd1) converting sphingomyelin to ceramide (Fig. 3.5 A; Suppl. Table S1 A). A selection of lysosomal enzymes which were found to be significantly changed in their abundance between *Gnpt*$^{ki}$ and wt organoids and for which specific antibodies are available, were tested by western blotting. The lysosomal cysteine proteases cathepsin C (CtsC) and cathepsin Z (CtsZ) were not detectable in *Gnpt*$^{ki}$ organoids, whereas CtsB and Grn were slightly increased as expected from the volcano plots (Fig. 3.5 A-B; Suppl. Table S1 A). Of note, the electrophoretic mobility e.g. of CtsB is reduced due to higher amounts of complex (charged) oligosaccharides instead of high mannose-type sugar chains (Kollmann et al. 2012).

Seven lysosomal membrane proteins revealed significant alterations (Fig. 3.5 C and Suppl. Table S1 C), whereas proteins involved in lysosomal mobility did not show an overall changed abundance state, except Arl8 subunits and Borcs7. The function of these proteins is explained in detail below, although the significance of expression is weak (Fig. 3.5 E and Suppl. Table S1 E). Among the lysosomal membrane proteins tested, Lamp1 (#24) revealed to be more abundant in *Gnpt*$^{ki}$ organoids due to the increased size of enlarged lysosomes. No changes in the amounts of the lysosomal v-ATPase subunit Atp6v1b2 were observed between the two genotypes of organoids. In addition, Tmem199 (#19), an accessory component of the lysosomal vATPase, was less abundant, while the chloride exchanger Clc7 (#20), the DNA damage-regulated autophagy modulator protein Dram2 (#21), the lysosomal glycosylated membrane protein Glmp (#22), the lysosomal acetyltransferase Hgsnat (#23) and the nuclear coactivator of iron homeostasis Ncoa4 (#25) were increased (Fig. 3.5 C-D; Suppl. Table S1 C).

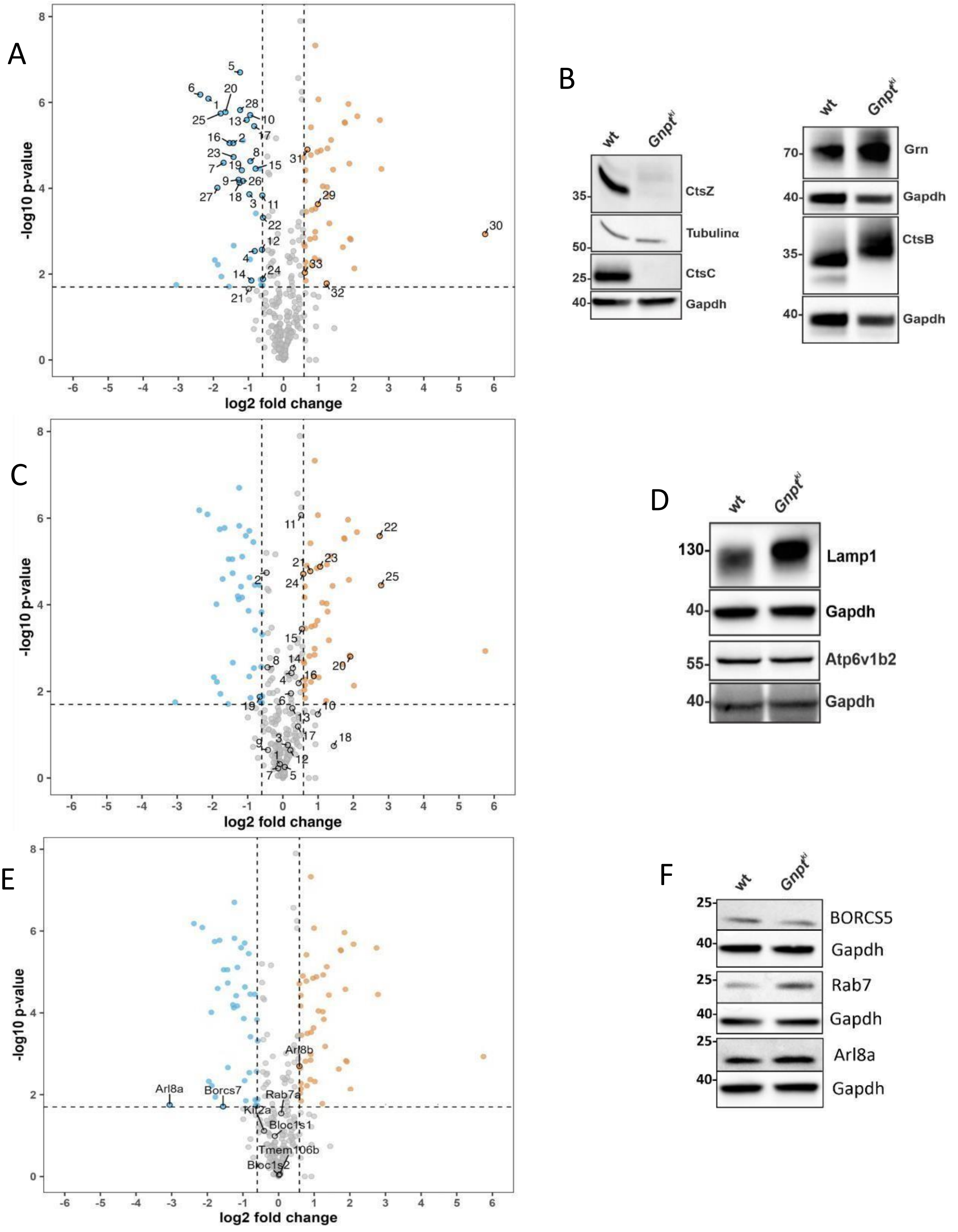

**Figure 3.5. Volcano plots for lysosomal enzymes and soluble accessory proteins (A), lysosomal membrane proteins (C) and proteins involved in lysosomal mobility (E) of *Gnpt$^{ki}$*:wt intestinal organoids (n=3)**. The plots are presented as mean of log2-fold ratio of *Gnpt$^{ki}$*/wt organoids. On the y-axis the -log10 *p*-values of significance are plotted. The dashed lines define the thresholds for statistical significance and abundance. Western blots of selected proteins of the respective proteome categories are shown (**B**, **D**, and **F**). Gapdh was used as loading control.

Moreover, several proteins involved in lysosomal mobility such as the small GTPase Rab7, the Arf-like (Arl) protein Arl8 or the Borcs5 subunit of the octameric BORC complex (Pu et al., 2015), were not significantly changed. In support of these data, they were also tested by immunoblotting and none of them revealed significant alterations (Fig. 3.5 EF).

### 3.1.3.1 Side-directed missorting of lysosomal enzymes

Polarized epithelial cells of the small intestine consist of two specialized apical and basolateral plasma membrane domains which are composed of distinct proteins and lipids and separated by tight junctions (Cao et al. 2012). The loss of multiple lysosomal enzymes in *Gnpt*$^{ki}$ organoids (3.1.3) supported their secretion via the basolateral membrane, because apical secretion of lysosomal enzymes and their trapping in the lumen of organoids cannot be distinguished from enzymes retained intracellularly.

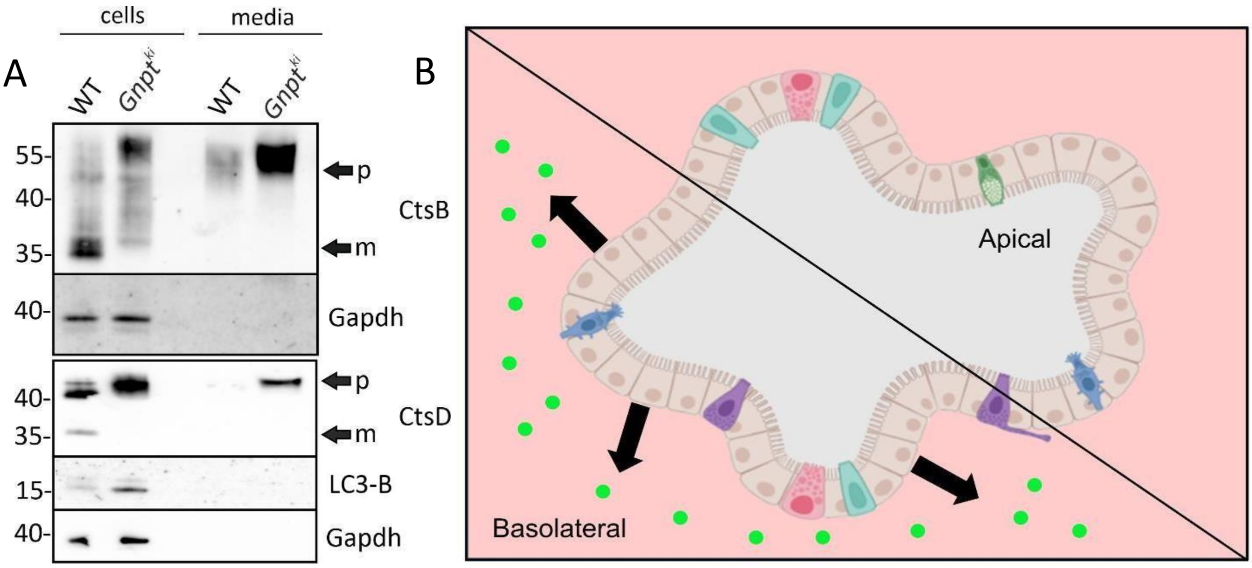

**Figure 3.6. Sorting of lysosomal enzymes lacking M6P residues in *Gnpt*$^{ki}$ organoids.** (**A**) Western blot analysis for CtsB and CtsD of extracts from wt and *Gnpt*$^{ki}$ organoids and their conditioned media. The position of enzymatic active mature (m) and inactive precursor (p) forms are indicated. LC3B is an autophagy marker and Gapdh was used as loading control. (**B**) Schematic representation of the organoid model showing the missorting of lysosomal enzymes (green dots) into the basolateral medium of *Gnpt*$^{ki}$ organoids.

Therefore, the basolateral, serum free medium collected after 24 hrs of conditioning was analyzed by western blotting and compared with respective organoid lysates. Protein immunoblot analysis revealed that extracts of *Gnpt*$^{ki}$ organoids lack mature forms (~35 kDa) of CtsB and cathepsin D (CtsD) (Fig. 3.6 A). In contrast, high amounts of catalytically inactive enzymes (~55 kDa for CtsB and ~47 kDa for CtsD) could be detected in the basolateral media. Since functional lysosomes are prerequisite for the basal autophagy pathway, the organoid lysates were tested for the microtubule- associated protein 1A/1B-light chain 3 (LC3) marker (Asanuma et al., 2003). LC3 western blotting resulted in the detection of two polypeptides of which the LC3-B form represents a C-terminally lipidated molecule inserted in the autophagosomal membrane and causes an increased electrophoretic mobility (Runwal et al., 2019; see 1.2). An increase in the LC3-B autophagosomal membrane marker in lysates of *Gnpt*$^{ki}$ organoids indicates either an enhanced autophagosome synthesis or a block in autophagosome-lysosome fusion (or both). Together, the data showed that the deletion of Gnpt in cells forming the polarized intestinal organoids leads to missorting and loss of newly synthesized lysosomal enzymes via the basolateral membrane, which drastically impair both the degradative capacity of lysosomes filled with non-degraded material and the autophagic pathway in intestinal cells (Fig. 3.6 B).

## 3.2 Analysis of *Gnpt*-knockout (KO) MODE-K cells

### 3.2.1 Generation of *Gnpt*-KO cells

To get a comparable single cell model to the multi-cellular intestinal organoids suitable for e.g. bacterial infection experiments, a KO cell line for the *Gnpt* gene in murine intestinal epithelial MODE-K cells was generated using the CRISPR/Cas9 editing technology. Since no antibodies are available recognizing the murine Gnpt, the CRISPR-mediated loss of Gnpt can be analyzed indirectly only. The known hypersecretion of the lysosomal β-hexosaminidase is characteristic for the loss of *Gnpt*-activity (Vladutiu et al., 1981). The determination of this glycosidase activity is simple, fast and cost-effective and used to identify *Gnpt*-edited cell clones. After puromycin selection, serum-free media conditioned for 24 hrs by 40 single-cell clones were collected and examined for β-hexosaminidase activity. Finally three clones, #3, #7, #10, secreting 3- to 7-fold higher β-hexosaminidase activities than wt cells (Fig. 3.7 A) were further characterized. Afterwards the MODE-K CRISPR clones 3, 7 and 10 were evaluated for the cellular loss of an abundant lysosomal protease, CtsB, that is expected to be reduced or not proteolytically processed to mature forms upon failure in M6P tagging. In wt cells CtsB precursor (45 kDa) is proteolytically activated to the 28 kDa mature form. The mature form was also observed in clone 3 and clone 10, but not in clone 7 (Fig. 3.7 B). Another characteristic parameter of loss of *Gnpt*-activity is the accumulation of non-degraded macromolecules which leads to enlarged and differently positioned lysosomes (Kollmann et al., 2012; see 3.1.1). Therefore clone 7 cells were examined by double immunofluorescence microscopy staining for the lysosomal marker Lamp1 and the terminal GlcNAc-specific Wheat germ agglutinin (WGA). Lamp1-positive lysosomes were found to be enlarged and mostly localized in the perinuclear region of clone 7 cells, and the WGA-intensity was strongly increased and co-localized with Lamp1-lysosomes (Fig. 3.7 C). Ultimately, Sanger-sequencing revealed a single base-pair deletion, G at position 204 in exon 3 which generated a frameshift and a premature stop codon (TGA) after 82 amino acids (c.204delG; p.Leu69Ser*fs*Ter82) (Fig. 3.7 D). All further experiments were performed using clone 7 as *Gnpt*-KO cell line.

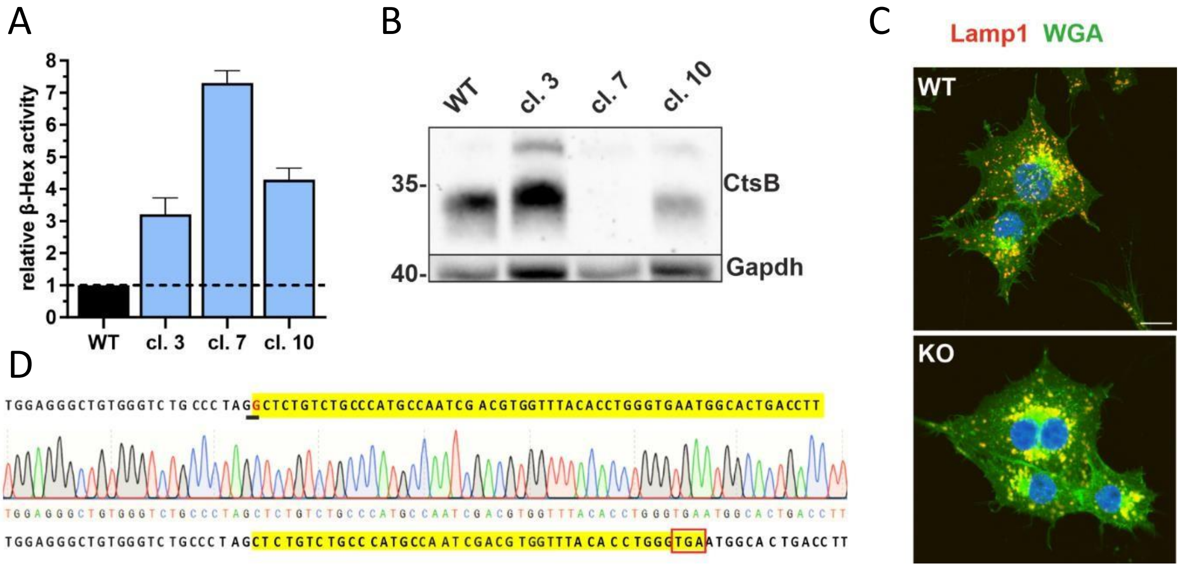

**Figure 3.7. Isolation and characterization of *Gnpt*-KO clones (cl)**. β-Hexosaminidase activity of 24 h conditioned media (media of wt cells were set=1; mean ± SD of 3 experiments) (**A**), and CtsB western blotting of select wt and *Gnpt*-edited MODE-K cell clones. Representative western blot (n=2) is shown with Gapdh as loading control (**B**). WGA and Lamp1 immunofluorescence co-staining of wt and clone 7 cells (**C**). Sequencing and premature stop codon, indicated by a red rectangle, in exon 3 of clone 7 cells (**D**). Scale bar 10 µm.

### 3.2.2 Lysosomal size and storage material

The missorting of newly synthesized lysosomal enzymes and their intracellular deficiency in *Gnpt*-KO MODE-K cells resulted in lysosomes enlarged in size and filled with non-degraded storage material. Analysis of wt and *Gnpt*-KO cells by IF microscopy revealed significant increases in lysosome sizes shown by Lamp1 staining, as well as in their cellular distribution (Fig. 3.8 A-B). In wt MODE-K cells small and evenly distributed lysosomes were observed (Fig. 3.8 A), whereas Lamp1-positive structures of increased sizes were preferentially localized in the perinuclear region of *Gnpt*-KO cells (Fig. 3.8 B). Individual enlarged lysosomes which are typical of *Gnpt*-KO cells were often hard to resolve, appeared as aggregated structures and prevented calculations of their number. First, the relative total cell Lamp1-fluorescence intensity, has been determined using Fiji ImageJ, which combines both the number and sizes of lysosomes. The mean of the total Lamp1-fluorescence per cell (n=25 cells of each genotype out of 3 independent experiments) was significantly increased by 23.5% in *Gnpt*-KO than in wt cells (Fig. 3.8 A-C). To quantitatively assess whether the loss of Gnpt is correlated with the subcellular distribution of lysosomes, the content of Lamp1-fluorescence was analyzed as a function of their distance from the nucleus.

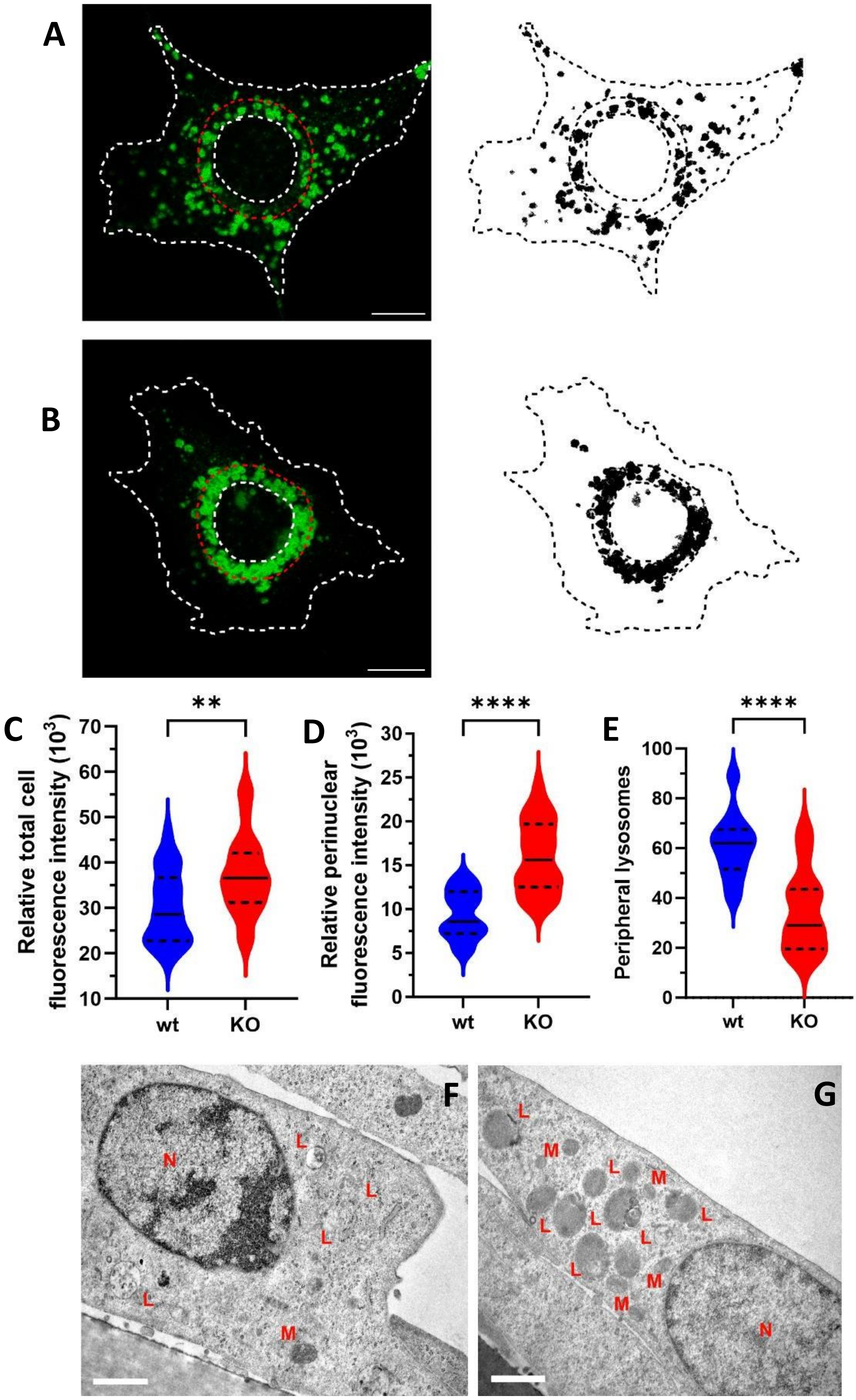

**Figure 3.8. Enlarged lysosomes filled with non-degraded storage material in *Gnpt*-KO MODE-K cells**. Lamp1 (lysosomes, green) staining of wt (**A**) and *Gnpt*-KO cells (**B**) and their respective masks are shown. Scale bar, 10 µm. Lysosomal relative total cell fluorescence intensity (**C**), relative perinuclear fluorescence intensity (**D**) and number of peripheral lysosomes in wt and *Gnpt-KO* MODE-K cells (**E**) (n=25 cells per genotype). Unpaired t- test, ***p*-value <0.05, **** *p*-value <0.0001. Ultrastructural analyses confirmed the reduced number of small sized lysosomes partially filled with electron-light vesicles in wt (**F**) and a higher number of enlarged electron- dense lysosomes in *Gnpt*-KO cells (**G**). Scale bar, 1 µm. N= nuclei; L= lysosomes; M= mitochondria.

The boundary was fixed outward a 3 µm-increment to create a concentric ring separating the preferential perinuclear from peripheral lysosomes (red dotted lines in Fig. 3.8 A-B). The respective black and white dot masks of the Lamp1-fluorescence represent individual lysosomes (Fig. 3.8 A-B). The mean relative fluorescence intensity in the perinuclear region of *Gnpt*-KO cells was higher by 70% compared to wt cells (Fig. 3.8 D). Correspondingly, the average number of peripheral lysosomes were almost 2-fold higher in wt than in *Gnpt*-KO cells (Fig. 3.8 E). Transmission electron microscopy (TEM) images were in line with these findings demonstrating few small lysosomes (if they are detectable in these thin sections at all) lacking any storage material (Fig. 3.8 G). In contrast, in *Gnpt*-KO cells increased number and enlarged electron-dense lysosomes filled by storage material were observed (Fig. 3.8 G). All together, these data demonstrate that the loss of Gnpt in MODE-K cells results in an increased number of enlarged lysosomes, mostly compact gathered in the perinuclear region.

### 3.2.3 Lysosome proteomes of *Gnpt*-KO MODE-K cells

To identify the complete lysosomal proteome, magnetite-based MS analyses have been performed with wt and *Gnpt*-KO MODE-K cells. This method has been established and successfully applied in the laboratory in collaboration with the MS-group of Prof. Dominic Winter at the University of Bonn. The cells were incubated with magnetic dextran beads in triplicate (n=3) and followed by magnetic isolation of the dextran-containing lysosomes and MS (Thelen at al., 2017). Soluble lumenal lysosomal enzymes and accessory proteins, lysosomal membrane proteins and proteins involved in lysosomal mobility were analyzed separately. These data are presented as Volcano plots, tables of proteins of interest and select immunoblots. In Fig. 3.9 A, the Volcano plot revealed a significant loss of 24 lysosomal enzymes and accessory proteins in isolated lysosomal fractions of *Gnpt*-KO cells (Suppl. Table S2 A), as expected due to the hypersecretion of those proteins lacking M6P tags (Kollmann et al. 2012; Markmann et al. 2015). Both the intracellular loss and strongly impaired catalytic maturation, and the hypersecretion into the culture media of *Gnpt*-KO cells have been verified by western blotting for two lysosomal proteases, the aspartic protease CtsD (#24) and the cysteine protease CtsZ (#6; Fig. 3.9 B). Only 4 lysosomal proteins and co-factors (thiol peroxidase Prdx6 (#25), phospholipase D3 Pld3 (#26), ganglioside activator protein Gm2a (#27) were increased in their lysosomal abundance in comparison to wt cells (Fig. 3.9 A; Suppl. Table S2 B). These data were not further verified. Among the 25 proteins reported to be involved in lysosomal mobility (Scerra et al., 2022; Eriksson et al., 2024), only 3 were significantly changed (Fig.

3.9 C; Suppl. Table S2 C).

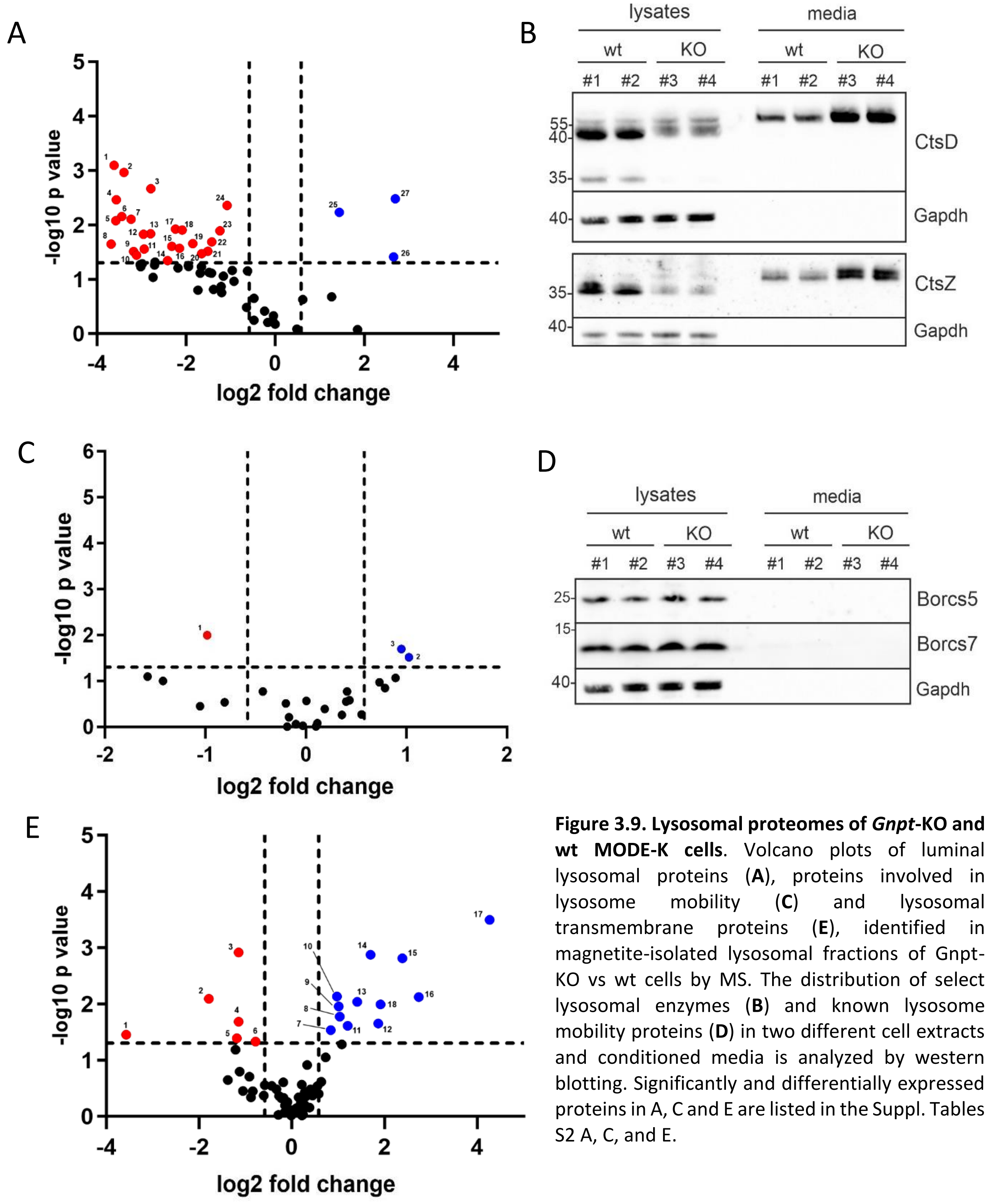

**Figure 3.9. Lysosomal proteomes of *Gnpt*-KO and wt MODE-K cells**. Volcano plots of luminal lysosomal proteins (**A**), proteins involved in lysosome mobility (**C**) and lysosomal transmembrane proteins (**E**), identified in magnetite-isolated lysosomal fractions of Gnpt-KO vs wt cells by MS. The distribution of select lysosomal enzymes (**B**) and known lysosome mobility proteins (**D**) in two different cell extracts and conditioned media is analyzed by western blotting. Significantly and differentially expressed proteins in A, C and E are listed in the Suppl. Tables S2 A, C, and E.

The cytoskeletal GTPase Septin-9 (Sept9; #1) was reduced in abundance in the lysosome fractions of *Gnpt*-KO cells, whereas cytoplasmic dynein 1 heavy chain 1 (DYHC1; #2), an ATPase motor protein involved in the retrograde transport of lysosomes, and the kinesin-1 heavy chain KINH/Kif5b (#3), required for the anterograde transport of lysosomes, were increased. However, the most of known players for the mobility and positioning of lysosomes were not significantly changed in the lysosomal proteome of *Gnpt*-KO cells. This has been exemplary confirmed by western blotting for two unchanged subunits of the BORC complex, Borcs5 (Myrlysin) and Borcs7 (Diaskedin) (Fig. 3.9 D).

Among the 64 lysosomal transmembrane proteins identified, only 6 were decreased in abundance, namely the Transmembrane protein 192, Tmem192 (#1), Lamp1 (#2), the glycosylated lysosomal membrane protein Glmp (#3), the heparan-alpha-glucosaminide N-acetyltransferase Hgsnat (#4), the lysosomal L-histidine exporter Slc15a4 (#5), and the lysosomal trafficking and acidification factor Tmem106b (#6). Significant increases in the concentration of Tmem127,-9b (#7; #13), Sorting nexins (Snx)-2 (#8), -6 (#10), -27 (#14) proteins involved in several stages of intracellular trafficking characterized by a phospholipid-binding domain, the lysosomal lipid transporter Abca2 (#12), the potassium-chloride cotransport channel Slc12a4 (#9), the subunits of the volume-regulated anion channel (VRAC) Lrrc8e (#11) and Lrrc8a (#15), the lysosomal-associated transmembrane protein Laptm4b (#16), the catalytic component of the ATPase flippase complex Atp10b (#17) and the low-density lipoprotein receptor Ldlr (#18) were observed (Fig. 3.9 E). The biological significance of the changes of lysosomal membrane proteins for the lysosomal functions in MODE-K *Gnpt*-KO cells is unclear yet.

### 3.2.4 Lysosomal pH determination

The subcellular localization and functions of lysosomes have been described to correlate with their luminal pH (Johnson et al., 2016). To determine whether the missorting, defects in proteolytic processing and catalytic activities of lysosomal enzymes in *Gnpt*-KO cells are accompanied by changes in lysosome acidification, the luminal pH at steady-state was assessed by two independent experimental approaches. First, the superecliptic pHluorin (SEP) fused to the luminal domain of LAMP1-RFP (Farías et al., 2017) was lentivirally and stably expressed in wt and *Gnpt*-KO MODE-K cells (Fig. 3.10 B). The SEP domain fluoresces at neutral pH and it is quenched at pH <6. Both in wt and *Gnpt*-KO cells the lysosomes were positive for RFP but negative for SEP fluorescence. This indicates that in both cell types the lysosomes were acidic (Fig. 3.10 A). The stronger RFP signal of *Gnpt*-KO cells is due to the increased number of enlarged lysosomes. The green SEP fluorescence on the plasma membrane of both cell types resulted from the SEP domains directed to the extracellular space (pH 7.4) of a minor populations of SEP-LAMP1-RFP fusion proteins transported via the plasma membrane with slower kinetics to lysosomes (Carlsson et al., 1992).

In a second experimental approach the lysosomal pH was measured in collaboration with the group of Prof. Tobias Stauber (Medical School Hamburg) by ratiometric fluorescence microscopy using a standard pulse-chase protocol with the pH-sensitive Oregon green 488-dextran dye (Steinberg et al., 2010). The Oregon green 488-dextran loaded cells were excited alternately through 440 nm (pH-insensitive) and 480 nm (pH-sensitive) filters. At the end of each experiment, an *in situ* calibration was performed. The quantification of the mean fluorescence intensity ratios 480/440 as a function of pH were used to interpolate the pH values from the cells. (Fig. 3.10 C). Unlike wt cells, the prevalent perinuclear lysosomal distribution observed in *Gnpt*-KO cells did not influence the lysosomal acidification. The data clearly showed unchanged pH values between the two genotypes, which were measured to be 4.4 ± 0.1 in both the cell lines (Fig. 3.10 D).

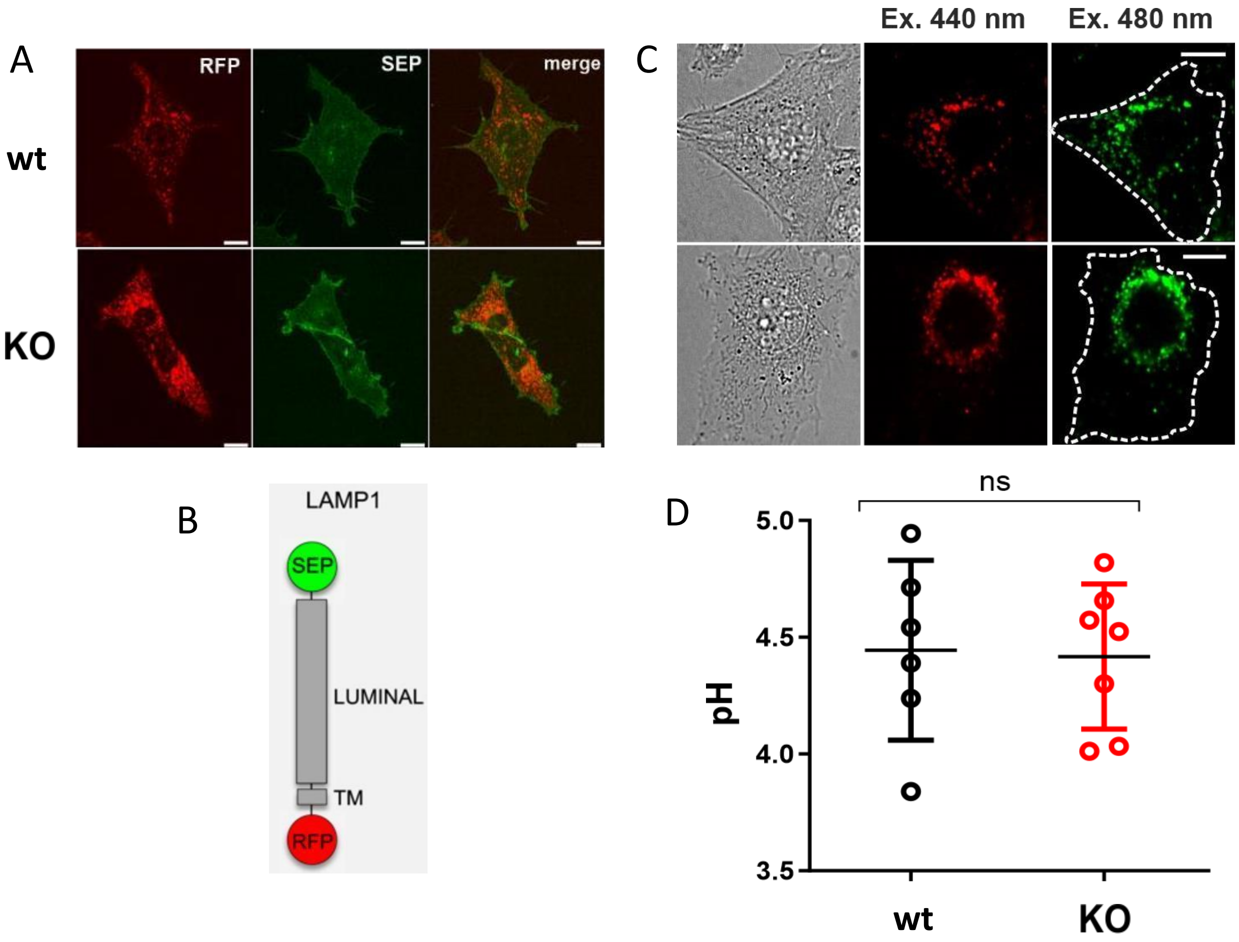

**Figure 3.10. Lysosomal pH measurements of *Gnpt*-KO MODE-K cells**. (**A**) Confocal immunofluorescence microscopy of stably lentiviral expressed SEP-LAMP1-RFP (**B**) construct did not reveal differences between wt and KO cells. (**C**) Representative images showing dextran-coupled pH-sensitive Oregon green 488 in lysosomes of wt and *Gnpt*-KO cells. Individual lysosomal pH was measured by ratiometric fluorescence microscopy based on pH calibration plots. (**D**) Graphical representation of absolute values of lysosomal pH is shown in a scatter plot, representing mean ± SD from several independent experiments (n=6 for wt and n=7 for KO). In each experiment >100 cells per genotype were analyzed. Scale bar 10 µm.

### 3.2.5 Lysosomal positioning and mobility

To analyze the distribution and mobility of lysosomes in MODE-K cells, live-cell confocal imaging was performed staining lysosomes with LysoTracker™ Deep Red on pre-loaded cells with 10 kDa dextran-AF488. Dextran is a polysaccharide internalized by macropinocytosis and used as terminal, stable endolysosomal/lysosomal compartment marker co-localizing with Lamp1 (Fig. 3.11 A-B). In addition, Dextran-AF488 aimed to analyze whether lysosomes of *Gnpt*-KO cells, filled with storage material, could be labelled. As shown in Fig. 3.11 A-B, lysosomes of wt cells (A) appeared small sized, actively moving (not shown) and more widely distributed (see 3.2.2). In *Gnpt*-KO cells (B) lysosomes were preferentially localized in the perinuclear region and displayed impairment in movement.

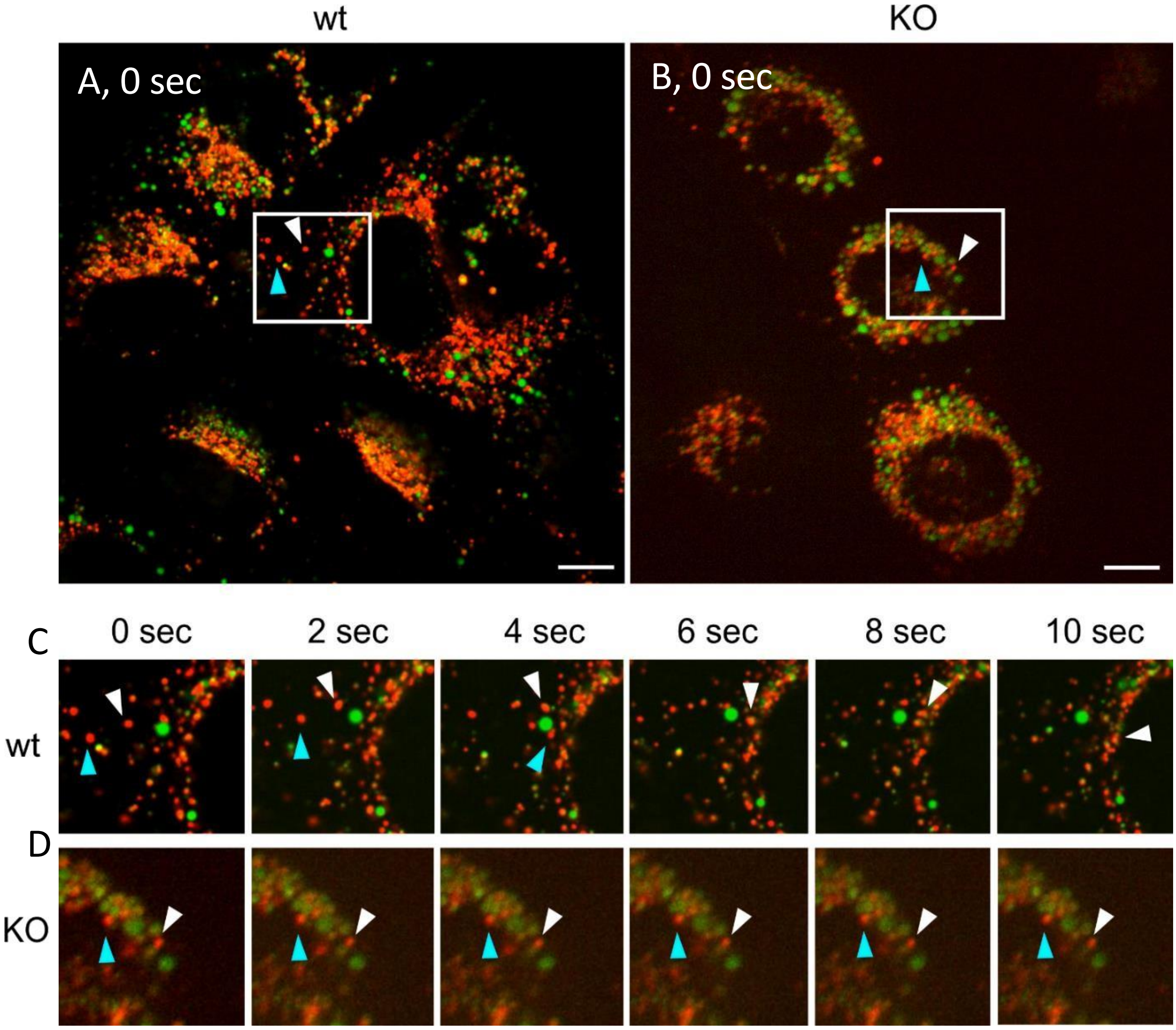

**Figure 3.11. Distribution and mobility of lysosomes in wt and *Gnpt*-KO MODE-K cells**. The images were taken from live-imaging movies performed by pre-loading wt (**A**) and *Gnpt*-KO (**B**) cells with dextran-AF488 (green) and labelling lysosomes with LysoTracker Deep Red (red). The white squares (A-B), representing timepoint 0 sec, indicate the chosen areas in which lysosomal movement was followed over time and presented as sequence of stills in (**C** and **D**). Movements of two wt and two KO lysosomes over time are indicated by the white and cyan arrows. The single time frames in C were cropped from the wt and KO cells live-imaging movie (15 fps), every 2 seconds. Scale bar 10 µm.

In Fig. 3.11 C, a sequence of stills from live-imaging movies allowed tracking 2 lysosomes in wt and 2 lysosomes in KO cells over time (acquired in continuous mode for 35 sec at 37 °C and 5% $CO_2$, both consist of 150 frames taken at 1 frame every 0.23 sec, 4.35 fps). The movies were prepared at 15 fps. The first timepoint 0 sec shown of wt cells in Fig. 3.11 C, both lysosomes were found almost at the periphery of the cell (borders not shown). Over the 6 stills, in 10- second time it was possible to observe their movements towards the microtubule minus end, or perinuclear region. The lysosome indicated by the white arrow moved slightly upwards, to turn around the dextran-AF488-containing vesicle, and proceeded on its run towards the perinuclear region. The lysosome marked by the cyan arrow moved towards the dextran-AF488-containing vesicle, and disappeared between the 4 and 6 sec frames moving to another plane of the cell. To quantify the lysosomal sizes precisely and analyze the lysosomal mobility differences found between wt and *Gnpt*-KO cells, single-particle tracking analyses have been performed in collaboration with Prof. Jens Bosse (Center for Structural Systems Biology (CSSB, Hamburg). The single-particle 4D analyses (Fig 3.12, A-C) were performed by staining lysosomes with LysoTracker Deep Red and imaging continuously for 120 sec with a Lattice Lightsheet microscope. The data revealed significant differences in the radius of lysosomes of wt (0.58 µm ± 0.1) and *Gnpt*-KO cells (0.61 µm ± 0.1) (Fig. 3.12 A); of note, not all lysosomes in the imaged cells were considered for the analysis as just those which could be tracked for the whole acquisition were analyzed. However, despite the size difference does not seem notable, the elevated number of lysosomes analyzed (n=6900 for wt; n=6370 for KO) gives significance to the data.

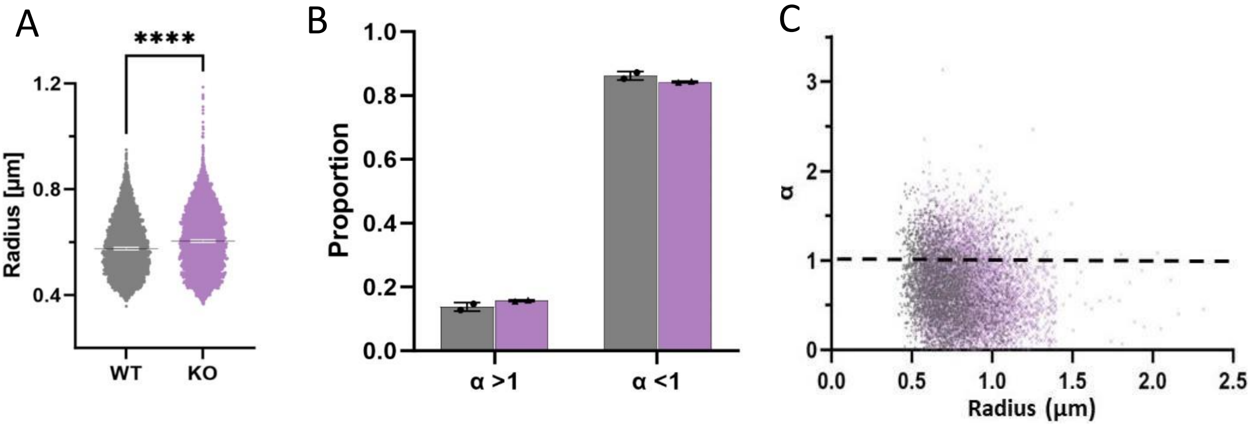

**Figure 3.12. Single-particle 4D analyses of lysosomes of MODE-K cells**. The average lysosomal radius of wt (grey) and *Gnpt*-KO (purple) cells were determined from 4 independent experiments (**A**), Kolmogorov-Smirnov test, *p*- value <0.001. (**B**) Portions of actively transported lysosomes (given as α>1 values) and diffusive transported lysosomes (α<1); (**C**) correlation between lysosomal radius and actively transported lysosomes.

No significant differences in the portion of actively (ATP-dependent) transported lysosomes (α, alpha) were observed in wt and *Gnpt*-KO cells (Fig. 3.12 B). The α values were plotted related to the proportion of lysosomes analyzed after the Mean Squared Displacement (MSD), a statistical mechanics tool to reliably measure over time the deviation of a particle position in relation to a reference position. Alpha values >1 indicated active transport, while values <1 meant no active transport (diffusion events) (Fig. 3.12 B). In addition, the data were also plotted relating the radius of each lysosome to its α value, to clearly show any possible correlation between size and active transport (Fig. 3.12 C). However, wt and KO lysosomes displayed a similar distribution, as most of the puncta (representing single lysosomes) concentrated in the same area of the plot. Remarkably, lysosomes of KO cells were slightly shifted on the x-axis to higher radius values in comparison to wt lysosomes, supporting the data shown in Fig. 3.12 A concerning the increased lysosomal size in KO cells. It has been reported that the mobility of lysosomes on detyrosinated microtubules is impaired (Mohan et al., 2019), therefore post-translational modifications (PTM) on microtubules in wt and *Gnpt*-KO MODE-K cells were examined in collaboration with the group of Prof. Marina Mikhaylova (Humboldt University, Berlin). Several PTMs on tubulin were analyzed and compared between the genotypes. Among them acetylation, tyrosination/detyrosination, delta 2-tubulin (Δ2), and polyglutamylation (polyE) were included. α-Tubulin was reported as the major cytoplasmic target for acetylation, canonically occurring at a lysine residue (Lys40) on the microtubule lumenal surface.

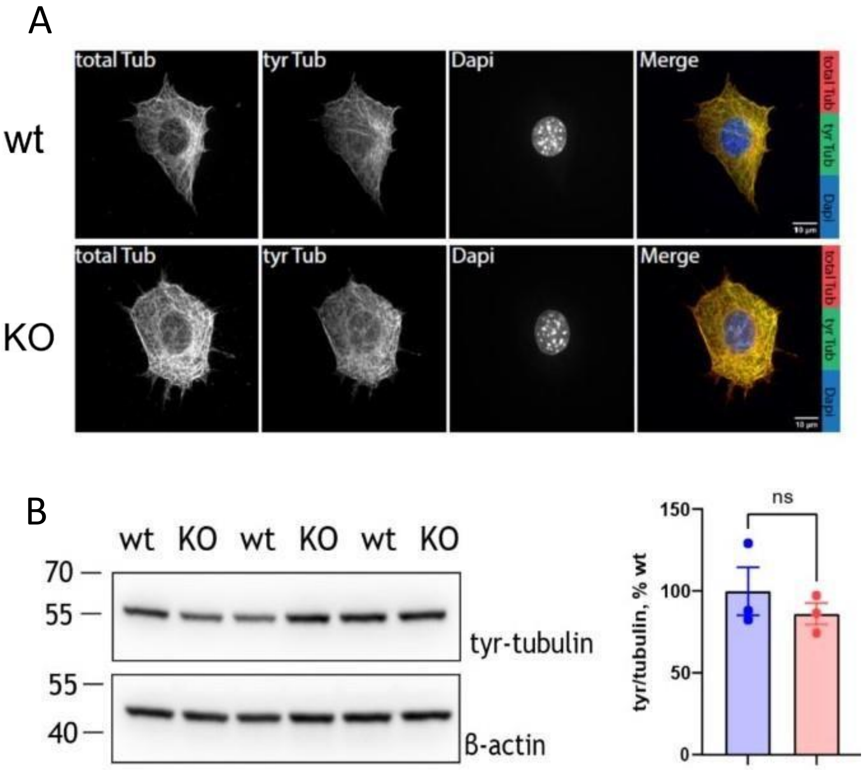

**Figure 3.13. Microtubules tyrosination analyses on wt and *Gnpt*-KO MODE-K cells**. Immunofluorescence analysis (**A**) and quantified western blotting (**B**) are shown (n=3). Mann Whitney U test. Scale bar 10 µm.

Most α-tubulins also contain a terminal tyrosine which, being exposed, could be easily modified: tyrosination and detyrosination take place on this tyrosine residue and represent key modifications, as their turnover defines distinct subcellular compartments and regulates proteins interactions with microtubules. Δ2 tubulin represents a tubulin variant that lacks a carboxy-terminal glutamyl-tyrosine group which cannot be re-tyrosinated Biochemical and microscopic analyses suggested that there were no significant differences in tyrosinated (Fig. 3.13 A) and acetylated (not shown) tubulins between wt and *Gnpt*-KO cells. In addition, quantified tyrosinated-tubulin immunoblotting revealed no significant changes between the genotypes (Fig. 3.13 B).

### 3.2.6 Lysosomal lipidomes

The lysosome proteome analysis of the MODE-K *Gnpt*-KO cells revealed a significant reduction of 9 lysosomal proteins (Abhd6, Hexb, Arsa, Neu1, Smpd1, Npc2, Psap, Asah1, Pla2g15) involved in lipid degradation (3.2.3). Therefore, it can be expected that partially or non- degraded lipids will either be stored in the lumen of lysosomes and/or will change the composition of the lysosomal membranes.

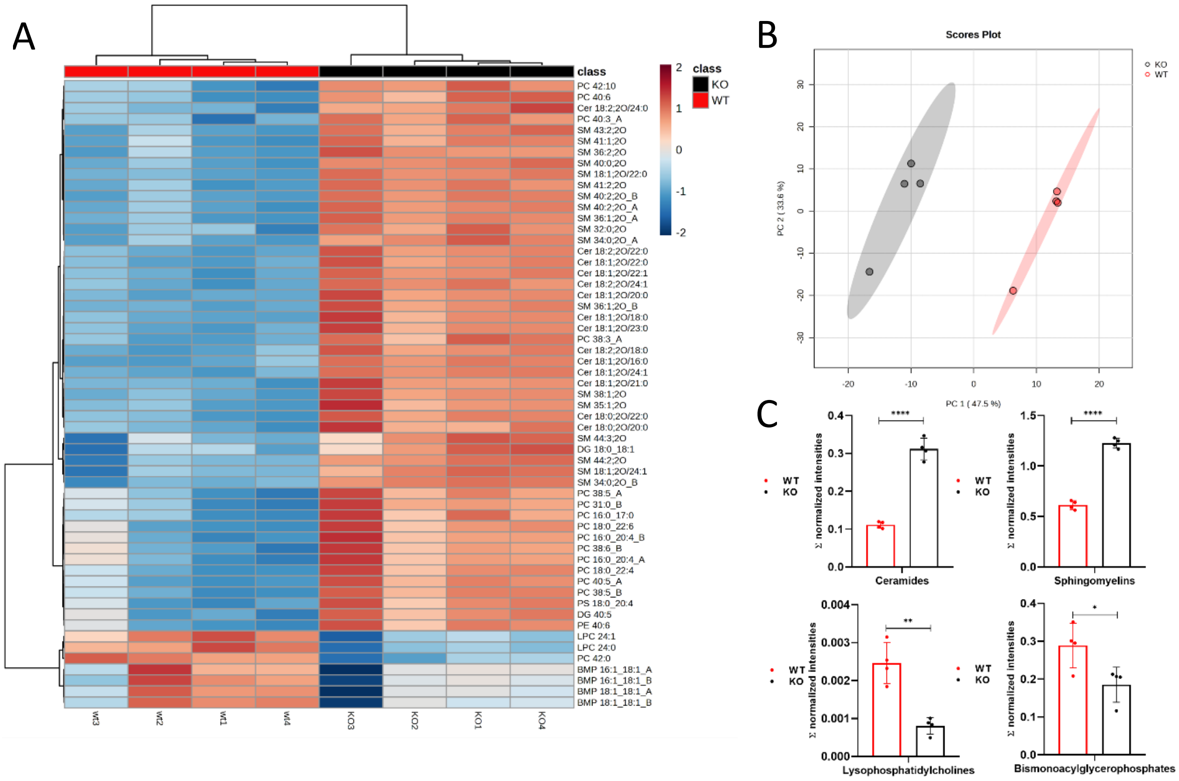

**Figure 3.14. *Gnpt*-deficiency leads to altered lipid composition of isolated lysosomes.** (**A**) Lipidomic heatmap showing normalized concentration of lipid species in parental and *Gnpt*-deficient MODE-K cells (n=4). (**B**) Principal component analysis score plots of lysosome lipids color-coded for wt and *Gnpt*-KO sample groups. (**C**) Significantly altered lipid subclasses quantified as sum of normalized intensities (mean±SD; unpaired student t-test; n=4 of each genotype).

Since abnormal lipid compositions of lysosome membranes impair the mobility, positioning and interorganelle contacts of lysosomes (Roney et al., 2021; Weesner et al., 2023), the complete lysosome lipidomes of wt and *Gnpt*-KO MODE-K cells were analyzed. MODE-K cells were incubated with magnetic dextran beads and lysosomes isolated as applied for proteome analysis (3.2.3). In collaboration with the group of Prof. Eduardo M. Sommella (University of Salerno, Italy) the lipidomes of lysosomes have been analyzed. After lipid extraction, untargeted lipidomic was performed by Reverse-phase Ultra-high performance liquid chromatography-Trapped Ion Mobility Spectrometry (RP-UHPLC-TIMS-MS) analyses (Merciai et al., 2022). In total, 342 lipid species (50 and 7 were significantly increased and reduced, respectively, in *Gnpt*-KO vs wt lysosomes) covering 14 lipid classes, were measured and annotated (Fig. 3.14 A; Suppl. Table S4). Principal component analysis (PCA) revealed genotype-dependent clustering of samples, indicating distinct changes in lipid composition of lysosomes from wt and *Gnpt*-KO cells (Fig. 3.14 B). Based on the entire dataset, ceramides (CER; e.g. Cer18:1;2O/24:1, Cer18:1;2O/16:0, Cer18:2;2O/22:0, Cer18:1;2O/22:1) containing un- or saturated long-chain fatty acids, and sphingomyelins (e.g. SM18:1;O2/22:0) comprised the significantly most increased subclasses in *Gnpt*-KO lysosomal fractions, whereas a significant reduction of lysophosphatidylcholins (LPC) and bis(monoacylglycero)phosphates (BMP) were found in the lysosomes of *Gnpt*-deficient cells (Fig. 3.14 C; Suppl. Table S4).

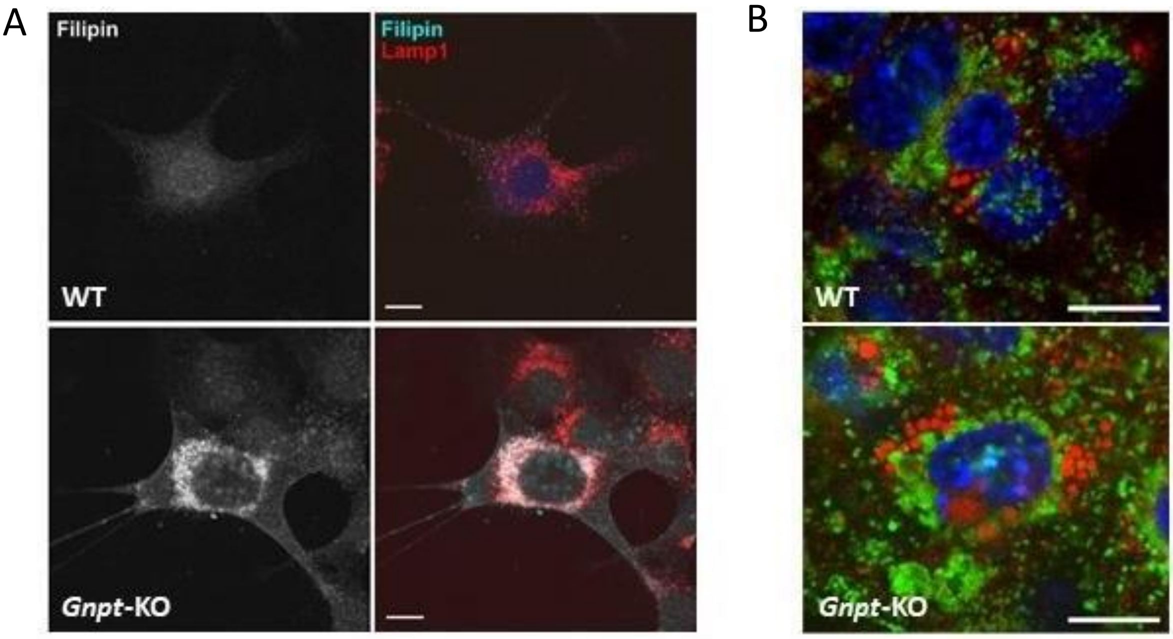

**Figure 3.15. Accumulation of cholesterol and lipid droplets in *Gnpt*-KO MODE-K cells.** (**A**) Non-esterified cholesterol (cyan) in lysosomes of *Gnpt*-KO cells co-stained with Lamp1 (red). Scale bars 10 µm. (**B**) Intracellular lipid droplets (red) in *Gnpt*-KO cells monolayer on filter co-stained with Lamp1 (green) and DAPI for nuclei (blue). Scale bars 10 µm.

In addition, immunofluorescence stainings for non-esterified cholesterol by usage of neutral polyene Filipin isolated from *Streptomyces filipinensis*, revealed its high accumulation in co-localization with Lamp1 in enlarged lysosomes of *Gnpt*-KO MODE-K cells, whereas no Filipin-positive lysosomes were observed in wt cells (Fig. 3.15 A). Similarly, an increased number of neutral lipid droplets was detectable in the immediate vicinity of perinuclear-localized lysosomes of *Gnpt*-deficient cells in comparison with wt cells (Fig. 3.15 B).

### 3.2.7 Autophagy in *Gnpt*-KO cells

As shown in *Gnpt*$^{ki}$ organoids (3.1.3.1) a strong increase of LC3-B immunoreactive bands could be confirmed in non-starved *Gnpt*-KO MODE-K cells by western blotting (Fig. 3. 16 A) and by immunofluorescence microscopy indicating weak cytoplasmic small LC3-positive puncta in wt and strong LC3-stained autophagosomal compartments in *Gnpt*-KO MODE-K cells (Fig. 3.16 B).

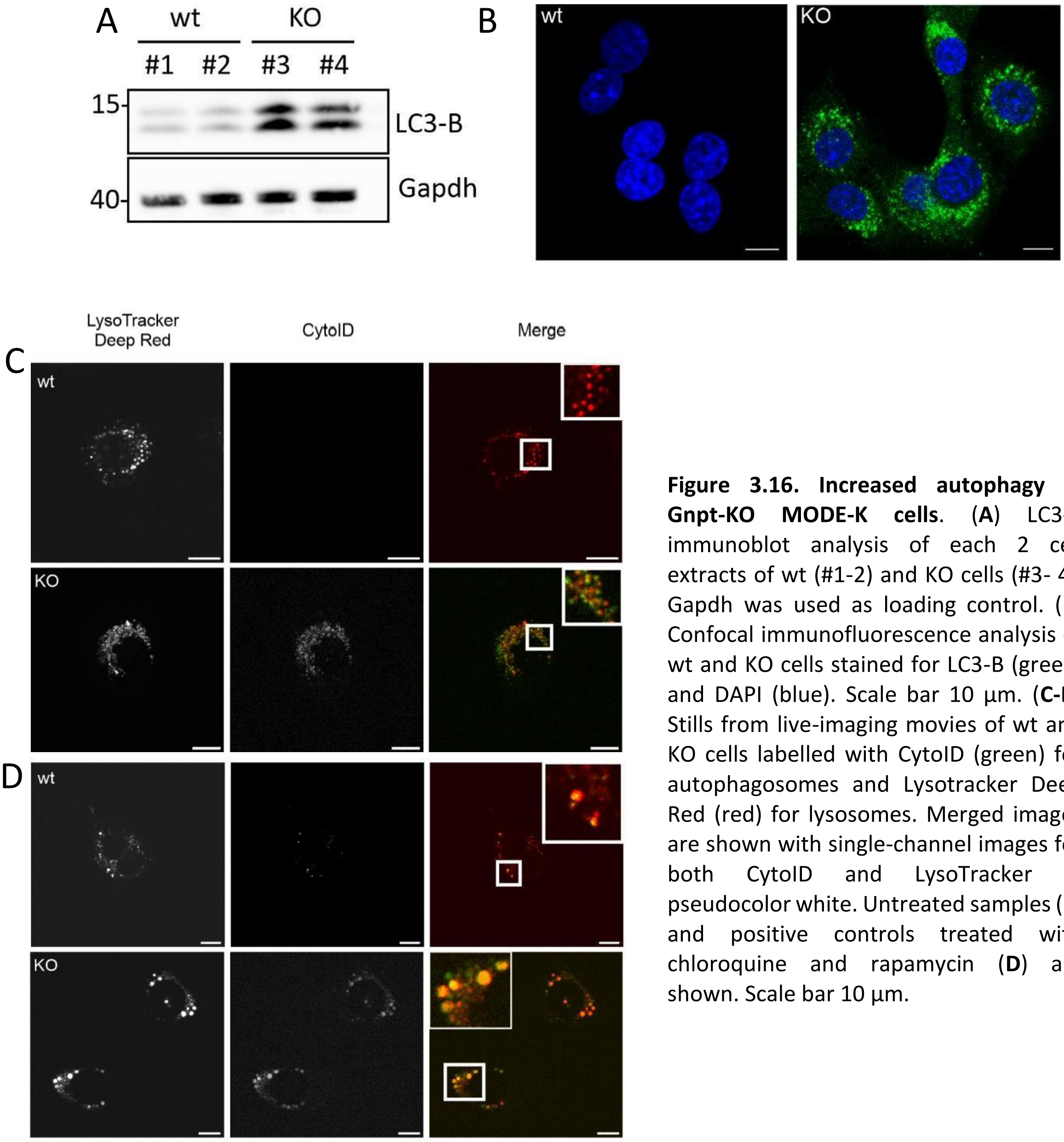

**Figure 3.16. Increased autophagy in Gnpt-KO MODE-K cells**. (**A**) LC3-B immunoblot analysis of each 2 cell extracts of wt (#1-2) and KO cells (#3- 4). Gapdh was used as loading control. (**B**) Confocal immunofluorescence analysis of wt and KO cells stained for LC3-B (green) and DAPI (blue). Scale bar 10 µm. (**C-D**) Stills from live-imaging movies of wt and KO cells labelled with CytoID (green) for autophagosomes and Lysotracker Deep Red (red) for lysosomes. Merged images are shown with single-channel images for both CytoID and LysoTracker in pseudocolor white. Untreated samples (**C**) and positive controls treated with chloroquine and rapamycin (**D**) are shown. Scale bar 10 µm.

In a third experimental approach, wt and KO cells were co-labelled with the CytoID®Green autophagy detection dye, able to exhibit bright fluorescence in precursor- and mature autophagosomes and autophagolysosomes (Chan et al., 2012), and LysoTracker™ Deep Red upon live-cell imaging (Fig. 3.16 C-D). In untreated wt cells, lysosomes were clearly detectable (red), but none of the green CytoID-positive autophagosomal structures (Fig. 3.16 C). In *Gnpt*-deficient cells lysosomes and strongly CytoID green stained organelles are both visible, better shown in the pseudocolor white staining. A higher magnification of the *Gnpt*-KO cell (Fig. 3.16 C inset) revealed separated endogenous autophagosomes and lysosomes, most likely due to a block in fusion of the organelles. As positive controls, wt and *Gnpt*-KO cells were treated with 500 nM rapamycin and 50 µM chloroquine (CQ) for 5 hrs as autophagy inducer and lysosomal activity inhibitor, respectively (Fig. 3.16 D). In cells of both genotypes lysosomes appeared swollen compared to the untreated condition. In particular, a strong merged signal in KO cells could be observed and it indicates the CytoID labelling of autophagolysosomes. Rapamycin treatment induces autophagy by inhibiting the mTORC1 complex (Laplante and Sabatini, 2012), thus leading to the production of autophagosomes, specifically stained by CytoID. CQ is a weak base belonging to the lysosmotropic drugs, undergoing lysosomal sequestration, lumenal pH elevation and subsequent inhibition of lysosomal degradative activity (Poole and Ohkluma, 1981). Interestingly, wt treated lysosomes appeared less swollen (Fig. 3.16 D) and the co-localization of CytoID-autophagosome and LysoTracker-lysosome stainings was reduced, indicating a decreased formation of autophagolysosomes.

## 3.3 *Yersinia enterocolitica* infections of MODE-K cells

### 3.3.1 Infection of MODE-K monolayer cells grown on filters

Intestinal epithelial MODE-K cells grown as monolayer on filters (Fig. 3.17 D) were used to assess the role of lysosomes and autophagosomes upon infection with RFP-labelled *Yersinia enterocolitica*. MODE-K cells were apically infected with *Y.enterocolitica* for 30 min at 37 °C. Fixing the cells directly after the 30 min infection, showed just few intracellular bacteria which did not co-localize with the lysosome marker Lamp1 (Fig. 3.17 A). To follow the intracellular fate of the few internalized bacteria, the *Yersinia*-containing medium was removed after 30 min and substituted by fresh medium including 100 µg/ml gentamicin to get rid of extracellular bacteria and incubated further for 3.5 hrs (chase). After fixation of the cells and co-staining with an antibody binding to the cytosolic tail of Lamp1, bacteria were enwrapped by Lamp1-positive structures in wild-type and *Gnpt*-KO MODE-K cells (Fig. 3.17 B).

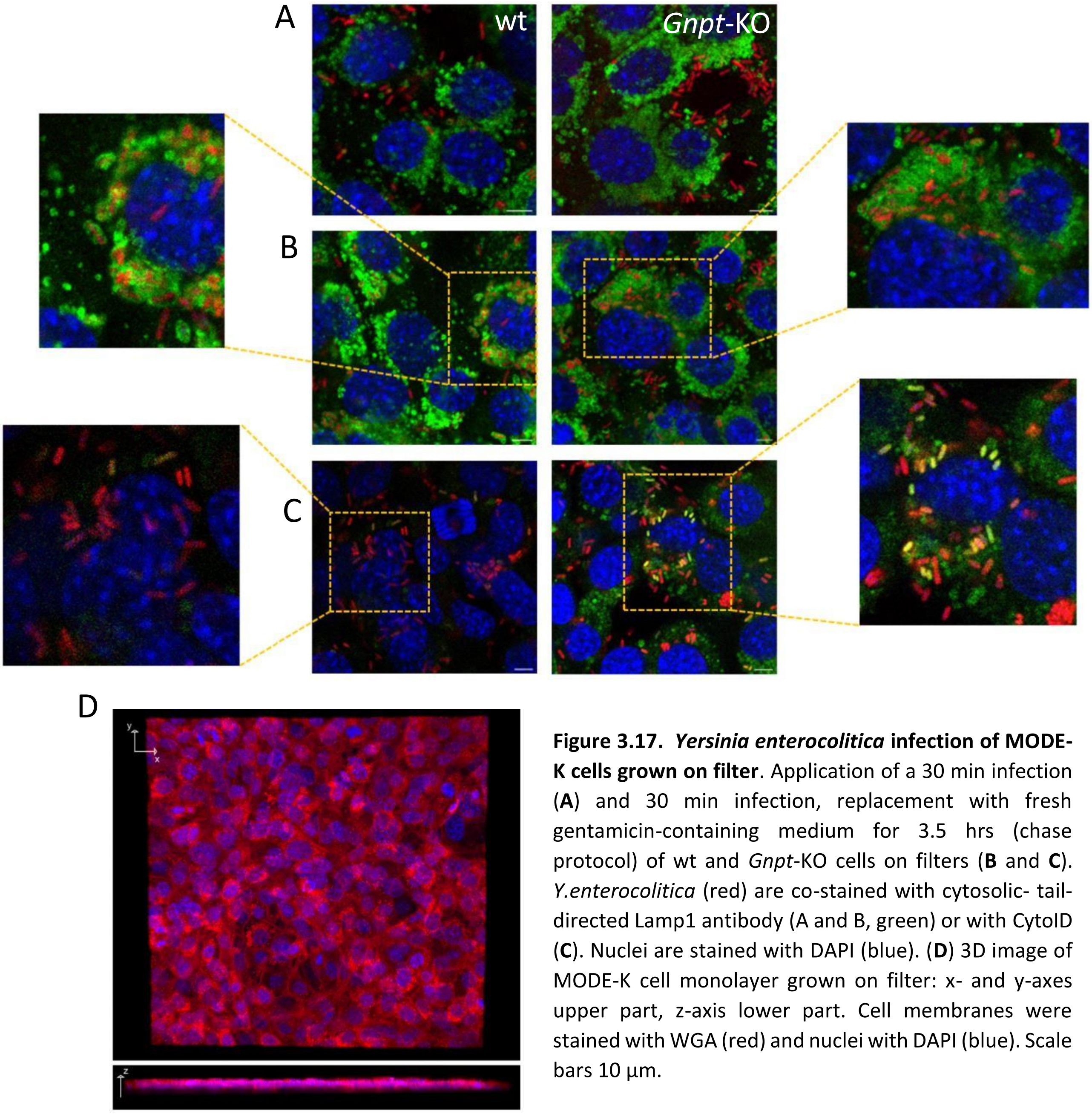

**Figure 3.17.** ***Yersinia enterocolitica* infection of MODE-K cells grown on filter**. Application of a 30 min infection (**A**) and 30 min infection, replacement with fresh gentamicin-containing medium for 3.5 hrs (chase protocol) of wt and *Gnpt*-KO cells on filters (**B** and **C**). *Y.enterocolitica* (red) are co-stained with cytosolic- tail-directed Lamp1 antibody (A and B, green) or with CytoID (**C**). Nuclei are stained with DAPI (blue). (**D**) 3D image of MODE-K cell monolayer grown on filter: x- and y-axes upper part, z-axis lower part. Cell membranes were stained with WGA (red) and nuclei with DAPI (blue). Scale bars 10 µm.

The *Yersinia*-containing lysosomes appeared to be increased in size (3 µm in average, n=60 from 8 different specimens). Generally, a weak Lamp1-staining has been observed in infected KO cells (Fig. 3.17 B). When infected MODE-K cells were co-stained under identical conditions with CytoID as autophagosomal marker, an increase in autophagic activity was detectable in KO cells as shown by the many green puncta visible in *Gnpt*-deficient cells, in comparison to wt cells. In addition, several bacteria were found in CytoID-positive compartments (yellow) in KO cells (Fig. 3.17 C), while in wt cells no bacteria could be found in autophagosomes. These data demonstrate that under these conditions, Yersinia accumulate in Lamp1-positive lysosomes in both genotypes of MODE-K cells and only in KO cells Yersinia were detected in CytoID-positive pre-existing autophagosomes.

### 3.3.2 Ultrastructural analysis of infected MODE-K cells

To investigate the localization of intracellular bacteria in intestinal MODE-K cells, wt and *Gnpt*-KO cells were pre-loaded with Bovine Serum Albumin (BSA)-coated gold nanoparticles (BSA-Au, OD=5), which are pinocytosed and delivered to lysosomes through the endocytic pathway (Pols et al., 2013), followed by infection with Yersinia-RFP (Fig. 3.18 A).

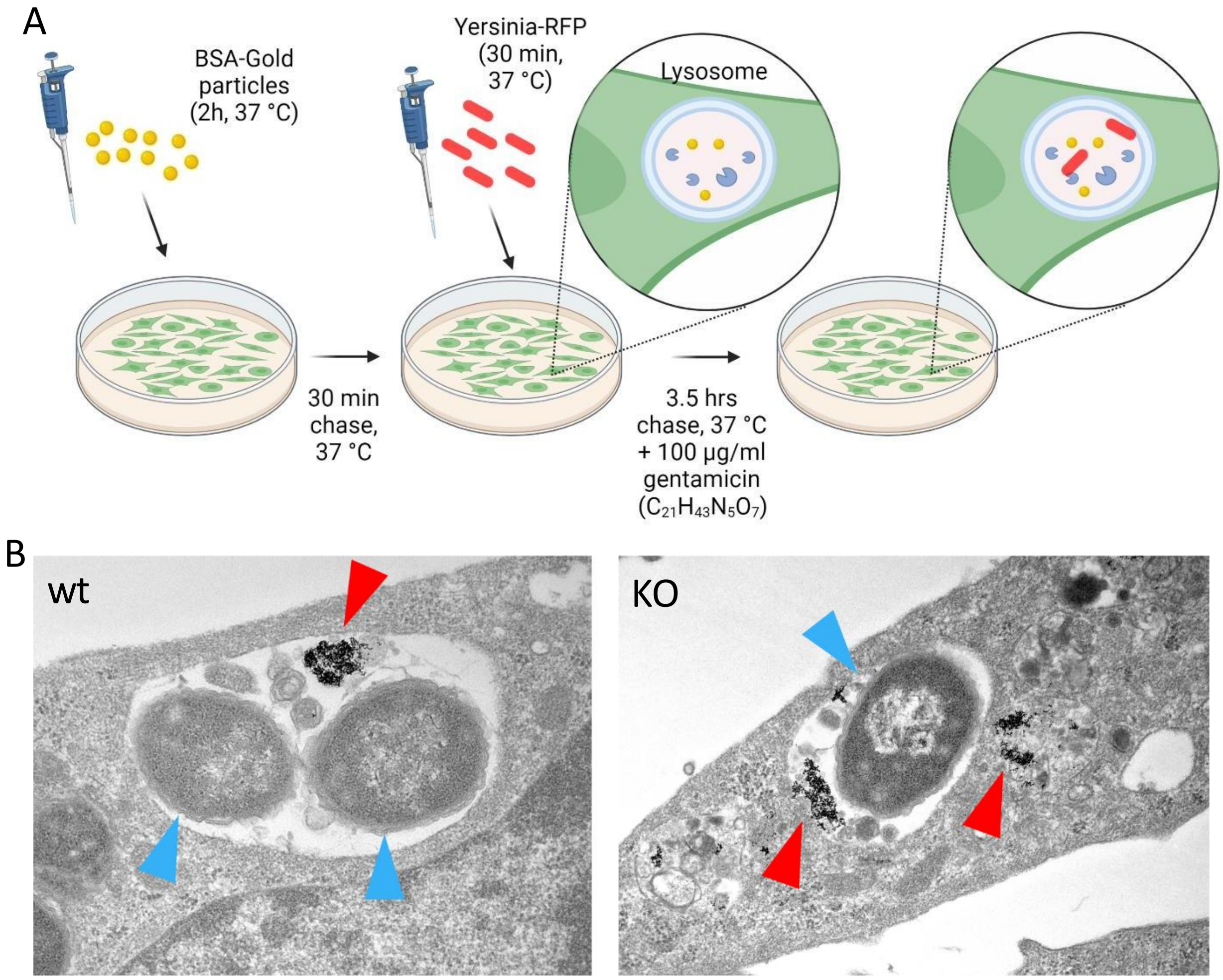

**Figure 3.18. Lysosome labeling of MODE-K cells with BSA-gold infected with *Y.enterocolitica* for ultrastructural analysis**. (**A**) Schematic representation of the experimental protocol to label lysosomes of wt and *Gnpt*-KO MODE-K cells with BSA-gold particles. Generated with BioRender. (**B**) Electron microscopy images of BSA-gold pre-loaded wt and KO cells infected with *Yersiniae* demonstrating their lysosomal localization. Red arrow heads indicate BSA-gold particles; cyan arrow heads point out bacteria.

Although it has been reported that an incubation period of 2 hrs with BSA-gold is sufficient to reach lysosomes (Galmes et al., 2015) the sequential time course of BSA-gold loading (2 hrs) followed by replacement of media, short infection period (30 min) and 3.5 hrs chase should guarantee the final destination of BSA-gold in lysosomes, accompanied by the BSA-gold depletion of other organelles within the endocytic pathway. The electron microscopy images revealed the presence of single *Yersiniae* (Fig. 3.18 B, cyan arrow heads) or sometimes two bacteria in single-membrane bound vacuolar compartments, which contain internalized BSA-gold particles (red arrow heads), and eventually other structured material of unknown identity. Of note, the membranes of the enclosed bacteria appeared slightly irregular or damaged. However, due to the bi-dimensional images, an interpretation that goes too far cannot be ruled out. Interestingly, in *Gnpt*-KO cells other smaller lysosomes, filled with storage material and clusters of BSA-gold particles but lacking bacteria can be observed (Fig. 3.18 A-B).

## 3.4 *Y.enterocolitica* infection of *Gnpt*$^{ki}$ intestinal organoids

To study the infection pathway of *Yersinia enterocolitica* in a multi-cellular system characterized by lysosomal dysfunctions, *Gnpt*$^{ki}$ intestinal organoids were infected with RFP-labelled bacteria and tested as proof of principle whether 3D structures could be infected from the basolateral side. Therefore, organoids embedded in matrigel were cultured and bacteria applied to the medium for 30 min at 37 °C; the medium was changed to remove floating bacteria and organoids imaged directly afterwards using a confocal microscope (Fig. 3.19 A-B).

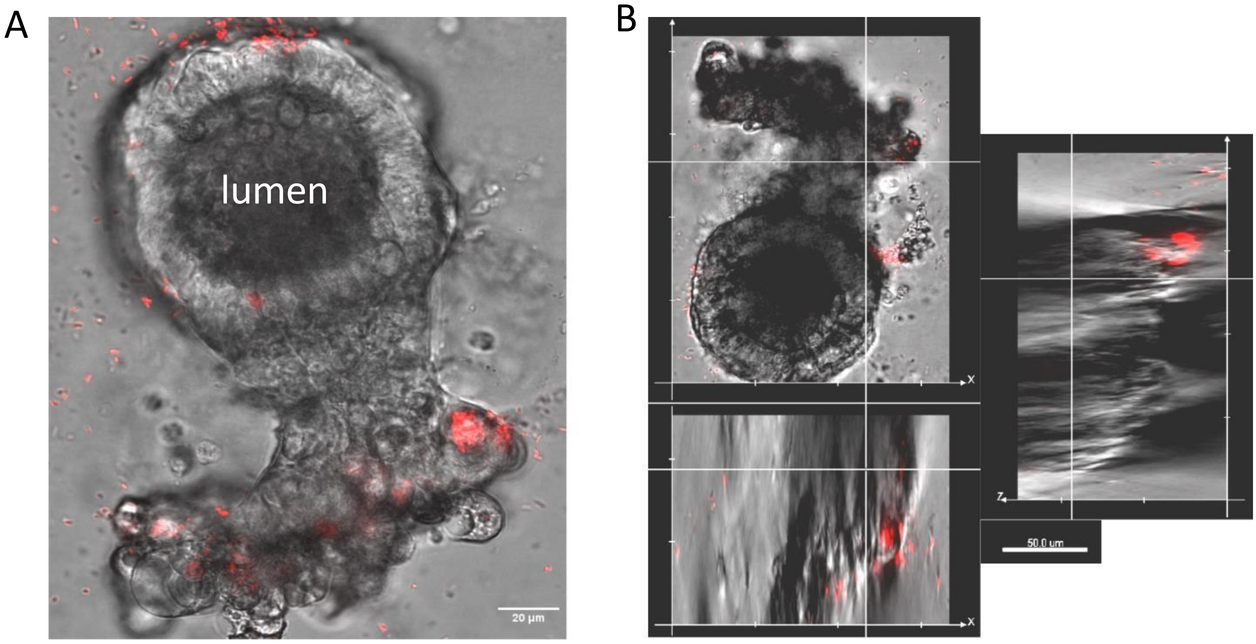

**Figure 3.19. Infection of basolateral-out matrigel-embedded murine intestinal organoids**. (**A**) Phase-contrast image of a *Gnpt*$^{ki}$ organoid overlapped with *Yersiniae* (in red). Scale bar 20 µm. (**B**) 3D projections of the organoid incubated with *Y.enterocolitica*. Scale bar 50 µm.

As shown in Fig. 3.19 A, *Yersiniae* were not internalized into organoid-forming cells under these conditions. The 3D projection (Fig. 3.19 B) showed that just few bacteria might get close to the organoid surface, as also shown in MODE-K cells monolayers when fixed after infection without any chase time (Fig. 3.14 A). Since foodborne *Yersinia* infections occur through the digestive tract and their interaction with the luminal part of the intestine, organoids with a reversed polarity (apical-out) might represent an alternative way to allow the access of pathogens to the apical epithelium by flipping the organoid inside out.

### 3.4.1 Apical-out intestinal organoid infection

Intestinal organoid polarity can be reversed in order to expose the apical side outward. Polarity reversion is triggered by the disruption of the interactions between ECM (or matrigel) and the basolateral β1 integrin receptors. This leads to a coordinated movement of the epithelium resulting in the reversion of the organoid polarity without altering the cellular composition, but recapitulating the functions (e.g. the maintenance of the barrier integrity) and properties of the intestinal epithelium (Co et al., 2019). The reversion process of an intestinal organoid over time is schematically represented in Fig. 3.20 A. In collaboration with the group of Prof. Denise Monack (Stanford University, CA) who established the organoid inside-out methodology, the time course of the reversion of both mouse and human intestinal organoids has been performed. As shown in Fig. 3.20 B, mouse and human intestinal organoids were reversed and it was demonstrated by staining with Zonula Occludens-1 (ZO-1) antibody for the intercellular tight junctions (green), phalloidin for actin (pseudocolor white) and DAPI for the nuclei (blue). It appeared that mouse organoids flipped faster, most likely due to the smaller size. Already after 2 hrs the reversion was fully accomplished as both ZO-1 and phalloidin stainings, typical marker of the apical side, are observed on the outside. On the contrary, the basolateral-out polarity of human organoids has not been changed after 2 hrs, showing a strong actin signal on the luminal side and the absence of ZO-1. After 6 hrs the human organoids revealed a mixed polarity, and the reversion was completed after 24 hrs. A further proof of the successful reversion is given by the release of dead cells from the apical surface into the medium (red arrow in Fig. 3.20 B, mouse 24h), since usually dead cells detach from the top of the apical microvilli into the lumen of the organoid, similarly to the release events of dead cells happening in the intestine, maturing from the bottom of the crypt and their release in the gut (Gehart and Clevers, 2019). To test the impact of organoid polarity on the infection rate, basolateral- and apical- out human organoids were infected with Gram-negative RFP-labelled *Salmonella enterica-serovar thyphimurium*. The images presented in Fig. 3.21 represent an infection experiment performed with high amounts of bacteria (MOI=600) for a short incubation of 30 min at 37 °C. In human organoids with the basolateral-out orientation (Fig. 3.21 A), bacteria could barely interact with the epithelial surface of the organoid and none of them entered the cells.

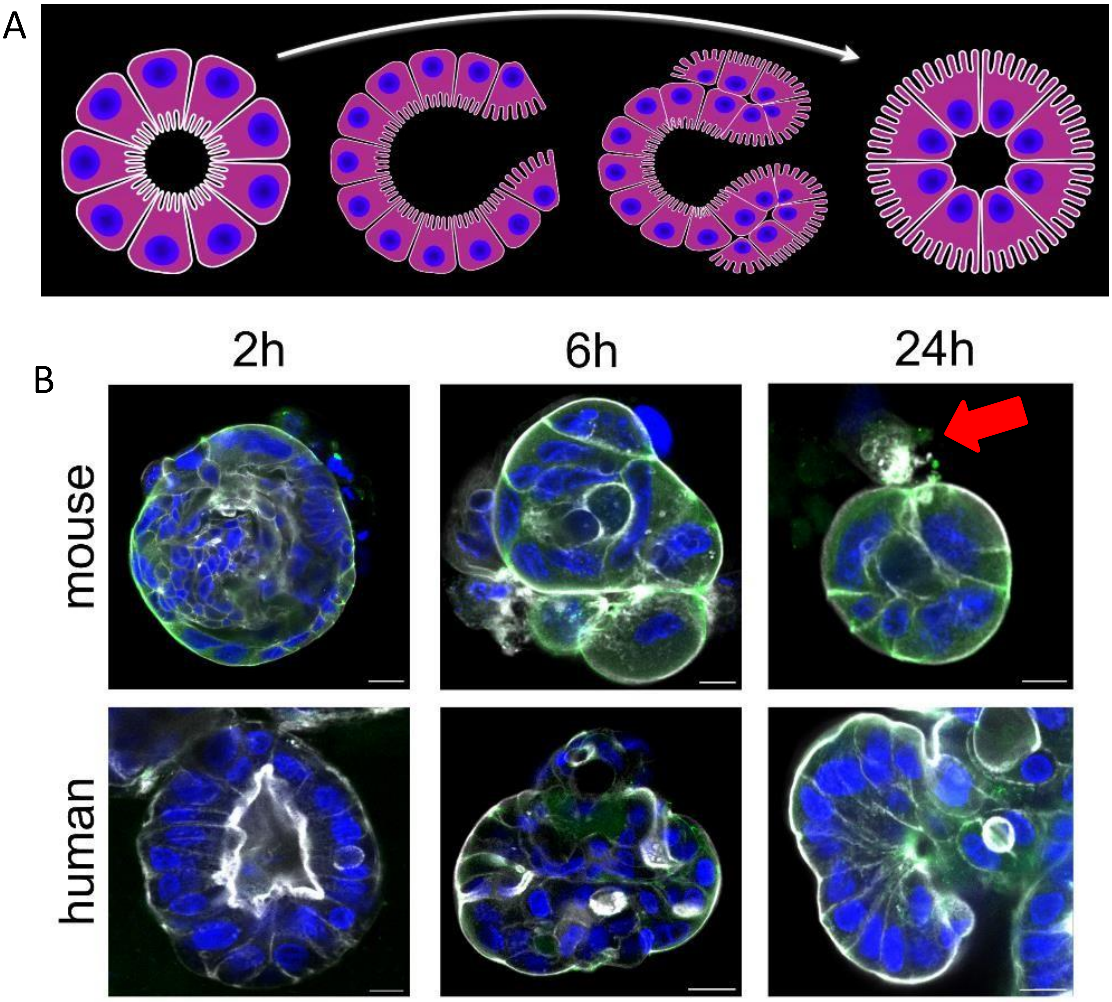

**Figure 3.20. Reversion of intestinal organoid polarity**. (**A**) Schematic representation of polarity reversion of an intestinal organoid (Co et al., 2019). (**B**) Comparative timecourses of polarity reversion velocity between mouse (upper) and human (lower) intestinal organoids stained with ZO-1 (green), phalloidin (pseudocolor white) and DAPI (blue). Scale bar 10 µm.

When the apical side faced outward (Fig. 3.21 B) multiple bacteria interacted with the surface and entered the cells. Since the short infection time did not allow bacterial replication, the intracellular bacteria represented the number of pathogens internalized in 30 min. Under conditions of organoids with mixed polarity (see Fig. 3.20 B) only flipped cells showed internalized bacteria, whereas apical-in cells were not infected (Fig. 3.21 C-D). These preliminary experiments demonstrated the impact of polarity orientation for host-pathogen interactions and represented an advanced tool to investigate kinetics, intra-cellular survival and molecular players of the pathogen internalization machinery. The established flipping approach must be adapted for infection experiments of murine intestinal organoids prepared from wild-type and *Gnpt*$^{ki}$ mice with *Yersinia enterocolitica.*

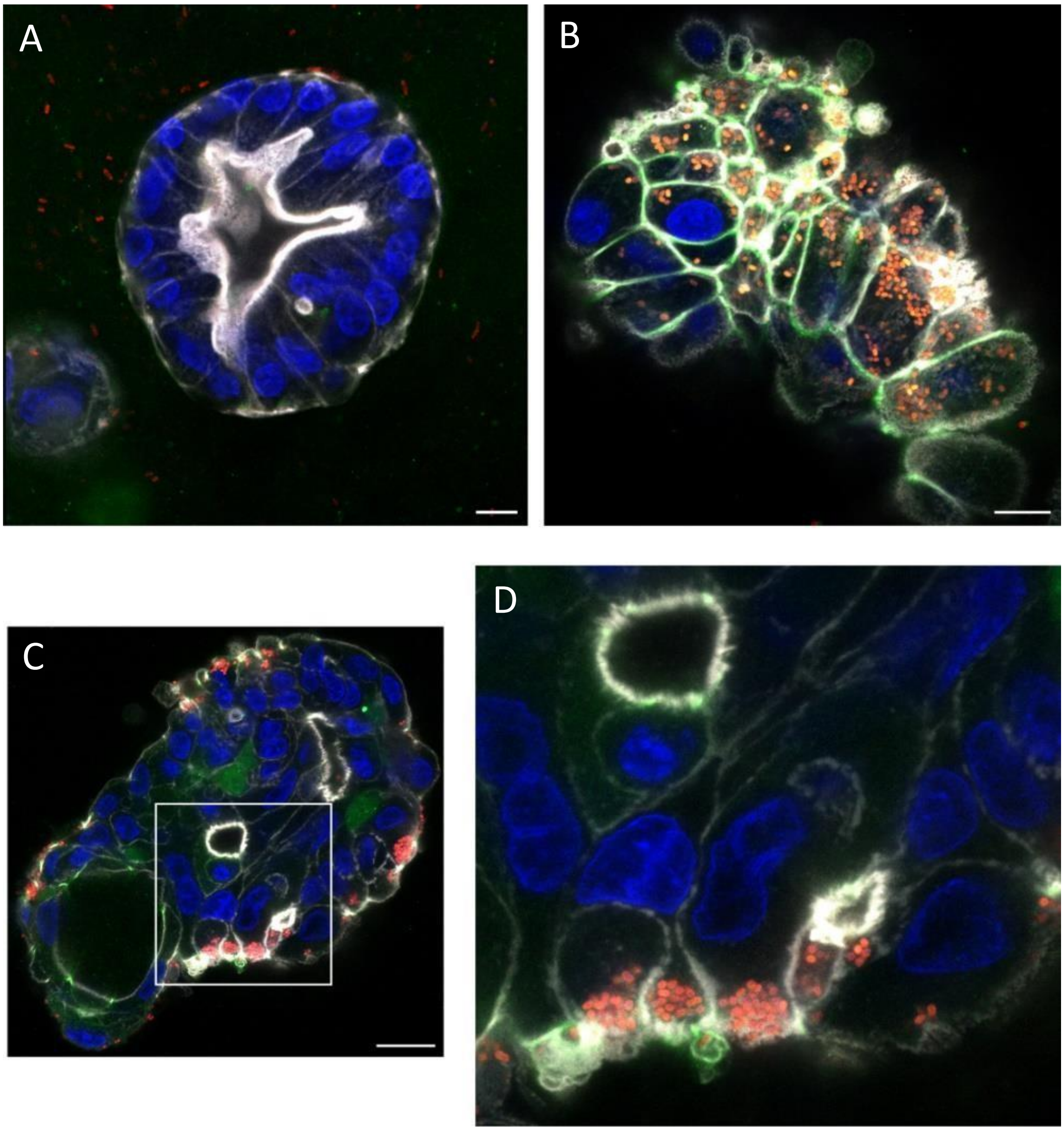

**Figure 3.21. Infection of human basolateral-out and apical-out intestinal organoids with RFP-labelled *Salmonella thyphimurium*.** (**A**) Basolateral-out organoids infected with *S.Thyphimurium* (red), characterized by strong apical phalloidin signal (pseudocolor white), very weak ZO-1 signal (green) and DAPI (blue). (**B**) Apical-out organoids infected with *S.Thyphimurium* (red), stained with phalloidin (pseudocolor white), ZO-1 (green) and DAPI (blue). (**C**) Example of a mixed polarity organoid: local polarity determines whether infection takes place. (**D**) Inset of Fig. 3.18 C, including an apical-out polarity region (plenty of red bacteria) and a basolateral-out one (inner, phalloidin-positive but undecorated with bacteria). Organoids were stained with phalloidin (pseudocolor white), ZO-1 (green), DAPI (blue). Scale bar 10 µm.

# 4. Discussion

Lysosomes represent the center for metabolic regulation of the cell, acting in the degradation of macromolecules, extracellular substrates, and bacteria delivered to lysosomes through the biosynthetic, endocytic, phagocytic, or autophagic pathways. The degradative functions are catalyzed and mediated by ~70 hydrolytic luminal enzymes and accessory proteins. The degradation products egress the lysosomes and are recycled creating new building blocks and providing new sources of energy (Eriksson and Öllinger, 2024). The lysosomal homeostasis requires a continuous replacement of lysosomal hydrolases which depends on a common posttranslational modification: mannose 6-phosphate (M6P) tags on their oligosaccharides which allow their efficient transport to lysosomes (Braulke et al., 2024). The loss of the GlcNAc-1-phosphotransferase (GNPT), the key enzyme in the formation of M6P residues, resulted in complete dysfunctional lysosomes due to the missorting of almost all lysosomal enzymes. Therefore *Gnpt*-KO cells or intestinal organoids prepared from *Gnpt$^{ki}$* mice provide suitable single or multi-cellular systems, respectively, to analyze molecular mechanisms on the role of lysosomes for *Y.enterocolitica* infections.

## 4.1 *Gnpt$^{ki}$* intestinal organoids

In contrast to previous studies reporting on phenotypes and biochemical hallmarks of different animal models with defective Gnpt activity (Bosshard et al., 1996; Gelfman et al., 2007; Kollmann et al., 2012; Flanagan-Steet et al., 2009), tissue-specific alterations in these animals (Kollmann et al., 2012; Kollmann et al., 2013; Schweizer et al., 2013; Sachs et al., 2020; Flanagan-Steet et al., 2016; Lu et al., 2020) or cultured single cell types prepared from affected mice and zebrafishes (Boonen et al., 2011; Kollmann et al., 2013; Otomo et al., 2015; Markmann et al., 2017), the first polarized and multi-cellular organoid model of the small intestine from *Gnpt$^{ki}$* mice has been established and characterized in the present thesis. Several of the typical biochemical and cell biological properties of cellular and tissutal Gnpt deficiency have been confirmed, such as enlarged lysosomes, accumulation of heterogeneous storage material, missorting and intracellular loss of lysosomal enzymes, as well as impaired autophagy. However, due to the progress in new methods and cutting-edge technologies several novel data were collected which provide deeper insights into adaptive processes and molecular alterations unknown so far.

### 4.1.1 Loss of mobility of enlarged *Gnpt*$^{ki}$ lysosomes

Surprisingly live-cell imaging of wt and *Gnpt*$^{ki}$ organoids labelled with LysoTracker Deep Red revealed that, in contrast to wt organoids in which smaller lysosomes are distributed throughout the cells, the enlarged lysosomes in *Gnpt*$^{ki}$ organoids are clustered and localized beneath the apical surface (3.1.2; Fig. 3.3). Apical positioning of lysosomes has not been described previously neither in other polarized cells, in dependence of the lysosomal dysfunction, nor in multi-cellular organoid systems. Furthermore, these *Gnpt*$^{ki}$ lysosomes showed no mobility whereas the lysosomes in cells of wt organoids moved between the apical and basolateral membranes in all directions. Both differences in positioning and mobility of lysosomes in wt and *Gnpt*$^{ki}$ organoids were confirmed at a higher resolution by Lattice lightsheet (LLS) microscopy (Figure 3.4).

To examine whether changes in the protein composition of lysosomal membranes, as well as proteins associated with the cytoplasmic surface of lysosomes, are responsible for the differences in lysosome mobility and positioning in wt and *Gnpt*$^{ki}$ organoids, targeted lysosome mass spectroscopy has been performed in whole organoid lysates. This data-independent acquisition (DIA) approach offers increased sensitivity and reproducibility for low-abundant peptides in complex samples (organoid lysates) without prior enrichment. Thus, the Winter lab generated a list comprising 374 proteins assigned to the lysosomal compartment-based gene ontology (GO) and Uniprot categories (Mosen et al., 2021). Whereas the low abundance of 28 soluble lysosomal enzymes in the lysates of *Gnpt*$^{ki}$ organoids could be confirmed, the amounts of detectable proteins involved in lysosomal mobility, such as the small GTPase Rab7, the Arf-like (Arl) protein Arl8 or the Borcs5 subunit of the octameric BORC complex (Pu et al., 2015), were not significantly changed (3.1.3; Fig. 3.5; Suppl. Table S1). The proteome data represent the mean of several cell types in different ratios to each other and unfortunately provided no molecular hints on proteins that might be responsible for the observed alterations in lysosomal positioning and/or mobility in *Gnpt*$^{ki}$ organoids.

### 4.1.2 Directional missorting of lysosomal enzymes

The intracellular loss of lysosomal hydrolases shown in Fig. 3.5 A confirms numerous reports on the loss of Gnpt activity demonstrating the hypersecretion of the lysosomal enzymes lacking M6P residues (Markmann et al., 2015; Richards et al., 2022; Markmann et al., 2017; Badenetti et al., 2024; Qian et al., 2010; Brauer, Chen et al., 2024). In a polarized multi-cellular system such as intestinal *Gnpt*$^{ki}$ organoids, a three-dimensional mini-intestine is formed with distinct apical and basolateral plasma membrane domains. The apical membrane faces the intestinal lumen and consists of an inner layer rich in phosphatidylinositol-4,5-bisphosphate (PI(4,5)P2), and of the outer layer containing glycosphingolipids and cholesterol. The basolateral plasma membrane of intestinal epithelial cells is rich in PIP3 and important for interactions between adjacent cells and the basement membrane (Schneeberger et al., 2018). In principle, the hypersecretion of lysosomal enzymes from *Gnpt$^{ki}$* organoids should be possible towards apical and/or basolateral membranes. However, the western blot analyses of organoid extracts shown in Fig. 3.5 B might suggest that cathepsin Z and C are secreted to the basolateral side, because the immunoreactive proteins were lost in *Gnpt$^{ki}$* organoids. On the other hand, both the signal intensity of immunoreactive granulin and cathepsin B are similar in wt and *Gnpt$^{ki}$* organoid extracts, which might suggest apical secretion towards the organoid lumen. The separate western blot analyses of organoid cell extracts and collected basolateral media revealed a clear basolateral secretion of cathepsin B and cathepsin D precursor forms (Fig. 3.6 A). However, only targeted or secretome analyses by MS of basolateral media will define the number and function of secreted lysosomal enzymes from polarized *Gnpt$^{ki}$* organoids. At present there is no information on the molecular mechanisms on how newly synthesized soluble proteins are sorted and transported to the apical or the basolateral site.

## 4.2 Intestinal *Gnpt*-KO MODE-K cells

To overcome the difficulties and disadvantages of murine intestinal organoids, we chose to use a cell line, the murine intestinal epithelial cell line MODE-K, in which the Gnpt gene was targeted using the CRISPR/Cas9 technology (3.2). The gene disruption and the biochemical and cell biological consequences have been validated by sequencing of the *Gnpt* gene, missorting of lysosomal enzymes and ultrastructural analysis of storage material (3.2.1; Fig. 3.7). However, by analyzing MODE-K cells the increased number, size and positioning of lysosomes could be quantified for the first time in *Gnpt*-KO in comparison to wt cells (3.2.2). The total cellular immunofluorescence of Lamp1-positive lysosomes was increased by 23% in *Gnpt*-KO cells, which summarized both enlarged sizes caused by storage material and the number of lysosomes which cannot be differentiated due to the high degree of lysosome clusters (Fig. 3.8 C). In addition, by analyzing the content of Lamp1-fluorescence as a function of a 3 µm-outward distance from the nucleus, the preferential perinuclear or peripheral localization of lysosomes could be determined. The content of perinuclearly located lysosomes of *Gnpt*-KO cells is almost doubled in comparison to wt cells (Fig. 3.8 D). About 60% of all Lamp1-positive lysosomes were found in peripheral areas outside the 3 µm nuclear distance (Fig. 3.8 E). A preferential perinuclear localization of storage-containing lysosomes has been reported in several cell models of lysosomal storage disorders (e.g. NPC1, Zhao and Ridgway, 2017; Mucopolysaccharidosis type IIIA, Capuozzo et al., 2022; for reviews, Scerra et al., 2022; Zhao et al., 2020) or by nutrient deprivation (Li et al., 2016).

### 4.2.1 Lysosomal pH, lysosomal proteome and lipidome analyses

Since the subcellular localization and functions of lysosomes have been described to correlate with their luminal pH (Johnson et al., 2016), we have measured the luminal pH of lysosomes of *Gnpt*-KO MODE-K cells with two experimentally independent approaches. First, the superecliptic pHluorin (SEP) fused to the luminal domain of LAMP1-RFP (Farías et al., 2017) was expressed in wt and *Gnpt*-KO MODE-K cells, and the analyses of the fluorescence images revealed that in cells of both genotypes the lysosomes are acidic (3.2.2; Fig. 3.10 A-B). This has been supported by ratiometric pH measurements based on the pH-sensitive Oregon green 488-dextran dye (Steinberg et al., 2010), which clearly determined the lumenal pH to 4.4 ± 0.1 in both the cell lines (3.2.2; Fig. 3.10 D). These data indicate that the lysosomal dysfunctions in *Gnpt*-KO cells are caused by the loss of multiple lysosomal enzymes rather than changes in the luminal pH.

The informative value of the targeted lysosomal proteome analysis of organoids by MS (3.1.3 and 4.1.1) is limited due to the low amounts and the multicellular composition of organoids differing in their relative abundance (enterocytes represent 80% of all epithelial cells; Boonekamp et al., 2020). Therefore, mouse intestinal epithelial MODE-K cell line isolated from crypts of the duodenum, retrovirally immortalized and selected with neomycin (Vidal et al. 1993), represents the major cell type of the murine organoids used (3.1), characterized by a fast proliferation rate that allows the sensitive proteome analysis of even low abundant proteins in highly enriched lysosomal fractions. The method of superparamagnetic iron oxide nanoparticles (SPIONs) loading of cells to isolate highly enriched lysosomal fractions was established in the lab many years ago (Markmann et al., 2015; Di Lorenzo et al., 2018; Schmidtke et al., 2019; Richards et al., 2022). We directly compared the lysosomal proteomes of MEF (Markmann et al., 2015) and MODE-K cells, in which we found in total 51 and 49 soluble lysosomal hydrolases, respectively, in lysosome preparations. 43 were overlapping in both cell lines. The abundance of four enzymes, Smpd1, Fuca1, Neu1, and Man2b2 is very low (2-15 % of wt lysosomes), so their reduction appears to be the main driver of lysosomal dysfunction, possibly together with 11 and 12 other hydrolases we found to be low abundant in both MEF and MODE-K cells. It is of interest that in MEFs eight of the very low abundant hydrolases are involved in lipid degradation (Markmann et al., 2015), whereas in MODE-K cells nine low abundant lysosomal enzymes participate in glycostructure degradation. The majority of luminal enzymes, however, in lysosomes of MEF (30) and MODE-K cells (21) vary in their abundance between 15 and 50% of control wt lysosomes. It is believed that these enzymes are targeted to lysosomes via M6P-independent cargo receptor routes (Braulke et al., 2024). Obviously, there are no alternate M6P-independent receptors for the low abundant hydrolases in MEF and MODE-K cells which strictly require M6P residues for their targeting to lysosomes.

The lysosomal membrane proteome of MODE-K cells revealed a 5.7- and 2.9-fold increase of the volume-regulated anion channel (VRAC) subunits A (Lrrc8a) and E (Lrrc8e), respectively (Suppl. Table S2 E). Lrrc8a as an essential VRAC component and the Lrrc8e subunit form a functional channel that is required for the osmoregulation of lysosomes to maintain water homeostasis, organelle volume, and membrane integrity under osmotic challenges (Li et al., 2020). It needs to be validated whether the accumulation of storage material in *Gnpt*-KO MODE-K cells leads to the Lrrc8-mediated enlargement of lysosomes and how its expression is regulated.

In general, the autophagy-lysosomal pathway by which proteins and organelles are delivered to the lysosomes for degradation is impaired in cells with dysfunctional lysosomes and has been implicated in many lysosomal storage diseases (Seranova et al., 2017; Ren and Wang, 2020). Examinations of fibroblasts from ML II patients revealed the accumulations of double-membraned autophagosomes, increased level of LC3-II and fragmented mitochondria (Otomo et al., 2009; Otomo et al., 2011).

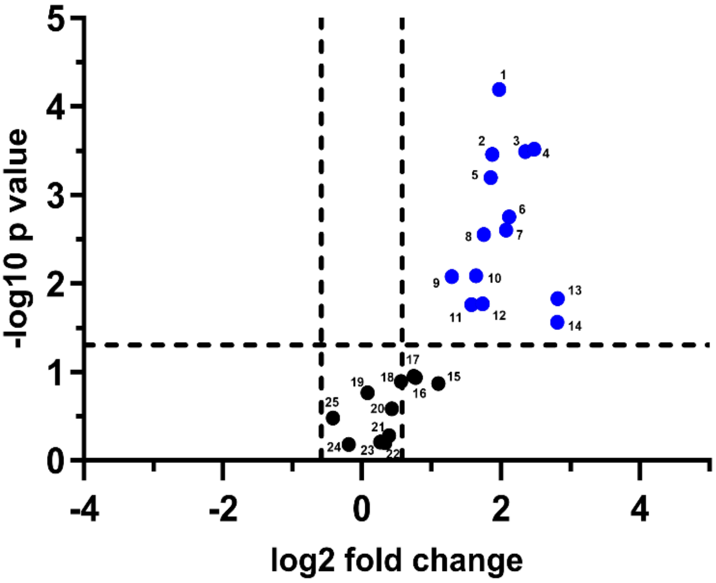

**Figure 4.1. Autophagy related proteins** associated with enriched lysosomal fractions of *Gnpt*-KO MODE-K cells. 1. Lgals8; 2. Map1lc3b; 3. Sqstm1; 4.Tax1bp1; 5.Wdr45 (Wipi4); 6.Atg9a; 7.Nbr1; 8.Atg3; 9.Atg16l1; 10.Ulk1; 11.Atg13; 12.Atg101; 13.Optn; 14.Tmem59; 15.Lamtor3; 16. Lgals3; 17.Gnai3; 18.Hspa8; 19.Atg2b; 20.Dram2; 21.Atg5; 22.Wipi2; 23.Vps4a; 24.Rraga; 25.Rptor. Significantly and differentially expressed proteins are listed in the Suppl. Table S3.

In addition, several marker proteins of activated autophagy, LC3-II, p62 and increased level ubiquitin-modified proteins have been reported in the brain of *Gnpt*$^{ki}$ mice (Kollmann et al., 2012).

# Discussion

In *Gnpt*-KO MODE-K cells both LC3-B western blots, LC3-immunofluorescence microscopy and CytoID/LysoTracker Deep Red stainings showed the basal activation of autophagy in *Gnpt*-deficient cells (3.2.7; Figure 3.16). The proteome analysis of highly enriched lysosomes supported the cell biological data demonstrating 14 significantly increased autophagy-related proteins associated with the lysosomes of *Gnpt*-deficient cells (Figure 4.1; Suppl. Table S3).

Further evaluation of these 14 enriched autophagy proteins on *Gnpt*-KO lysosomes revealed that half of them is ubiquitin (Ub)-binding autophagic receptors and all proteins are involved in i) the initiation of the ULK complex assembly, ii) the membrane elongation and lipidation of Atg8 proteins, and iii) the recruitment of the PI3KC3 complex (Yamamoto et al., 2023). Their presence in lysosomes suggests that the increased amounts of autophagy-related proteins detected are caused by reduced degradation of the components in dysfunctional lysosomes. However, immunofluorescence microscopy-based observations additionally suggest reduced fusion of autophagosomes with lysosomes, possibly as a consequence of altered protein and/or lipid composition of lysosomal membranes.

Very recently, alterations in the level of autophagy proteins have been reported in various cell models of lysosomal storage diseases (LSD) to correlate with distinct lipid species (Kraus et al., 2025). The authors used 3x HA-tagged TMEM192 to immunprecipitate lysosomes and generated proteo-lipidomic landscapes for 33 LSD mutant cell lines. For example, the targeting of the lysosomal membrane protein Npc1 and the luminal accessory protein Npc2, both required for the efflux of cholesterol, correlated significantly with distinct lipids of specific lipid classes (lipid fingerprint) and resulted in a complex Ub-binding autophagy receptor network with phosphatidylcholine (PC), lyso-PCs (LPC), alkenyl-diacylglycerols (DGs), and GD3- and GM2-gangliosides. These findings are highly relevant for the proteomic and lipidomic data from magnetite-lysosome preparations from *Gnpt*-KO MODE K cells, because Npc2 belongs to the luminal proteins that depend strongly on M6P residues and is strongly reduced (Fig. 3.9 A, Suppl. Table S2 A) as reported previously (Markmann et al., 2015). The abundance of the Npc1 cholesterol exporter is not changed in comparison with wt lysosomes. Thus, the absence of Npc2 in *Gnpt*-deficient MODE-K lysosomes is sufficient to increase lysosomal cholesterol shown by Filipin-staining (Fig. 3.15 A), with a strong activation of autophagy and several autophagy receptors (3.2.7, Fig. 3.16, Fig. 4.1, Suppl. Table S3), and mostly elevated levels of PC, LPC, and Cer species. Since in *Gnpt*-KO lysosomes in addition to Npc2 other lipid-degrading enzymes (Abhd6, Hexb, Arsa, Neu1, Smpd1, Psap, Asah1, Pla2g15) are strongly reduced (Suppl. Table S2 A), it is likely that the lipidome also differs from the NPC2-defective HeLa TMEM192-3xHA cells (Kraus et al., 2025). We aim to correlate the altered autophagy receptors and core proteins with lipid clusters identified in the *Gnpt*-KO MODE-K cells, and test how the addback of recombinant M6P-containing lipases, Npc2 or activator proteins (Psap) changes the lipid and/or proteome landscape, the kinetics of intracellular protein transport, and/or the mobility of lysosomes to determine the crucial drivers of these processes.

## 4.3 *Yersinia enterocolitica* enter the host lysosome-autophagy pathway

We used intestinal organoids and the murine intestinal epithelial MODE-K cell line to investigate the first steps in the course of *Yersinia enterocolitica* infection, the internalization into cells of the intestinal tract. Intracellular bacterial pathogens e.g. *Yersinia enterocolitica*, internalize mammalian host cells and form bacteria (*Yersinia*)-containing vacuoles (BCV; YCV). In phagocytic and epithelial cells such as macrophages and HeLa cells, respectively, pathogenic *Yersiniae* are able to activate the autophagy (xenophagy) pathway indicated by the LC3-conversion to the lipidated LC3-II form. During the next steps YCV will fuse with elongated phagophores (see 1.3) to form double-membrane autophagosomes (Lemarignier and Pizarro-Cerdá, 2020) which subsequently can fuse with lysosomes to acidic autolysosomes for degradation of cargo/pathogens (Yamamoto et al., 2023). However, it has been reported that in epithelial HeLa cells subpopulations of *Y.entercolitica* follow the degradative lysosomal pathway whereas the other half of *Yersinia* survive and replicate in non-acidic double-membrane autophagosomes unable to fuse with lysosomes (Valencia Lopez et al., 2019).

Surprisingly, in both wild-type and *Gnpt*-KO MODE-K cells grown on transwell filters in a polarized manner, *Y.enterocolitica* are detected after a standard 4 hrs pulse-chase protocol in Lamp1-positive structures (Fig. 3.17). When uninfected MODE-K cells were labeled with CytoID, an autophagosomal marker, only *Gnpt*-KO cells showed a high number of activated autophagosomes, in which bacteria are detectable 4 hrs post-infection. This means that in *Gnpt*-KO MODE-K cells the autophagy pathway is activated in an mTORC1 and starvation-independent (non-canonical) manner, which is confirmed by the increase of autophagy receptor and core proteins demonstrated by MS (Fig. 4.1; Suppl. Table S3). Most likely, the dysfunctional lysosomes in *Gnpt*-KO cells are not able to fuse with pre-existing autophagosomes. At present it is unclear why *Y.enterocolitica* do not activate autophagy in MODE-K cells as reported for HeLa cells (Valencia Lopez et al., 2019). Perhaps the higher MOI for the infection or the different cell type might be responsible for the activation of autophagy in HeLa cells.

# Discussion

The ultrastructural analysis of infected MODE-K cells revealed that the *Yersinia*-containing vacuoles consist of a single membrane (Fig. 3.18). Similar findings have been reported by Ligeon et al., 2014, upon infection of HeLa cells with *Yersinia pseudotuberculosis*. High amounts of the SNARE protein VAMP3 which controls the fusion between multivesicular bodies and autophagosomes and mediates the fusion with ATG9-containing vesicles, correlate with the appearance of single membrane YCV. By analyzing the proteome data of lysosome-enriched fractions from wt and *Gnpt*-KO MODE-K no VAMP3 could be detected. The increased amounts of VAMP2 in the *Gnpt*-KO proteome is most likely not relevant for the single membrane YCV morphology in the MODE-K cells of both genotypes. The BSA-gold co-localization in the majority of YCV supports the high prevalence of the lysosomal entry pathway of *Y.enterocolitica* in MODE-K cells.

In further experiments we have to examine 1) the kinetics of MODE-K cell infection with *Y.enterocolitica* between 1 and 24 hrs, 2) the simultaneous 3-colour stainings of Lamp1-positive lysosomes and CytoID-positive autophagosomes upon *Yersinia* infection, 3) the intracellular bacterial replication rate, 4) the pH in YCV, 5) the lysosomal (BSA-gold-positive) proteome upon *Y.enterocolitica* infection.

The most physiological in vitro model for the analyses of the molecular mechanisms of infection with *Y.enterocolitica* are intestinal organoids. Since the basolateral-out morphology of organoids prevents the direct infection with *Yersinia*, the successful establishment of the apical-out technology in the lab will make performing the infection experiments in a multi-cellular system possible. In particular, the role of enlarged lysosomes clustered in the periphery of *Gnpt*-KO enterocytes for the survival and replication of bacteria and studies on the underlying mechanisms resulting in the loss of lysosome mobility in *Gnpt*-KO cells, will be in the focus of future studies.

# 5. Summary (English)

*Yersinia enterocolitica* belongs to the enteropathogenic, disease-causing bacteria that invade the epithelial cells of the intestinal tract. The intracellular compartments, the transport pathways and the proteins of the transport machinery in phagocytic host cells appear to be of particular importance for the survival and proliferation of *Yersinia*. In recent years, it has been observed that the autophagy-lysosome pathway for the degradation of macromolecules, damaged organelles and pathogens can be subverted and manipulated by *Yersinia* to bypass lysosomal elimination and to generate a replication niche. In this work, the role of the autophagy-lysosome pathway for *Yersinia* infection was investigated in physiologically relevant cell models and compared with cells whose degradation capacity is blocked by loss of most lysosomal enzymes. For this purpose, 1) the *Gnpt*-KO was established in the intestinal epithelial cell line MODE-K, and 2) intestinal organoids from control and *Gnpt*$^{ki}$ mice with dysfunctional lysosomes were prepared and characterized cell biologically and biochemically.

The number and size of perinuclearly localized lysosomes were increased in *Gnpt*-KO MODE-K cells. The loss of function of *Gnpt*-KO lysosomes caused by missorting of lysosomal enzymes was detectable by proteome analyses and the lysosomal accumulation of storage material at unchanged pH. The abundance of several proteins in the isolated lysosomal fractions involved in autophagosome formation were strongly increased, which correlates with immunofluorescence microscopy data on activated autophagy and in *Gnpt*-KO cells with concomitant block of autophago-lysosome formation. Lipidomic analyses of isolated lysosomes showed strong differences between control and *Gnpt*-KO cells of 14 lipid classes. In the polarized cells of *Gnpt*$^{ki}$organoids, clusters of enlarged, immobile lysosomes are localized below the apical membrane. The results suggest that the altered lipid composition of *Gnpt*-KO lysosomes influences the recruitment and interaction of components of the mobility apparatus and causes the reduced motility and altered positioning.

When MODE-K monolayer on filters were infected with fluorophore-labelled *Y.enterocolitica*, the bacteria were detectable intracellularly in both control and *Gnpt*-KO cells not in CytoID-positive autophagosomes, but in Lamp1-positive single-membrane organelles, which could be defined as lysosomes using BSA-gold. The establishment of apical-out organoids allows the infection of this multi-cellular system with *Y.enterocolitica*, to investigate the intracellular transport pathway and the role of autophagosomes and lysosomes for bacterial proliferation and survival.

# 6. Zusammenfassung (Deutsch)

*Yersinia enterocolitica* gehört zu den enteropathogenen, krankheitsverursachenden Bakterien, die in die Epithelzellen des intestinalen Darmtraktes eindringen. Für das Überleben und die Vermehrung der *Yersinien* scheinen die intrazellulären Kompartimente, die Transportwege und die Proteine der Transportmaschinerie in phagozytotischen Wirtszellen von besonderer Bedeutung zu sein. In den letzten Jahren wurde beobachtet, dass der Autophagie-Lysosomen-Weg für den Abbau von Makromolekülen, geschädigten Organellen und Pathogenen, durch *Yersinien* untergraben und manipuliert werden kann, um die lysosomale Eliminierung zu umgehen und um eine Replikationsnische zu generieren. In dieser Arbeit sollte die Rolle des Autophagie-Lysosomen-Weges für die Yersinia Infektion in physiologisch relevanten Zellmodellen untersucht und mit Zellen verglichen werden, deren Abbaukapazität durch Verlust der meisten lysosomalen Enzyme blockiert ist. Dazu wurden zunächst 1.) der *Gnpt*-KO in der intestinalen Epithelzelllinie MODE-K etabliert, und 2.) intestinale Organoide aus Kontroll- und *Gnpt*$^{ki}$ Mäusen mit dysfunktionalen Lysosomen, präpariert, und zellbiologisch und biochemisch charakterisiert.

Die Anzahl und Größe der perinukleär lokalisierten Lysosomen waren in *Gnpt*-KO MODE-K Zellen erhöht. Der Funktionsverlust der *Gnpt*-KO Lysosomen durch Fehlsortierung lysosomaler Enzyme war durch Proteomanalyse isolierter Lysosomen und die Akkumulation von Speichermaterial bei unverändertem pH-Wert nachweisbar. Die Abundanz mehrerer Proteine in den Lysosomenfraktionen, die an der Bildung von Autophagosomen beteiligt sind, waren stark erhöht, was mit Immunfluoreszenz-mikroskopischen Daten zur aktivierten Autophagie und in *Gnpt*-KO Zellen korreliert bei gleichzeitigem Block der Bildung von Autophago-lysosomen. Lipidomanalysen von isolierten Lysosomenfraktionen wiesen starke Unterschiede zwischen Kontroll und *Gnpt*-KO Zellen auf, die 14 Lipidklassen betrafen. In den polarisierten Zellen der *Gnpt*$^{ki}$ Organoide sind Cluster von vergrößerten, unbeweglichen Lysosomen unterhalb der apikalen Membran lokalisiert. Die Ergebnisse lassen vermuten, dass die veränderte Lipidzusammensetzung der *Gnpt*-KO Lysosomen die Rekrutierung und Wechselwirkung von Komponenten des Mobilitätsapparates beeinflusst und die reduzierte Beweglichkeit und veränderte Positionierung bewirkt.

Wenn MODE-K Monolayer auf Filtern mit Fluorophor-markierten *Y. enterocolitica* infiziert wurden, waren die Bakterien intrazellulär sowohl in Kontroll- als auch *Gnpt*-KO Zellen, nicht in CytoID-positiven Autophagosomen, aber in Lamp1-positiven Einzelmembran-Organellen nachweisbar, die mit BSA-Gold als Lysosomen definiert werden konnten. Die Etablierung von apikal-out Organoiden ermöglicht die Infektion dieses multizellulären Systems mit *Y.enterocolitica,* zu Untersuchungen des intrazellulären Transportweges und zur Rolle von Autophagosomen und Lysosomen für Vermehrung und Überleben der Bakterien.

# 7. References

Asanuma, K., et al. (2003). "MAP-LC3, a promising autophagosomal marker, is processed during the differentiation and recovery of podocytes from PAN nephrosis." Faseb j 17(9): 1165-1167.

Badenetti, L., et al. (2024). "Multi-omic analysis of a mucolipidosis II neuronal cell model uncovers involvement of pathways related to neurodegeneration and drug metabolism." Mol Genet Metab 143(3): 108596.

Ballabio, A. and J. S. Bonifacino (2020). "Lysosomes as dynamic regulators of cell and organismal homeostasis." Nat Rev Mol Cell Biol 21(2): 101-118.

Bao, M., et al. (1996). "Bovine UDP-N-acetylglucosamine:lysosomal-enzyme N-acetylglucosamine-1-phosphotransferase. I. Purification and subunit structure." J Biol Chem 271(49): 31437-31445.

Boonekamp, K. E., et al. (2020). "Intestinal organoids as tools for enriching and studying specific and rare cell types: advances and future directions." J Mol Cell Biol 12(8): 562-568.

Boonen, M., et al. (2011). "Vacuolization of mucolipidosis type II mouse exocrine gland cells represents accumulation of autolysosomes." Mol Biol Cell 22(8): 1135-1147.

Bosshard, N. U., et al. (1996). "Spontaneous mucolipidosis in a cat: an animal model of human I-cell disease." Vet Pathol 33(1): 1-13.

Brauer, B. K., et al. (2024). "GOLPH3 and GOLPH3L maintain Golgi localization of LYSET and a functional mannose 6-phosphate transport pathway." Embo j 43(24): 6264-6290.

Braulke, T. and J. S. Bonifacino (2009). "Sorting of lysosomal proteins." Biochim Biophys Acta 1793(4): 605-614.

Braulke, T., et al. (2024). "Lysosomal enzyme trafficking: from molecular mechanisms to human diseases." Trends Cell Biol 34(3): 198-210.

Braulke, T., et al. (2008). "Molecular analysis of the GlcNac-1-phosphotransferase." J Inherit Metab Dis 31(2): 253-257.

Bulgin, R., et al. (2010). "Bacterial guanine nucleotide exchange factors SopE-like and WxxxE effectors." Infect Immun 78(4): 1417-1425.

Cabukusta, B. and J. Neefjes (2018). "Mechanisms of lysosomal positioning and movement." Traffic 19(10): 761-769.

Cao, X., et al. (2012). "Polarized sorting and trafficking in epithelial cells." Cell Res 22(5): 793-805.

Capuozzo, A., et al. (2022). "Fluoxetine ameliorates mucopolysaccharidosis type IIIA." Mol Ther 30(4): 1432-1450.

Caramelo, J. J. and A. J. Parodi (2008). "Getting in and out from calnexin/calreticulin cycles." J Biol Chem 283(16): 10221-10225.

Carlsson, S. R. and M. Fukuda (1992). "The lysosomal membrane glycoprotein lamp-1 is transported to lysosomes by two alternative pathways." Arch Biochem Biophys 296(2): 630-639.

# References

Casey, J. R., et al. (2010). "Sensors and regulators of intracellular pH." Nat Rev Mol Cell Biol 11(1): 50-61.

Chan, L. L., et al. (2012). "A novel image-based cytometry method for autophagy detection in living cells." Autophagy 8(9): 1371-1382.

Chen, C., et al. (2024). "ABCG2 is an itaconate exporter that limits antibacterial innate immunity by alleviating TFEB-dependent lysosomal biogenesis." Cell Metab 36(3): 498-510.e411.

Co, J. Y., et al. (2019). "Controlling Epithelial Polarity: A Human Enteroid Model for Host-Pathogen Interactions." Cell Rep 26(9): 2509-2520.e2504.

Co, J. Y., et al. (2021). "Controlling the polarity of human gastrointestinal organoids to investigate epithelial biology and infectious diseases." Nat Protoc 16(11): 5171-5192.

de Araujo, M. E. G., et al. (2020). "Lysosomal size matters." Traffic 21(1): 60-75.

De Pace, R., et al. (2015). "Subunit interactions of the disease-related hexameric GlcNAc-1-phosphotransferase complex." Hum Mol Genet 24(23): 6826-6835.

Deuretzbacher, A., et al. (2009). "Beta1 integrin-dependent engulfment of Yersinia enterocolitica by macrophages is coupled to the activation of autophagy and suppressed by type III protein secretion." J Immunol 183(9): 5847-5860.

Di Lorenzo, G., et al. (2018). "Lysosomal Proteome and Secretome Analysis Identifies Missorted Enzymes and Their Nondegraded Substrates in Mucolipidosis III Mouse Cells." Mol Cell Proteomics 17(8): 1612-1626.

Ebner, M., et al. (2023). "Nutrient-regulated control of lysosome function by signaling lipid conversion." Cell 186(24): 5328-5346.e5326.

Encarnação, M., et al. (2016). "A Rab3a-dependent complex essential for lysosome positioning and plasma membrane repair." J Cell Biol 213(6): 631-640.

Eriksson, I. and K. Öllinger (2024). "Lysosomes in Cancer-At the Crossroad of Good and Evil." Cells 13(5).

Ershov, D., et al. (2022). "TrackMate 7: integrating state-of-the-art segmentation algorithms into tracking pipelines." Nat Methods 19(7): 829-832.

Farías, G. G., et al. (2017). "BORC/kinesin-1 ensemble drives polarized transport of lysosomes into the axon." Proc Natl Acad Sci U S A 114(14): E2955-e2964.

Flanagan-Steet, H., et al. (2016). "Cathepsin-Mediated Alterations in TGFß-Related Signaling Underlie Disrupted Cartilage and Bone Maturation Associated With Impaired Lysosomal Targeting." J Bone Miner Res 31(3): 535-548.

Flanagan-Steet, H., et al. (2009). "Altered chondrocyte differentiation and extracellular matrix homeostasis in a zebrafish model for mucolipidosis II." Am J Pathol 175(5): 2063-2075.

Franke, M., et al. (2013). "Transport of the GlcNAc-1-phosphotransferase α/β-subunit precursor protein to the Golgi apparatus requires a combinatorial sorting motif." J Biol Chem 288(2): 1238-1249.

# References

Fratti, R. A., et al. (2001). "Role of phosphatidylinositol 3-kinase and Rab5 effectors in phagosomal biogenesis and mycobacterial phagosome maturation arrest." J Cell Biol 154(3): 631-644.

Fromme, J. C. and R. Schekman (2005). "COPII-coated vesicles: flexible enough for large cargo?" Curr Opin Cell Biol 17(4): 345-352.

Galmes, R., et al. (2015). "Vps33B is required for delivery of endocytosed cargo to lysosomes." Traffic 16(12): 1288-1305.

Gehart, H. and H. Clevers (2019). "Tales from the crypt: new insights into intestinal stem cells." Nat Rev Gastroenterol Hepatol 16(1): 19-34.

Gelfman, C. M., et al. (2007). "Mice lacking alpha/beta subunits of GlcNAc-1-phosphotransferase exhibit growth retardation, retinal degeneration, and secretory cell lesions." Invest Ophthalmol Vis Sci 48(11): 5221-5228.

Ghosh, P., et al. (2003). "Mannose 6-phosphate receptors: new twists in the tale." Nat Rev Mol Cell Biol 4(3): 202-212.

Gorelik, A., et al. (2022). "Structures of the mannose-6-phosphate pathway enzyme, GlcNAc-1-phosphotransferase." Proc Natl Acad Sci U S A 119(33): e2203518119.

Helenius, A. and M. Aebi (2001). "Intracellular functions of N-linked glycans." Science 291(5512): 2364-2369.

Irazoqui, J. E. (2020). "Key Roles of MiT Transcription Factors in Innate Immunity and Inflammation." Trends Immunol 41(2): 157-171.

Johnson, D. E., et al. (2016). "The position of lysosomes within the cell determines their luminal pH." J Cell Biol 212(6): 677-692.

Keren-Kaplan, T., et al. (2022). "RUFY3 and RUFY4 are ARL8 effectors that promote coupling of endolysosomes to dynein-dynactin." Nat Commun 13(1): 1506.

Kobayashi, T., et al. (1998). "A lipid associated with the antiphospholipid syndrome regulates endosome structure and function." Nature 392(6672): 193-197.

Koehne, T., et al. (2016). "Mannose 6-phosphate-dependent targeting of lysosomal enzymes is required for normal craniofacial and dental development." Biochim Biophys Acta 1862(9): 1570-1580.

Kollmann, K., et al. (2012). "Lysosomal dysfunction causes neurodegeneration in mucolipidosis II 'knock-in' mice." Brain 135(Pt 9): 2661-2675.

Kollmann, K., et al. (2013). "Decreased bone formation and increased osteoclastogenesis cause bone loss in mucolipidosis II." EMBO Mol Med 5(12): 1871-1886.

Kollmann, K., et al. (2010). "Mannose phosphorylation in health and disease." Eur J Cell Biol 89(1): 117-123.

Kondo, Y., et al. (2018). "Site-1 protease deficiency causes human skeletal dysplasia due to defective inter-organelle protein trafficking." JCI Insight 3(14).

# References

Kornfeld, S. S., W. S. (2001). I-cell disease and pseudo-Hurler polydystrophy: disorders of lysosomal enzyme phosphorylation and localization. The Metabolic and Molecular Bases of Inherited Disease, 8.

Korolchuk, V. I., et al. (2011). "Lysosomal positioning coordinates cellular nutrient responses." Nat Cell Biol 13(4): 453-460.

Kraus, F., et al. (2025). "Global cellular proteo-lipidomic profiling of diverse lysosomal storage disease mutants using nMOST." Sci Adv 11(4): eadu5787.

Kudo, M., et al. (2005). "The alpha- and beta-subunits of the human UDP-N-acetylglucosamine:lysosomal enzyme N-acetylglucosamine-1-phosphotransferase [corrected] are encoded by a single cDNA." J Biol Chem 280(43): 36141-36149.

Kudo, M. and W. M. Canfield (2006). "Structural requirements for efficient processing and activation of recombinant human UDP-N-acetylglucosamine:lysosomal-enzyme-N-acetylglucosamine-1-phosphotransferase." J Biol Chem 281(17): 11761-11768.

Kumar, G., et al. (2022). "RUFY3 links Arl8b and JIP4-Dynein complex to regulate lysosome size and positioning." Nat Commun 13(1): 1540.

Kwiatkowska, K., et al. (2014). "Visualization of cholesterol deposits in lysosomes of Niemann-Pick type C fibroblasts using recombinant perfringolysin O." Orphanet J Rare Dis 9: 64.

Laplante, M. and D. M. Sabatini (2012). "mTOR signaling in growth control and disease." Cell 149(2): 274-293.

Lazzarino, D. A. and C. A. Gabel (1989). "Mannose processing is an important determinant in the assembly of phosphorylated high mannose-type oligosaccharides." J Biol Chem 264(9): 5015-5023.

Leibiger, R., et al. (2008). "Yersinia enterocolitica Yop mutants as oral live carrier vaccines." Vaccine 26(51): 6664-6670.

Lemarignier, M. and J. Pizarro-Cerdá (2020). "Autophagy and Intracellular Membrane Trafficking Subversion by Pathogenic Yersinia Species." Biomolecules 10(12).

Leroy, J. G. and R. I. Demars (1967). "Mutant enzymatic and cytological phenotypes in cultured human fibroblasts." Science 157(3790): 804-806.

Li, H., et al. (2024). "Structure of a truncated human GlcNAc-1-phosphotransferase variant reveals the basis for its hyperactivity." J Biol Chem 300(9): 107706.

Li, P., et al. (2020). "LRRC8 family proteins within lysosomes regulate cellular osmoregulation and enhance cell survival to multiple physiological stresses." Proc Natl Acad Sci U S A 117(46): 29155-29165.

Li, X., et al. (2016). "A molecular mechanism to regulate lysosome motility for lysosome positioning and tubulation." Nat Cell Biol 18(4): 404-417.

Ligeon, L. A., et al. (2014). "Role of VAMP3 and VAMP7 in the commitment of Yersinia pseudotuberculosis to LC3-associated pathways involving single- or double-membrane vacuoles." Autophagy 10(9): 1588-1602.

# References

Lolicato, F., et al. (2024). "Phosphoinositide switches in cell physiology - From molecular mechanisms to disease." J Biol Chem 300(3): 105757.

Lu, P. N., et al. (2020). "Inappropriate cathepsin K secretion promotes its enzymatic activation driving heart and valve malformation." JCI Insight 5(20).

Luzio, J. P., et al. (2007). "Lysosomes: fusion and function." Nat Rev Mol Cell Biol 8(8): 622-632.

Mahe, M. M., et al. (2013). "Establishment of Gastrointestinal Epithelial Organoids." Curr Protoc Mouse Biol 3(4): 217-240.

Makrypidi, G., et al. (2012). "Mannose 6 dephosphorylation of lysosomal proteins mediated by acid phosphatases Acp2 and Acp5." Mol Cell Biol 32(4): 774-782.

Markmann, S., et al. (2017). "Quantitative Proteome Analysis of Mouse Liver Lysosomes Provides Evidence for Mannose 6-phosphate-independent Targeting Mechanisms of Acid Hydrolases in Mucolipidosis II." Mol Cell Proteomics 16(3): 438-450.

Markmann, S., et al. (2015). "Lrp1/LDL Receptor Play Critical Roles in Mannose 6-Phosphate-Independent Lysosomal Enzyme Targeting." Traffic 16(7): 743-759.

Marschner, K., et al. (2011). "A key enzyme in the biogenesis of lysosomes is a protease that regulates cholesterol metabolism." Science 333(6038): 87-90.

McGourty, K., et al. (2012). "Salmonella inhibits retrograde trafficking of mannose-6-phosphate receptors and lysosome function." Science 338(6109): 963-967.

McGuckin, M. A., et al. (2011). "Mucin dynamics and enteric pathogens." Nat Rev Microbiol 9(4): 265-278.

Merciai, F., et al. (2022). "Development and application of a fast ultra-high performance liquid chromatography-trapped ion mobility mass spectrometry method for untargeted lipidomics." J Chromatogr A 1673: 463124.

Mohan, N., et al. (2019). "Detyrosinated microtubules spatially constrain lysosomes facilitating lysosome-autophagosome fusion." J Cell Biol 218(2): 632-643.

Mosen, P., et al. (2021). "Targeted Quantification of the Lysosomal Proteome in Complex Samples." Proteomes 9(1).

Nakatogawa, H. (2020). "Mechanisms governing autophagosome biogenesis." Nat Rev Mol Cell Biol 21(8): 439-458.

Nanayakkara, R., et al. (2023). "Autophagic lysosome reformation in health and disease." Autophagy 19(5): 1378-1395.

Otomo, T., et al. (2009). "Inhibition of autophagosome formation restores mitochondrial function in mucolipidosis II and III skin fibroblasts." Mol Genet Metab 98(4): 393-399.

Otomo, T., et al. (2011). "Lysosomal storage causes cellular dysfunction in mucolipidosis II skin fibroblasts." J Biol Chem 286(40): 35283-35290.

# References

Otomo, T., et al. (2015). "Mannose 6 phosphorylation of lysosomal enzymes controls B cell functions." J Cell Biol 208(2): 171-180.

Oughtred, R., et al. (2021). "The BioGRID database: A comprehensive biomedical resource of curated protein, genetic, and chemical interactions." Protein Sci 30(1): 187-200.

Pechincha, C., et al. (2022). "Lysosomal enzyme trafficking factor LYSET enables nutritional usage of extracellular proteins." Science 378(6615): eabn5637.

Perera, R. M. and R. Zoncu (2016). "The Lysosome as a Regulatory Hub." Annu Rev Cell Dev Biol 32: 223-253.

Pols, M. S., et al. (2013). "hVps41 and VAMP7 function in direct TGN to late endosome transport of lysosomal membrane proteins." Nat Commun 4: 1361.

Poole, B. and S. Ohkuma (1981). "Effect of weak bases on the intralysosomal pH in mouse peritoneal macrophages." J Cell Biol 90(3): 665-669.

Pu, J., et al. (2016). "Mechanisms and functions of lysosome positioning." J Cell Sci 129(23): 4329-4339.

Pu, J., et al. (2015). "BORC, a multisubunit complex that regulates lysosome positioning." Dev Cell 33(2): 176-188.

Puertollano, R., et al. (2018). "The complex relationship between TFEB transcription factor phosphorylation and subcellular localization." Embo j 37(11).

Qian, Y., et al. (2010). "Functions of the alpha, beta, and gamma subunits of UDP-GlcNAc:lysosomal enzyme N-acetylglucosamine-1-phosphotransferase." J Biol Chem 285(5): 3360-3370.

Raas-Rothschild, A., et al. (2000). "Molecular basis of variant pseudo-hurler polydystrophy (mucolipidosis IIIC)." J Clin Invest 105(5): 673-681.

Ren, H. and G. Wang (2020). "Autophagy and Lysosome Storage Disorders." Adv Exp Med Biol 1207: 87-102.

Ribet, D. and P. Cossart (2015). "How bacterial pathogens colonize their hosts and invade deeper tissues." Microbes Infect 17(3): 173-183.

Richards, C. M., et al. (2022). "The human disease gene LYSET is essential for lysosomal enzyme transport and viral infection." Science 378(6615): eabn5648.

Rink, J., et al. (2005). "Rab conversion as a mechanism of progression from early to late endosomes." Cell 122(5): 735-749.

Roney, J. C., et al. (2021). "Lipid-mediated motor-adaptor sequestration impairs axonal lysosome delivery leading to autophagic stress and dystrophy in Niemann-Pick type C." Dev Cell 56(10): 1452-1468.e1458.

Ruddock, L. W. and M. Molinari (2006). "N-glycan processing in ER quality control." J Cell Sci 119(Pt 21): 4373-4380.

# References

Runwal, G., et al. (2019). "LC3-positive structures are prominent in autophagy-deficient cells." Sci Rep 9(1): 10147.

Sachdeva, K. and V. Sundaramurthy (2020). "The Interplay of Host Lysosomes and Intracellular Pathogens." Front Cell Infect Microbiol 10: 595502.

Sachs, W., et al. (2020). "Distinct Modes of Balancing Glomerular Cell Proteostasis in Mucolipidosis Type II and III Prevent Proteinuria." J Am Soc Nephrol 31(8): 1796-1814.

Scerra, G., et al. (2022). "Lysosomal positioning diseases: beyond substrate storage." Open Biol 12(10): 220155.

Schindelin, J., et al. (2012). "Fiji: an open-source platform for biological-image analysis." Nat Methods 9(7): 676-682.

Schmidtke, C., et al. (2019). "Lysosomal proteome analysis reveals that CLN3-defective cells have multiple enzyme deficiencies associated with changes in intracellular trafficking." J Biol Chem 294(24): 9592-9604.

Schneeberger, K., et al. (2018). "Intestinal epithelial cell polarity defects in disease: lessons from microvillus inclusion disease." Dis Model Mech 11(2).

Schuster, E. M., et al. (2022). "TFEB induces mitochondrial itaconate synthesis to suppress bacterial growth in macrophages." Nat Metab 4(7): 856-866.

Schweizer, M., et al. (2013). "Ultrastructural analysis of neuronal and non-neuronal lysosomal storage in mucolipidosis type II knock-in mice." Ultrastruct Pathol 37(5): 366-372.

Seidah, N. G. and A. Prat (2012). "The biology and therapeutic targeting of the proprotein convertases." Nat Rev Drug Discov 11(5): 367-383.

Seranova, E., et al. (2017). "Dysregulation of autophagy as a common mechanism in lysosomal storage diseases." Essays Biochem 61(6): 733-749.

Spanò, S. and J. E. Galán (2018). "Taking control: Hijacking of Rab GTPases by intracellular bacterial pathogens." Small GTPases 9(1-2): 182-191.

Steinberg, B. E., et al. (2010). "A cation counterflux supports lysosomal acidification." J Cell Biol 189(7): 1171-1186.

Takla, M., et al. (2023). "The post-translational regulation of transcription factor EB (TFEB) in health and disease." EMBO Rep 24(11): e57574.

Tarantino, N., et al. (2014). "TNF and IL-1 exhibit distinct ubiquitin requirements for inducing NEMO-IKK supramolecular structures." J Cell Biol 204(2): 231-245.

Teixeira, S. C., et al. (2023). "Subversion strategies of lysosomal killing by intracellular pathogens." Microbiol Res 277: 127503.

Thelen, M., et al. (2017). "SILAC-Based Comparative Proteomic Analysis of Lysosomes from Mammalian Cells Using LC-MS/MS." Methods Mol Biol 1594: 1-18.

# References

Tiede, S., et al. (2005). "Mucolipidosis II is caused by mutations in GNPTA encoding the alpha/beta GlcNAc-1-phosphotransferase." Nat Med 11(10): 1109-1112.

Valencia Lopez, M. J., et al. (2019). "Activation of the macroautophagy pathway by Yersinia enterocolitica promotes intracellular multiplication and egress of yersiniae from epithelial cells." Cell Microbiol 21(9): e13046.

Velho, R. V., et al. (2017). "Site-1 protease and lysosomal homeostasis." Biochim Biophys Acta Mol Cell Res 1864(11 Pt B): 2162-2168.

Vidal, K., et al. (1993). "Immortalization of mouse intestinal epithelial cells by the SV40-large T gene. Phenotypic and immune characterization of the MODE-K cell line." J Immunol Methods 166(1): 63-73.

Vonk, A. M., et al. (2020). "Protocol for Application, Standardization and Validation of the Forskolin-Induced Swelling Assay in Cystic Fibrosis Human Colon Organoids." STAR Protoc 1(1): 100019.

Walter, P., et al. (1984). "Protein translocation across the endoplasmic reticulum." Cell 38(1): 5-8.

Wang, Z., et al. (2024). "Insights into the role of legionella effectors on host metabolic perturbations." Front Cell Infect Microbiol 14: 1458276.

Weber, K., et al. (2008). "A multicolor panel of novel lentiviral "gene ontology" (LeGO) vectors for functional gene analysis." Mol Ther 16(4): 698-706.

Weesner, J. A., et al. (2023). "Glycosphingolipids within membrane contact sites influence their function as signaling hubs in neurodegenerative diseases." FEBS Open Bio 13(9): 1587-1600.

Weinert, S., et al. (2010). "Lysosomal pathology and osteopetrosis upon loss of H+-driven lysosomal Cl- accumulation." Science 328(5984): 1401-1403.

Wiesmann, U. N., et al. (1971). "Multiple lysosomal enzyme deficiency due to enzyme leakage?" N Engl J Med 284(2): 109-110.

Willett, R., et al. (2017). "TFEB regulates lysosomal positioning by modulating TMEM55B expression and JIP4 recruitment to lysosomes." Nat Commun 8(1): 1580.

Xu, H. and D. Ren (2015). "Lysosomal physiology." Annu Rev Physiol 77: 57-80.

Yadati, T., et al. (2020). "The Ins and Outs of Cathepsins: Physiological Function and Role in Disease Management." Cells 9(7).

Yamamoto, H., et al. (2023). "Autophagy genes in biology and disease." Nat Rev Genet 24(6): 382-400.

Yang, J., et al. (2001). "Decreased lipid synthesis in livers of mice with disrupted Site-1 protease gene." Proc Natl Acad Sci U S A 98(24): 13607-13612.

Ye, J., et al. (2000). "ER stress induces cleavage of membrane-bound ATF6 by the same proteases that process SREBPs." Mol Cell 6(6): 1355-1364.

Zanetti, G., et al. (2011). "COPII and the regulation of protein sorting in mammals." Nat Cell Biol 14(1): 20-28.

# References

Zhang, Z., et al. (2022). "Itaconate is a lysosomal inducer that promotes antibacterial innate immunity." Mol Cell 82(15): 2844-2857.e2810.

Zhao, K. and N. D. Ridgway (2017). "Oxysterol-Binding Protein-Related Protein 1L Regulates Cholesterol Egress from the Endo-Lysosomal System." Cell Rep 19(9): 1807-1818.

Zhao, Q., et al. (2020). "Molecular Mechanisms of Lysosome and Nucleus Communication." Trends Biochem Sci 45(11): 978-991.

Zhao, Y. G., et al. (2021). "Machinery, regulation and pathophysiological implications of autophagosome maturation." Nat Rev Mol Cell Biol 22(11): 733-750.

Zhen, Y. and H. Stenmark (2023). "Autophagosome Biogenesis." Cells 12(4).

# 8. Supplementary Tables

For each of the following Supplementary Table the significance intervals are ≥ 1.7 for the y- axis ($\log_{10}$ p-value) and ≤ -0.58 and ≥ +0.58 for the x-axis ($\log_2$ fold change). [1] log2 fold change

**Supplementary Table S1 A.** Soluble lysosomal enzymes and accessory proteins identified by Targeted MS in cell extracts of wt and *Gnpt*$^{ki}$ organoids (n=3); related to Figure 3.5 A.

| | **UniProt ID** | **Protein** | **Description** | **Mean ± SD KO/wt[1]** |
|---|---|---|---|---|
| **1** | Q64191 | **Aga** | N(4)-(beta-N-acetylglucosaminyl)-L-asparaginase | -2.10±0.47 |
| **2** | P50429 | **Arsb** | Arylsulfatase B | -1.52±0.43 |
| **3** | Q3UMW8 | **Cln5** | Ceroid-lipofuscinosis neuronal protein 5 | -0.94±0.43 |
| **4** | Q8R242 | **Ctbs** | Di-N-acetylchitobiase | -0.97±0.58 |
| **5** | P97821 | **Ctsc** | Cathepsin C | -1.26±0.23 |
| **6** | P49935 | **Ctsh** | Cathepsin H | -2.40±0.51 |
| **7** | Q9WUU7 | **Ctsz** | Cathepsin Z | -1.77±0.59 |
| **8** | P56542 | **Dnase2** | Deoxyribonuclease-2-alpha | -0.97±0.32 |
| **9** | Q9ET22 | **Dpp7** | Dipeptidyl peptidase 2 | -1.49±0.51 |
| **10** | Q99LJ1 | **Fuca1** | Tissue alpha-L-fucosidase | -0.96±0.23 |
| **11** | P54818 | **Galc** | Galactocerebrosidase | -0.54±0.27 |
| **12** | Q9Z0L8 | **Ggh** | Gamma-glutamyl hydrolase | -0.81±0.43 |
| **13** | P51569 | **Gla** | Alpha-galactosidase | -1.03±0.27 |
| **14** | P23780 | **Glb1** | Beta-galactosidase | -1.37±0.88 |
| **15** | Q8BFR4 | **Gns** | N-acetylglucosamine-6-sulfatase | -0.76±0.29 |
| **16** | P29416 | **Hexa** | Beta-hexosaminidase subunit alpha | -1.61±0.46 |
| **17** | P20060 | **Hexb** | Beta-hexosaminidase subunit beta | -0.90±0.22 |
| **18** | Q6YGZ1 | **Hpse** | Heparanase | -1.19±0.51 |
| **19** | O09159 | **Man2b1** | Lysosomal alpha-mannosidase | -1.16±0.44 |
| **20** | O54782 | **Man2b2** | Epididymis-specific alpha-mannosidase | -1.59±0.40 |
| **21** | Q8K2I4 | **Manba** | Beta-mannosidase | -0.98±0.74 |
| **22** | O88325 | **Naglu** | Alpha-N-acetylglucosaminidase | -0.56±0.31 |
| **23** | Q9Z0J0 | **Npc2** | Niemann-Pick type C2, intracellular cholesterol transporter 2 | -1.47±0.47 |
| **24** | Q8VEB4 | **Pla2g15** | Group XV phospholipase A2 | -0.56±0.55 |
| **25** | Q7TMR0 | **Prcp** | Lysosomal Pro-X carboxypeptidase | -1.71±0.44 |

| | | | | |
|---|---|---|---|---|
| 26 | Q920A5 | **Scpep1** | Retinoid-inducible serine carboxypeptidase | -1.30±0.46 |
| 27 | Q9EQ08 | **Sgsh** | Heparan N-sulfatase | -1.86±0.41 |
| 28 | P70665 | **Siae** | Sialate O-acetylesterase | -1.09±0.29 |
| 29 | P10605 | **Ctsb** | Cathepsin B | +0.82±0.47 |
| 30 | P28798 | **Grn** | Progranulin | +5.87±0.34 |
| 31 | O35405 | **Pld3** | Phospholipase D3 | +0.69±0.21 |
| 32 | Q61207 | **Psap** | Prosaposin | +0.66±1.22 |
| 33 | Q04519 | **Smpd1** | Sphingomyelin phosphodiesterase | +0.64±0.53 |

**Supplementary Table S1 C.** Lysosomal membrane proteins identified by Targeted MS in cell extracts of wt and *Gnpt*$^{ki}$ organoids (n=3); related to Figure 3.5 C.

| | **UniProt ID** | **Protein** | **Description** | **Mean ± SD KO/wt[1]** |
|---|---|---|---|---|
| 1 | Q9R1Q9 | **Atp6ap1** | V-type proton ATPase subunit S1 | -0.24±0.35 |
| 2 | P51863 | **Atp6v0d1** | V-type proton ATPase subunit d 1 | -0.50±0.15 |
| 3 | P50516 | **Atp6v1a** | V-type proton ATPase catalytic subunit A | +0.17±0.28 |
| 4 | P62814 | **Atp6v1b2** | V-type proton ATPase subunit B | +0.30±0.18 |
| 5 | Q9Z1G3 | **Atp6v1c1** | V-type proton ATPase subunit C 1 | +0.04±0.27 |
| 6 | P57746 | **Atp6v1d** | V-type proton ATPase subunit D | +0.23±0.21 |
| 7 | P50518 | **Atp6v1e1** | V-type proton ATPase subunit E 1 | -0.03±0.72 |
| 8 | Q9D1K2 | **Atp6v1f** | V-type proton ATPase subunit F | -0.35±0.31 |
| 9 | Q9CR51 | **Atp6v1g1** | V-type proton ATPase subunit G | -0.38±0.96 |
| 10 | Q8BVE3 | **Atp6v1h** | V-type proton ATPase subunit H | +0.48±0.84 |
| 11 | P17047 | **Lamp2** | Lysosome-associated membrane glycoprotein 2 | +0.54±0.11 |
| 12 | Q9JLJ0 | **Litaf** | Lipopolysaccharide-induced tumor necrosis factor-alpha factor homolog | +0.40±0.49 |
| 13 | P57716 | **Ncstn** | Nicastrin | +0.34±0.29 |
| 14 | O35604 | **Npc1** | Niemann-Pick type C1, intracellular cholesterol transporter 1 | +0.30±0.20 |
| 15 | Q8BN82 | **Slc17a5** | Sialin | +0.60±0.27 |
| 16 | Q99P65 | **Slc29a3** | Equilibrative nucleoside transporter 3 | +0.54±0.37 |
| 17 | Q8BGD6 | **Slc38a7** | Arg-regulated non-polar amino acid transporter 7 | +0.53±0.60 |
| 18 | Q9CR23 | **Tmem9** | Transmembrane protein 9 | +1.35±2.29 |

| | | | | |
|---|---|---|---|---|
| 19 | Q5SYH2 | **Tmem199** | Transmembrane protein 199 | -0.81±0.62 |
| 20 | O70496 | **Clc7** | H(+)/Cl(-) exchange transporter 7 | +1.63±1.22 |
| 21 | Q9CR48 | **Dram2** | DNA damage-regulated autophagy modulator protein 2 | +0.69±0.25 |
| 22 | Q9JHJ3 | **Glmp** | Glycosylated lysosomal membrane protein | +2.73±0.29 |
| 23 | Q3UDW8 | **Hgsnat** | Heparan-alpha-glucosaminide N-acetyltransferase | +1.06±0.34 |
| 24 | P11438 | **Lamp1** | Lysosome-associated membrane glycoprotein 1 | +0.60±0.19 |
| 25 | Q5U4H9 | **Ncoa4** | Nuclear receptor coactivator 4 | +2.36±1.02 |

**Supplementary Table S1 E.** Proteins involved in lysosomal mobility identified by Targeted MS in cell extracts of wt and *Gnpt*$^{ki}$ organoids (n=3); related to Figure 3.5 E.

| | **UniProt ID** | **Protein** | **Description** | **Mean ± SD KO/wt[1]** |
|---|---|---|---|---|
| 1 | P28740 | **Kif2a** | Kinesin-like protein KIF2A | -0.17±0.60 |
| 2 | O55102 | **Bloc1s1** | Biogenesis of lysosome-related organelles complex 1 subunit 1 | -0.14±0.17 |
| 3 | Q80X71 | **Tmem106b** | Transmembrane protein 106B | +0.15±0.57 |
| 4 | Q9CWG9 | **Bloc1s2** | Biogenesis of lysosome-related organelles complex 1 subunit 2 | +0.06±0.33 |
| 5 | P51150 | **Rab7a** | Ras-related protein Rab-7a | +0.09±0.08 |
| 6 | Q8VEH3 | **Arl8a** | ADP-ribosylation factor-like protein 8A | -3.25±0.71 |
| 7 | Q9CRC6 | **Borcs7** | BLOC-1-related complex subunit 7 | -1.55±0.07 |
| 8 | Q9CQW2 | **Arl8b** | ADP-ribosylation factor-like protein 8B | +0.61±0.39 |

# Supplementary Tables

For each of the following Supplementary Table the significance intervals are ≥ 1.3 for the y-axis ($\log_{10}$ p-value) and ≤ -0.58 and ≥ +0.58 for the x-axis ($\log_2$ fold change). [1] log2 fold change

**Supplementary Table S2 A.** Soluble lysosomal enzymes and accessory proteins identified by MS in lysosomal fractions of wt and *Gnpt*-KO MODE-K cells (n=3); related to Figure 3.9 A.

| | UniProt ID | Protein | Description | Mean KO/wt[1] |
|---|---|---|---|---|
| **1** | Q99LJ1 | **Fuca1** | Alpha-L-fucosidase | -3.61 |
| **2** | Q64191 | **Aga** | N(4)-(beta-N-acetylglucosaminyl)-L-asparaginase | -3.39 |
| **3** | P20060 | **Hexb** | Beta-hexosaminidase subunit beta | -2.79 |
| **4** | P50428 | **Arsa** | Arylsulfatase A | -3.56 |
| **5** | O35657 | **Neu1** | Sialidase-1 | -3.58 |
| **6** | Q9WUU7 | **Ctsz** | Cathepsin Z | -3.44 |
| **7** | Q04519 | **Smpd1** | Sphingomyelin phosphodiesterase | -3.23 |
| **8** | Q8JZV7 | **Naga** | Alpha-N-acetylgalactosaminidase | -3.68 |
| **9** | Q8R242 | **Ctbs** | Di-N-acetylchitobiase | -3.18 |
| **10** | P12265 | **Gusb** | Beta-glucuronidase | -3.11 |
| **11** | P28798 | **Grn** | Progranulin | -2.94 |
| **12** | Q08890 | **Ids** | Iduronate 2-sulfatase | -2.95 |
| **13** | O54752 | **Naglu** | Alpha-N-acetylglucosaminidase | -2.79 |
| **14** | Q8VEB4 | **Pla2g15** | Phospholipase A2 group XV | -2.41 |
| **15** | Q8K2I4 | **Manba** | Beta-mannosidase | -2.32 |
| **16** | Q9Z0J0 | **Npc2** | NPC intracellular cholesterol transporter 2 | -2.15 |
| **17** | Q571E4 | **Galns** | N-acetylgalactosamine-6-sulfatase | -2.23 |
| **18** | Q61207 | **Psap** | Prosaposin | -2.08 |
| **19** | P50429 | **Arsb** | Arylsulfatase B | -1.85 |
| **20** | Q8BFR4 | **Gns** | N-acetylglucosamine-6-sulfatase | -1.65 |
| **21** | O89023 | **Tpp1** | Tripeptidyl-peptidase 1 | -1.51 |
| **22** | Q8R2Y0 | **Abhd6** | Monoacylglycerol lipase | -1.42 |
| **23** | Q9WV54 | **Asah1** | Acid ceramidase | -1.24 |
| **24** | P18242 | **Ctsd** | Cathepsin D | -1.08 |

| | | | | |
|---|---|---|---|---|
| 25 | O08709 | **Prdx6** | Peroxiredoxin-6 | +1.44 |
| 26 | O35405 | **Pld3** | 5'-3' exonuclease | +2.69 |
| 27 | Q60648 | **Gm2a** | Ganglioside GM2 activator | +2.66 |

**Supplementary Table S2 C.** Proteins involved in lysosomal mobility identified by MS in lysosomal fractions of wt and *Gnpt*-KO MODE-K cells (n=3); related to Figure 3.9 C.

| | **UniProt ID** | **Protein** | **Description** | **Mean KO/wt[1]** |
|---|---|---|---|---|
| 1 | Q80UG5 | **Sept9** | Septin-9 | -0.98 |
| 2 | Q9JHU4 | **Dyhc1** | Dynein 1 heavy chain 1 | +1.02 |
| 3 | Q61768 | **Kif5b** | Kinesin-1 heavy chain | +0.95 |

**Supplementary Table S2 E.** Lysosomal membrane proteins identified by MS in lysosomal fractions of wt and *Gnpt*-KO MODE-K cells (n=3); related to Figure 3.9 E.

| | **UniProt ID** | **Protein** | **Description** | **Mean KO/wt[1]** |
|---|---|---|---|---|
| 1 | Q9CXT7 | **Tmem192** | Transmembrane protein 192 | -3.57 |
| 2 | P11438 | **Lamp1** | Lysosome-associated membrane glycoprotein 1 | -1.79 |
| 3 | Q9JHJ3 | **Glmp** | Glycosylated lysosomal membrane protein | -1.15 |
| 4 | Q3UDW8 | **Hgsnat** | Heparan-alpha-glucosaminide N-acetyltransferase | -1.15 |
| 5 | Q91W98 | **Slc15a4** | Lysosomal L-histidine exporter | -1.19 |
| 6 | Q80X71 | **Tmem106b** | Transmembrane protein 106B | -0.78 |
| 7 | Q8BGP5 | **Tmem127** | Transmembrane protein 127 | +0.84 |
| 8 | Q9CWK8 | **Snx2** | Sorting nexin-2 | +1.03 |
| 9 | Q9JIS8 | **Slc12a4** | Potassium-chloride cotransport channel | +1.01 |
| 10 | Q6P8X1 | **Snx6** | Sorting nexin-6 | +0.98 |
| 11 | Q66JT1 | **Lrrc8e** | Volume-regulated anion channel subunit E | +1.21 |
| 12 | P41234 | **Abca2** | ATP-binding cassette sub-family A member 2 | +1.86 |
| 13 | Q9JJR8 | **Tmem9b** | Transmembrane protein 9B | +1.41 |
| 14 | Q3UHD6 | **Snx27** | Sorting nexin-27 | +1.69 |
| 15 | Q80WG5 | **Lrrc8a** | Volume-regulated anion channel subunit A | +2.39 |

| | | | | |
|---|---|---|---|---|
| **16** | Q91XQ6 | **Laptm4b** | Lysosomal-associated transmembrane protein 4B | +2.74 |
| **17** | B1AWN4 | **Atp10b** | Catalytic subunit of the ATPase flippase complex | +4.26 |
| **18** | P35951 | **Ldlr** | Low-density lipoprotein receptor | +1.91 |

**Supplementary Table S3. Autophagy related proteins** associated with enriched lysosomal fractions of wt and *Gnpt*-KO MODE-K cells (n=3); related to Figure 4.1. [1] log2 fold change

| | **UniProt ID** | **Protein** | **Description** | **Mean KO/wt[1]** |
|---|---|---|---|---|
| **1** | Q9JL15 | **Lgals8** | Beta-galactoside-binding lectin, sensor of membrane damage | +3.92 |
| **2** | Q9CQV6 | **Map1lc3b** | Ubiquitin-like modifier, involved in formation of autophagosomes | +3.68 |
| **3** | Q64337 | **Sqstm1** | Molecular adapter required for selective macroautophagy | +5.10 |
| **4** | Q3UKC1 | **Tax1bp1** | Ubiquitin-binding adapter that participates in selective autophagy regulation | +5.58 |
| **5** | Q91VM3 | **Wdr45 (Wipi4)** | Component of the autophagy machinery | +3.61 |
| **6** | Q68FE2 | **Atg9a** | Phospholipid scramblase mediating autophagosomal membrane expansion | +4.34 |
| **7** | P97432 | **Nbr1** | Ubiquitin-binding autophagy adapter | +4.21 |
| **8** | Q9CPX6 | **Atg3** | E2 conjugating enzyme | +3.37 |
| **9** | Q8C0J2 | **Atg16l1** | interacts with ATG12-ATG5 to mediate the lipidation to ATG8 family proteins | +2.46 |
| **10** | O70405 | **Ulk1** | Serine/threonine-protein kinase involved in autophagy in response to starvation | +3.13 |
| **11** | Q91YI1 | **Atg13** | Autophagy factor required for autophagosome formation | +2.98 |
| **12** | Q9D8Z6 | **Atg101** | Autophagy factor required for autophagosome formation | +3.34 |
| **13** | Q8K3K8 | **Optn** | Autophagy modifier of the MAP1 LC3 family | +7.04 |
| **14** | Q9QY73 | **Tmem59** | Regulator promoting LC3-ATG16L1 functional complex and LC3 lipidation | +7.03 |
| **15** | O88653 | **Lamtor3** | Involved in amino acid sensing and activation of mTORC1 | +2.14 |
| **16** | P16110 | **Lgals3** | Coordinates the recognition of membrane damage with mobilization of the core autophagy regulators | +1.71 |
| **17** | Q9DC51 | **Gnai3** | GTPase acting as autophagy modulator | +1.68 |
| **18** | P63017 | **Hspa8** | Molecular chaperone involved in chaperone-mediated autophagy | +1.48 |
| **19** | Q80XK6 | **Atg2b** | Lipid transfer protein required for autophagosome formation | +1.06 |

| | | | | |
|---|---|---|---|---|
| **20** | Q9CR48 | **Dram2** | Role in the initiation of autophagy | +1.35 |
| **21** | Q99J83 | **Atg5** | Involved in autophagic vesicle formation | +1.31 |
| **22** | Q80W47 | **Wipi2** | Component of the autophagy machinery | +1.26 |
| **23** | Q8VEJ9 | **Vps4a** | Selective lipophagy receptor | +1.20 |
| **24** | Q80X95 | **Rraga** | Regulation of the mTORC1 signaling cascade | +0.88 |
| **25** | Q8K4Q0 | **Rptor** | Component of mTORC1 | +0.75 |

**Supplementary Table S4.** Lipid species in isolated lysosomal fractions from wt and *Gnpt*-KO MODE-K cells (n=4); related to Figure 3.14.

| | | **Relative intensities ±SD** | | |
|---|---|---|---|---|
| **Lipid species (ions)** [1] | **Chains** | **wild type** | ***Gnpt*-KO** | **Ratio KO/wt** |
| BMP 36:2 (-) | 18:1/18:1 | 0.156±0.04 | 0.091±0.03 | 0.59 |
| BMP 36:2 (+) | 18:1/18:1 | 0.056±0.02 | 0.033±0.01 | 0.59 |
| BMP 34:2 (-) | 16:1_18:1 | 0.029±0.01 | 0.019±0.01 | 0.66 |
| BMP 34:2 (+) | 16:1_18:1 | 0.011±0.00 | 0.007±0.00 | 0.65 |
| Cer 42:2;2O (+) | 18:1;2O/24:1 | 0.0245±0.00 | 0.0773±0.01 | 3.15 |
| Cer 34:1;2O (+) | 18:1;2O/16:0 | 0.0212±0.00 | 0.0608±0.00 | 2.87 |
| Cer 40:1;2O (+) | 18:1;2O/22:0 | 0.0113±0.00 | 0.0480±0.01 | 4.26 |
| Cer 42:2;2O (+) | 18:2;2O/24:0 | 0.0053±0.00 | 0.0113±0,00 | 2.14 |
| Cer 42:3;2O (+) | 18:2;2O/24:1 | 0.0035±0.00 | 0.0115±0,00 | 3.27 |
| Cer 41:1;2O (+) | 18:1;2O/23:0 | 0.0034±0.00 | 0.0089±0,00 | 2.65 |
| Cer 40:0;2O (+) | 18:0;2O/22:0 | 0.0015±0.00 | 0.0047±0,00 | 3.19 |
| Cer 40:2;2O (+) | 18:2;2O/22:0 | 0.0015±0.00 | 0.0055±0,00 | 3.76 |
| Cer 36:1;2O (+) | 18:1;2O/18:0 | 0.0013±0.00 | 0.0061±0,00 | 4.63 |
| Cer 38:1;2O (+) | 18:1;2O/20:0 | 0.0010±0.00 | 0.0050±0,00 | 4.93 |
| Cer 40:2;2O (+) | 18:1;2O/22:1 | 0.0010±0.00 | 0.0044±0,00 | 4.43 |
| Cer 39:1;2O (+) | 18:1;2O/21:0 | 0.0005±0.00 | 0.0023±0,00 | 4.22 |
| Cer 38:0;2O (+) | 18:0;2O/20:0 | 0.0005±0.00 | 0.0015±0,00 | 3.38 |
| Cer 36:2;2O (+) | 18:2;2O/18:0 | 0.0003±0.00 | 0.0015±0,00 | 4.31 |
| DG 36:1 (+) | 18:0_18:1 | 0.0091±0.00 | 0.0187±0.00 | 2.05 |

| | | | | |
|---|---|---|---|---|
| DG 40:5 (+) | not specified | 0.0005±0.00 | 0.0012±0.00 | 2.55 |
| LPC 24:0 (+) | not specified | 0.0016±0.00 | 0.0005±0.00 | 0.31 |
| LPC 24:1 (+) | not specified | 0.0009±0.00 | 0.0003±0.00 | 0.35 |
| PC 42:0 (+) | not specified | 0.0008±0.00 | 0.0003±0.00 | 0.41 |
| PC 36:4 (-) | 16:0_20:4_A | 0.0177±0.01 | 0.0390±0.01 | 2.20 |
| PC 38:5_B (+) | not specified | 0.0148±0.00 | 0.0343±0.00 | 2.33 |
| PC 36:4 (+) | 16:0_20:4_B | 0.0142±0.01 | 0.0391±0.01 | 2.76 |
| PC 38:3_A (+) | not specified | 0.0074±0.00 | 0.0152±0.00 | 2.05 |
| PC 40:5_A (+) | not specified | 0.0054±0.00 | 0.0132±0.00 | 2.45 |
| PC 40:6 (+) | 18:0_22:6 | 0.0050±0.00 | 0.0138±0.00 | 2.74 |
| PC 31:0_B (+) | not specified | 0.0050±0.00 | 0.0109±0.00 | 2.16 |
| PC 38:6_B (+) | not specified | 0.0044±0.00 | 0.0103±0.00 | 2.33 |
| PC 38:5_A (+) | not specified | 0.0031±0.00 | 0.0067±0.00 | 2.16 |
| PC 40:6 (+) | not specified | 0.0030±0.00 | 0.0063±0.00 | 2.07 |
| PC 33:0 (+) | 16:0_17:0 | 0.0026±0.00 | 0.0051±0.00 | 2.00 |
| PC 40:4 (+) | 18:0_22:4 | 0.0024±0.00 | 0.0061±0.00 | 2.53 |
| PC 40:3_A (+) | not specified | 0.0009±0.00 | 0.0019±0.00 | 2.03 |
| PC 42:10 (+) | not specified | 0.0002±0.00 | 0.0004±0.00 | 2.08 |
| PE 40:6 (+) | not specified | 0.0169±0.00 | 0.0350±0.01 | 2.08 |
| PS 38:4 (-) | 18:0_20:4 | 0.0188±0.01 | 0.0414±0.01 | 2.21 |
| SM 42:2;2O (+) | 18:1;2O/24:1 | 0.0630±0.01 | 0.1374±0.01 | 2.18 |
| SM 36:1;2O_A (-) | not specified | 0.0218± 0.00 | 0.0623±0.01 | 2.86 |
| SM 34:0;2O_A (-) | not specified | 0.0200±0.00 | 0.0468±0.00 | 2.34 |
| SM 40:1;2O (+) | 18:1;2O/22:0 | 0.0183±0.00 | 0.0680±0.01 | 3.71 |
| SM 34:0;2O_B (+) | not specified | 0.0157±0.00 | 0.0447±0.00 | 2.85 |
| SM 36:1;2O_B (+) | not specified | 0.0124±0.00 | 0.0438±0.01 | 3.54 |
| SM 41:1;2O (+) | not specified | 0.0052±0.00 | 0.0111±0.00 | 2.13 |
| SM 40:2;2O_A (+) | not specified | 0.0050±0.00 | 0.0139±0.00 | 2.77 |
| SM 36:2;2O (+) | not specified | 0.0045±0.00 | 0.0102±0.00 | 2.25 |
| SM 35:1;2O (+) | not specified | 0.0033±0.00 | 0.0079±0.00 | 2.37 |

| | | | | |
|---|---|---|---|---|
| SM 38:1;2O (+) | not specified | 0.0033±0.00 | 0.0127±0.00 | 3.88 |
| SM 40:2;2O_B (+) | not specified | 0.0030±0.00 | 0.0106±0.00 | 3.49 |
| SM 41:2;2O | not specified | 0.0025±0.00 | 0.0067±0.00 | 2.69 |
| SM 44:2;2O (+) | not specified | 0.0014±0.00 | 0.0028±0.00 | 2.02 |
| SM 40:0;2O (+) | not specified | 0.0013±0.00 | 0.0042±0.00 | 3.18 |
| SM 43:2;2O (+) | not specified | 0.0010±0.00 | 0.0023±0.00 | 2.22 |
| SM 44:3;2O (+) | not specified | 0.0005±0.00 | 0.0010±0.00 | 2.06 |
| SM 32:0;2O (+) | not specified | 0.0004±0.00 | 0.0008±0.00 | 2.16 |

[1] Alphabetical ordered lipid groups

BMP, Bis(monoaclylglycero)phosphates; Cer, ceramides; DG, diacylglyceroles; Hex2Cer, Dihexosylceramide; LPC, Lysophosphatidylcholines; PC, Phosphatidylcholines; PE, Phosphatidylethanolamine; PS, Phosphatidylserine; SM, Sphingomyelins. Notation “A” and “B” represent potential isomers (sn-positions of fatty acyls not determined as well as Cis/Trans isomerism). (+): detected in positive ESI mode; (-): detected in negative ESI mode.

**Supplementary Table S5.** Antibodies.

| Antibody | Host | Cat. | Vendor | Dilution* |
|---|---|---|---|---|
| **Arl8a** | rabbit | 17060-1-AP | ProteinTech | 1:500 (WB) |
| **BMP (LBPA)** | mouse | gift by Dr. J Gruenberg** | Hybridoma supernatant | 1:50 (IF) |
| **Borcs5 (Myrlysin)** | rabbit | 17169-1-AP | ProteinTech | 1:500 (WB) |
| **Borcs7 (Diaskedin)** | rabbit | ABN-PAB23142 | Biozol Abnova | 1:350 (WB) |
| **CtsB** | goat | GT15047 | Neuromics | 1:1,000 (WB) |
| **CtsC** | mouse | sc-74590 | Santa Cruz | 1:1,000 (WB) |
| **CtsD** | rabbit | #69854 (E179) | Cell Signaling | 1:1,000 (WB) |
| **CtsZ** | goat | AF1033 | R&D | 1:1,000 (WB) |
| **Gapdh** | rabbit | sc-25778 | Santa Cruz | 1:1,000 (WB) |
| **GFP** | rabbit IgG | A11122 | Invitrogen | 1:2,000 (WB)<br>1:500 (IF) |
| **GM130** | mouse | 610822 | BD Biosciences | 1:1,000 (WB) |
| **Lamp1** | rat | 1D4B | Hybridoma | 1:1,000 (WB and IF) |
| **Lamp1 (C-tail)** | rabbit | Ab24170 | Abcam | 1:150 (IF) |
| **LC3B** | rabbit | NB100-2220 | Novusbio | 1:1,500 (WB) |

# Supplementary Tables

| | | | | |
|---|---|---|---|---|
| **LC3B** | rabbit | 12741 | Cell Signaling | 1:100 (IF) |
| **Prgn** | sheep | AF2557 | R&D | 1:1,000 (WB) |
| **Rab7** | rabbit | #9367 | Cell Signaling | 1:1,000 (WB) |
| **Tubulinα** | mouse | T9026 | Sigma | 1:5,000 (WB) |
| **v-ATPase B2 (Atp6v1b2)** | mouse | sc-166045 | Santa Cruz | 1:500 (WB) |
| **ZO-1** | mouse | 33-9100 | Invitrogen | 1:100 (IF) |
| **Alexa Fluor (AF) anti-rabbit 488** | goat | A11035 | Invitrogen | 1:1,000 (IF) |
| **AF anti-rat488** | donkey | A21208 | Invitrogen | 1:1,000 (IF) |
| **AF anti-mouse 546** | goat | A11030 | Invitrogen | 1:1,000 (IF) |
| **AF anti-rat igG (H+L) Plus 594** | donkey | A48271 | Invitrogen | 1:1,000 (IF) |
| **Peroxidase AffiniPure anti-rabbit IgG (H+L)** | goat | 111-035-003 | Jackson | 1:1,000 (WB) |
| **Peroxidase AffiniPure anti-mouse IgG** | goat | 115-035-003 | Jackson | 1:1,000 (WB) |
| **Peroxidase-conjugated AffiniPure anti-rat IgG** | goat | 112-035-003 | Jackson | 1:1,000 (WB) |
| **anti-goat HRP** | rabbit | 305-035-003 | Dianova | 1:1,000 (WB) |

*WB, western blot; IF, immunofluorescence

**(Kobayashi et al., 1998)

Dyes were used at the following dilutions: LysoTracker Deep Red **1:20,000**, Bodipy Lactosylceramide complexed to BSA **1:100**, WGA CF488A **1:200**, WGA AF 555 conjugate **1:200**, Phalloidin660 **1:100**, HCS LipidTOX™ Red Neutral lipid stain **1:1,000**, Cyto-ID **1:500** (2 µl/ml); Filipin complex ready made **1:200** (25 µg/ml).

# 9. Abbreviations

| | |
|---|---|
| **β-Hex** | β-hexosaminidase |
| **Δ2** | Delta 2-tubulin |
| **µg** | microgram |
| **µl** | microliter |
| **µm** | micrometer |
| **µM** | micromolar |
| **xg** | times gravity |
| **3D** | three-dimensional |
| **4D** | four-dimensional |
| **AF** | Alexa Fluor |
| **ALR** | Autophagic lysosome reformation |
| **Arl** | ARF-Like protein |
| **Asn** | Asparagine |
| **Asp** | Aspartic acid |
| **ATF** | Activating Transcription Factor |
| **ATG** | Autophagy-related gene |
| **ATP** | Adenosine triphosphate |
| **Au** | Gold |
| **BCA** | Bicinchoninic acid |
| **BCV** | Bacteria-containing vacuole |
| **BMP** | Bis(monoacylglycero)phosphate |
| **Borcs** | BLOC-one-related complex subunit |
| **bp** | base pair |
| **BSA** | Bovine Serum Albumin |
| **C-terminal** | Carboxy-terminal |
| **$Ca^{2+}$** | Calcium$^{2+}$ |
| **CCV** | Clathrin-coated vesicle |
| **CD-MPR** | Cation-dependent mannose 6-phosphate receptor 46 kDa |
| **cDNA** | complementary DNA |
| **CER** | Ceramide |
| **CI-MPR** | Cation-independent mannose 6-phosphate receptor 300 kDa |
| **cl** | clone |
| **COPI** | Coat protein complex I |
| **COPII** | Coat protein complex II |
| **CQ** | Chloroquine |
| **CR1-4** | Conserved Region 1-4 |
| **CRISPR** | Clustered regularly interspaced short palindromic repeats |
| **DAPI** | 2-(4-amidinophenyl)-1H-indole-6-carboxamidine |
| **DG** | Diacylglycerol |
| **DIA** | Data-independent acquisition |
| **DMAP** | DNA methyltransferase-associated protein |
| **DMEM** | Dulbecco's Modified Eagle's Medium |
| **DMSO** | Dimethylsulfoxid |
| **DNA** | Deoxyribonucleic acid |
| **DPBS** | Dulbecco´s Phosphate Buffered Saline |

# Abbreviations

| | |
|---|---|
| **DTT** | Dithiothreitol |
| **ECL** | Enhanced chemiluminescence |
| **ECM** | Extracellular matrix |
| **EDTA** | Ethylenediamine tetraacetic acid disodium salt dehydrate |
| **e.g.** | exempli gratia, for example |
| **EGF** | Epidermal growth factor |
| **EM** | Electron microscopy |
| **ER** | Endoplasmic reticulum |
| **ERGIC** | ER-Golgi intermediate compartment |
| **ESCRT** | Endosomal Sorting Complex Required for Transport |
| **et al.** | and others |
| **FBS** | Fetal Bovine Serum |
| **Fig** | Figure |
| **fps** | frame per second |
| **GA** | glutaraldehyde |
| **Glc** | D-glucose |
| **GlcNAc** | N-Acetyl-D-glucosamine |
| **GNPT** | N-Acetylglucosamine-1-phosphotransferase |
| **Gnpt$^{ki}$** | N-Acetylglucosamine-1-phosphotransferase knock-in |
| **GO** | Gene ontology |
| **GTP** | Guanosine triphosphate |
| **HA** | Human influenza hemagglutinin |
| **HBSS** | Hank´s Balanced Salt Solution |
| **HeLa** | human cell line from cervical cancer (Henrietta Lacks) |
| **HRP** | Horseradish peroxidase |
| **hrs** | hours |
| **IF** | immunofluorescence |
| **ins** | insertion |
| **kDa** | kiloDalton |
| **ki** | knock-in |
| **KO** | knock-out |
| **LacCer** | Lactosylceramide |
| **LCV** | *Legionella*-containing vacuole |
| **LL** | Dileucine (leucine-leucine) |
| **LLS** | Lattice lightsheet |
| **LPC** | Lysophosphatidylcholin |
| **LPS** | Lipopolysaccharide |
| **LSD** | Lysosomal storage disease |
| **Lys** | Lysine |
| **LYSET** | Lysosomal Enzyme Trafficking factor |
| **M6P** | Mannose 6-phosphate |
| **Man** | D-mannose |
| **MEF** | Mouse embryonic fibroblasts |
| **min** | minute |
| **MiTF** | Microphthalmia-associated transcription factor |
| **mg** | milligram |
| **ml** | milliliter |

# Abbreviations

| | |
|---|---|
| **mm** | millimiter |
| **mM** | millimolar |
| **MOI** | Multiplicity of infection |
| **ML II** | Mucolipidosis type II |
| **MPR** | M6P receptor |
| **MS** | Mass spectrometry |
| **mTORC1** | mammalian Target Of Rapamycin Complex 1 |
| **MSD** | Mean squared displacement |
| **N-terminal** | Amino-terminal |
| **N1-2** | Notch repeats 1-2 |
| **NA** | Numerical aperture |
| **nm** | nanometer |
| **nM** | nanomolar |
| **OD** | Optical density |
| **P** | Phosphate |
| **P/S** | Penicillin/streptomycin |
| **PBS** | Phosphate Buffered Saline |
| **PC** | Phosphatidylcholine |
| **PCA** | Principal component analysis |
| **PCR** | Polymerase chain reaction |
| **PCV** | Pathogen-containing vesicle |
| **PE** | Phosphatidylethanolamine |
| **PFA** | Paraformaldehyde |
| **PI$_3$P** | Phophaditylinositol-3-phosphate |
| **polyE** | polyglutamylation |
| **Pro** | Proline |
| **PTM** | posttranslational modification |
| **Rab** | Ras-related protein |
| **RFP** | Red fluorescent protein |
| **RIR** | Arginine-Isoleucine-Arginine |
| **ROI** | Region of interest |
| **rpm** | revolutions per minute |
| **RP-UHPLC-TIMS MS** | Reverse-phase Ultra-high performance liquid chromatography-Trapped Ion Mobility Spectrometry |
| **RUFY** | RUN- and FYVE-domain-containing |
| **S1-4** | Spacer regions 1-4 |
| **S1P** | Site-1 protease |
| **SCV** | *Salmonella*-containing vacuole |
| **SD** | Standard deviation |
| **SDS** | Sodium Dodecyl Sulfate |
| **sec** | second |
| **SEP** | Superecleptic pHluorin |
| **Ser** | Serine |
| **sgRNA** | single-guide ribonucleic acid |
| **SM** | Sphingomyelin |
| **SNARE** | Soluble N-ethylmaleimide-sensitive factor attachment protein receptor |
| **SPIONs** | Superparamagnetic iron oxide nanoparticles |

# Abbreviations

| | |
|---|---|
| **TBST** | Tris-buffered saline/Tween20 |
| **TEM** | Transmission electron microscopy |
| **TFE3** | Transcription Factor E3 |
| **TFEB** | Transcription Factor EB |
| **TFEC** | Transcription Factor EC |
| **TGN** | *Trans*-Golgi network |
| **Thr** | Threonine |
| **TMEM** | Transmembrane protein |
| **Tris** | Tris-hydroxymethyl-aminomethane |
| **TRPML1** | Transient Receptor Potential channel Mucolipin 1 |
| **Ub** | Ubiquitin |
| **UCE** | Uncovering enzyme |
| **UDP** | Uridine diphosphate |
| **UVRAG** | Ultraviolet radiation resistance-associated protein |
| **v/v** | volume/volume |
| **VAMP** | Vesicle associated membrane protein |
| **Vps** | Vacuolar protein sorting-associated protein |
| **VRAC** | Volume-regulated anion channel |
| **WB** | Western blotting |
| **WGA** | Wheat germ agglutinin |
| **WIPI** | WD-repeat protein Interacting with PhosphoInositides |
| **wt** | wild-type |
| **YCV** | *Yersinia*-containin vacuole |
| **ZO-1** | Zonula Occludens-1 |

## 10. Acknowledgements

This doctoral work is based on the results of my studies carried out in the laboratory of Prof. Dr. Thomas Braulke at the Center for Experimental Medicine, Institute of Osteology and Biomechanics (Universitätsklinikum Hamburg-Eppendorf, UKE, Germany) between October 2020 and September 2024. Throughout these years I perceive I have grown significantly as a person and as a scientist, learning to focus on my goals, to work willingly hard independently on any timetable, tiredness and to cope with stressful situations. I consider these as very valuable lessons for life. I leave surely with more knowledge, but also grateful for the self-awareness gained. For these reasons, alongside for his supervision, guidance and time, my heartfelt thanks go to Thomas. I am sure this journey into cellular biology and your mentorship improved my research skills and prepared me for future challenges.

I would like to express my sincere gratitude to my thesis supervisors, Prof. Dr. Klaus Ruckdeschel (UKE) for evaluating this dissertation and to Prof. Dr. Tim W. Gilberger (Universität Hamburg) for joining the Thesis Committee. To Prof. Dr. Klaus Ruckdeschel and his collaborators (Dr. med. Benjamin Berinson, Nick Mohr MTA) my gratitude for their precious collaboration in regard to the *Yersinia enterocolitica* infection experiments performed.

I am very thankful to all our collaborators, including Prof. Dr. Jens Bosse (Hannover Medical School) and Saskia Sanders (M.Sc.) for their fundamental microscopy support and work on the single-particle analysis; to Prof. Dr. Sabrina Jabs (University of Kiel) my heartfelt thanks for teaching me how to prepare intestinal organoids, for assisting me during my first steps with these amazing cells and for her scientific support during this experience; to Dr. Michaela Schweizer (UKE), for her always kind and welcoming approach and for providing us great EM images; to Prof. Dr. Dominic Winter (University of Bonn) and his group (Dr. Robert Hardt, Anne Sanner M.Sc.) for their work concerning the proteomic analyses on my samples; to Prof. Dr. Diego Luís Medina (University of Naples “Federico II”) and to Prof. Dr. Eduardo Sommella (University of Salerno) for the lipidomic analysis successfully performed; to Prof. Dr. Tobias Stauber and Dr. Shroddha Bose (Medical School Hamburg) for their work on lysosomal pH measurements; to Prof. Dr. Marina Mikhaylova (Humboldt University, Berlin) for her work on the analysis of microtubule posttranslational modifications; to Prof. Dr. Denise Monack (Stanford University School of Medicine, CA) for giving me the opportunity to join her laboratory for my internship and to her brilliant collaborator Dr. Joy A. McKenna for her kindness, for making me feel at ease and for showing me how to reverse organoid polarity.

# Acknowledgements

Sincere thanks to the Research Training Group 2771 “Humans and Microbes: Reorganisation of Cell Compartments and Molecular Complexes during Infection” and to Prof. Dr. Martin Aepfelbacher for funding my research, for giving me the opportunity to fly to California and live this amazing internship research experience.

A huge thanks to my beloved family, who I have been missing a lot over these years and who, despite the distance especially during those difficult pandemic times, never missed lending to me their love and support. I feel blessed.

Last but not least, an enormous thanks to my soon wife-to-be Giulia. Your delicate, lovely and unique presence filled my life and enlightened my worst days. Words cannot adequately express my gratitude. You just mean everything to me.

# 11. Eidesstattliche Versicherung

Ich versichere ausdrücklich, dass ich die Arbeit selbständig und ohne fremde Hilfe, insbesondere ohne entgeltliche Hilfe von Vermittlungs- und Beratungsdiensten, verfasst, andere als die von mir angegebenen Quellen und Hilfsmittel nicht benutzt und die aus den benutzten Werken wörtlich oder inhaltlich entnommenen Stellen einzeln nach Ausgabe (Auflage und Jahr des Erscheinens), Band und Seite des benutzten Werkes kenntlich gemacht habe. Das gilt insbesondere auch für alle Informationen aus Internetquellen.

Soweit beim Verfassen der Dissertation KI-basierte Tools („Chatbots“) verwendet wurden, versichere ich ausdrücklich, den daraus generierten Anteil deutlich kenntlich gemacht zu haben. Die „Stellungnahme des Präsidiums der Deutschen Forschungsgemeinschaft (DFG) zum Einfluss generativer Modelle für die Text- und Bilderstellung auf die Wissenschaften und das Förderhandeln der DFG“ aus September 2023 wurde dabei beachtet. Ferner versichere ich, dass ich die Dissertation bisher nicht einem Fachvertreter an einer anderen Hochschule zur Überprüfung vorgelegt oder mich anderweitig um Zulassung zur Promotion beworben habe. Ich erkläre mich damit einverstanden, dass meine Dissertation vom Dekanat der Medizinischen Fakultät mit einer gängigen Software zur Erkennung von Plagiaten überprüft werden kann.

Datum Unterschrift